Interfacial Conformation of Polymer Chains and Its Impact on Film Properties

Bianca Martins de Lima

A Thesis
In the Department
of
Chemical and Materials Engineering

Presented in Partial Fulfillment of the Requirements
For the Degree of
Doctor of Philosophy (Chemical and Materials Engineering) at
Concordia University
Montreal, Quebec, Canada

March 2025

CONCORDIA UNIVERSITY
SCHOOL OF GRADUATE STUDIES

This is to certify that the thesis prepared

By: Bianca Martins de Lima

Entitled: Interfacial Conformation of Polymer Chains and Its Impact on Film Properties

and submitted in partial fulfillment of the requirements for the degree of
DOCTOR OF PHILOSOPHY (Chemical and Materials Engineering)

complies with the regulations of the University and meets the accepted standards with respect to originality and quality.

Signed by the final examining committee:

____ Chair
Dr. Alex De Visscher

____ External Examiner
Dr. Dennis Hore

____ Examiner
Dr. Sana Anbuhi

____ Examiner
Dr. Martin Pugh

____ Examiner
Dr. Jerin John

____ Thesis Supervisor
Dr. Paula Wood-Adams

____ Thesis Supervisor
Dr. Patrick Hayes

Approved by ____
Dr. Zhinin Ye, Graduate Program Director

March/27/2025 ____
Dr. Mourad Debbabi, Dean of the Gina Cody School of Engineering and Computer Science

ABSTRACT

Interfacial Conformation of Polymer Chains and Its Impact on Film Properties

Bianca Martins de Lima, Ph.D.
Concordia University, 2025

Polymeric thin films, exhibiting unique optical, electrical, and mechanical properties, can be engineered for various technologies, including adhesives, membranes, optical systems, and electronics. The interfacial region between these films and their environment plays a crucial role in key processes such as nucleation, crystallization, adhesion, and wettability. The conformation of polymer chains near the interface significantly influences these processes. However, there is lack of studies that establish clear correlations between interfacial chain conformation and the macroscopic behavior of thin films. In this study, we employed sum frequency generation (SFG) spectroscopy to investigate the interfacial conformation of polystyrene chains across various systems, establishing valuable relationships between substrate properties, interfacial chain conformation, and macroscopic thin film properties.

First, we examined the role of the polymer molecular weight in driving interfacial chain conformation. We found significant differences in the conformation of polystyrene chains near a metallic substrate, depending on the polymer molecular weight. Our analysis revealed that the balance between entropy and enthalpy during polymer adsorption plays a crucial role in determining the chain conformation.

Building on the previous findings, we explored the relationship between the polymer molecular weight, the interfacial environment (free and buried interfaces), the chain conformation and the dewetting behavior of thin films. Our study revealed that polystyrene chains of the same molecular weight adopt distinct conformations depending on the interface and that these differences in chain conformation play a key role in determining the dewetting behavior of thin films.

Lastly, we conducted a pioneering work demonstrating the potential use of SFG spectroscopy to determine the lamellar orientation at the surface of semi-crystalline thin films. This

study broadens the scope of SFG spectroscopy and expands the range of analytical tools available for interfacial lamellar orientation analysis, particularly in complex systems, such as at buried interfaces.

This work provides valuable insights that enhance the fundamental understanding of interfacial properties, chain conformations, and the macroscopic behavior of thin films. By integrating innovative SFG spectroscopy applications with theoretical calculations, we have established a robust foundation for future studies in polymer science and materials engineering, driving advancements in thin film technologies and applications.

Acknowledgements

I gratefully acknowledge the research funding support by the Natural Science and Engineering Research Council of Canada Discovery Grant Program (RGPIN-2020-05173 and RGPIN/218056-2012), the Canada Foundation for Innovation (Project 32277), the Fonds de Recherche du Québec - Nature et Technologies (FRQNT) (grant number 2022-PR-300978), as well as Concordia University and the Université de Montréal.

I would like to express my deepest gratitude to my supervisors, Dr. Paula Wood-Adams and Dr. Patrick Hayes, for their guidance, support, and mentorship throughout my PhD journey. Their expertise and encouragement have been key to the successful of this research and to my development as a scientist.

I am also sincerely grateful to the members of my proposal exam and thesis committees—Dr. Martin Pugh, Dr. Sana Anbuhi, Dr. Jerin John, and Dr. Zhibin Ye—for their invaluable feedback and suggestions, which significantly enriched my work.

My heartfelt thanks go to my lab colleagues, Nimo, Milad, Kero, Nonso, Elhan, and Mina, for the partnership we have built over the years. A special thanks to my lab colleague and close friend Mohammadali, for his constant support, thoughtful discussions, and for always being there when I needed help.

Finally, I extend my appreciation to the lab technicians—Heng Wang, Christophe Clément, Harriet Laryea, Kerri Warbanski and Chris Law—for their assistance with experiments and invaluable support with laboratory inquiries. I would also like to thank Stan Guthrie at Altos Photonics for providing an amazing technical support during this project execution.

Thank you.

Dedication

This thesis is dedicated to my husband Fernando and to my daughter Isabella. You are my life's greatest blessing. Your love gives me purpose every day.

To my parents Maria and Amador, and to my sister Karen. Thank you for everything you have done for me.

Contribution of Authors

This thesis includes chapters that are presented in the form of journal articles.

Chapter 3. "Influence of polymer molecular weight on chain conformation at the polystyrene/silver interface". Bianca Martins de Lima, Patrick Hayes, and Paula Wood-Adams, (2021). *Langmuir*, 37(33), 10036–10045.
Bianca Martins de Lima conducted the experimental design, performed the experiments, data analysis, and manuscript preparation. Dr. Paula Wood-Adams and Dr. Patrick Hayes provided invaluable guidance, mentorship, and feedback throughout all stages of the project, including thorough review and constructive input on the manuscript.
All authors reviewed the final manuscript and approved of the contents.

Chapter 4. "The role of interfacial polymer conformation on the dewetting behavior of thin films". Bianca Martins de Lima, Patrick Hayes, and Paula Wood-Adams, to be submitted for publication.
Bianca Martins de Lima conducted the experimental design, performed the experiments, data analysis, and manuscript preparation. Dr. Paula Wood-Adams and Dr. Patrick Hayes provided invaluable guidance, mentorship, and feedback throughout all stages of the project, including thorough review and constructive input on the manuscript.
All authors reviewed the final manuscript and approved of the contents.

Chapter 5. "Lamellar orientation at the surface of isotactic polystyrene thin films analyzed by sum frequency generation spectroscopy". Bianca Martins de Lima, Patrick Hayes, and Paula Wood-Adams, *Analytica Chimica Acta*, 1248, 340904.
Bianca Martins de Lima conducted the experimental design, performed the experiments, data analysis, and manuscript preparation. Kerri Warbanski performed the Atomic Force Microscopy (AFM) experiments. Dr. Paula Wood-Adams and Dr. Patrick Hayes provided invaluable guidance, mentorship, and feedback throughout all stages of the project, including thorough review and constructive input on the manuscript.
All authors reviewed the final manuscript and approved of the contents.

Table of Contents

Chapter 1 . Introduction 1
1.1. Thesis structure and objectives 2
Chapter 2 . Literature Review 4
2.1. Structure and properties of polystyrene 4
2.2. Polymer molecular weight 5
2.2.1. Effect of polymer molecular weight on bulk and interfacial polymer properties 6
2.2.2. Effect of polymer molecular weight on interfacial processes 8
2.3. Polymer thin films 10
2.3.1. The influence of thin film thickness on its properties 10
2.3.2. Polymer thin films fabrication methods 12
2.3.3. Free standing polymer thin films 14
2.4. Crystallization in polymer thin films 15
2.4.1. Comparison of homogeneous and heterogeneous nucleation 15
2.4.2. Influence of substrate properties on polymer nucleation 17
2.4.3. Crystallization in confined systems 18
2.5. Interfacial chain conformation 20
2.5.1. The effect of annealing on the interfacial chain conformation 21
2.5.2. Surface vs buried chain conformation 21
2.5.3. System parameters influencing the interfacial chain conformation 23
2.6. Sum frequency generation (SFG) spectroscopy 25
2.6.1. Comparing SFG spectroscopy with other interfacial analytical methods 25
2.6.2. Key features of SFG spectroscopy 26
2.6.3. Directly probing buried interfaces using SFG spectroscopy 28
Chapter 3 . Influence of polymer molecular weight on chain conformation at the polystyrene/silver Interface 30
3.1. Preface 30
3.2. Abstract 31
3.3. Introduction 31
3.4. Experimental section 34
3.4.1. Materials 34
3.4.2. Sample preparation 34

3.4.3. SFG measurements 36

3.5. Theoretical background 36

3.5.1. Sum frequency generation spectroscopy 36

3.5.2. SFG on metallic substrates 38

3.5.3. Tilt angle calculation 39

3.6. Results and discussion 41

3.6.1. Tilt angle analysis 41

3.6.2. Possible physical-chemical factors affecting PS conformation 47

3.7. Conclusions 50

Chapter 4 . The role of interfacial polymer conformation on the dewetting behavior of thin films 51

4.1. Preface 51

4.2. Abstract 52

4.3. Introduction 52

4.4. Methodology section 55

4.4.1. Theoretical calculations of the free energy of adsorption 55

4.4.1.1. Case study: polystyrene films 56

4.4.1.2. Theory of the free energy of adsorption of polymers 57

4.4.2. Probing the interfacial conformation of PS chains 59

4.5. Results and discussion 60

4.5.1. Theoretical analysis of the free energy of adsorption 60

4.5.1.1. Templated interfacial chain conformation after thermal annealing 60

4.5.1.2. Chain conformation at the air-templated interface 60

4.5.1.3. Chain conformation at the mica-templated interface 61

4.5.2. Effect of the initial chain conformation on the dewetting behavior 64

4.5.2.1. Coiled chains (air-templated interface) transferred to the hydrophobic substrate . 64

4.5.2.2. Extended chains (mica-templated interface) transferred to the hydrophobic substrate. 66

4.5.3. Overview of the relationship between initial chain conformation and the dewetting behavior of thin films. 67

4.5.4. Probing PS interfacial chain conformation with SFG spectroscopy 68

4.5.4.1. Phenyl ring orientation 68

4.5.4.2. End group segregation 70

4.5.4.3. Backbone conformation 71
4.6. Conclusion 74
Chapter 5 . Lamellar orientation at the surface of isotactic polystyrene thin films analyzed by sum frequency generation spectroscopy 76
5.1. Preface 76
5.2. Abstract 77
5.3. Introduction 77
5.4. Experimental section 79
5.4.1. Sample preparation 79
5.4.2. SFG measurements 81
5.4.3. SFG orientation analysis 82
5.5. Results and discussion 84
5.5.1. Crystal growth 84
5.5.2. Confirming the source of the SFG signal 85
5.5.3. Tracking the crystallization progress by SFG 87
5.5.4. Crystalline structure of iPS and expected SFG response 91
5.5.5. Analyzing iPS lamellar orientation with SFG 93
5.5.6. Validating the iPS lamellar orientation 96
5.6. Conclusions 98
Chapter 6 . Conclusions 100
6.1. Detailed conclusions, contributions and future work by chapter 100
Appendix A..105
Appendix B..109
Appendix C..112

List of Figures

Figure 2.1. Structure of polystyrene. A. Atactic polystyrene; B. Syndiotactic polystyrene; and C. Isotactic polystyrene...4

Figure 2.2. Chain conformations of polymers in the bulk and surface regions. A. High molecular weight polymer adopting a random coil conformation in the bulk, with the dashed circle representing the radius of gyration. B. High molecular weight polymer rearranged into a restricted conformation to fit within the narrow interfacial region. C. Low molecular weight polymer adopting a random coil conformation in the bulk. D. Low molecular weight polymer conforming more easily to the surface region. Adapted from [38]..8

Figure 2.3. Model of 3-layer Tg variations in thin films when there are strong interactions between the polymer and the substrate. Adapted from[59] 11

Figure 2.4. Scheme of polymer thin film fabrication methods. A. Dip coating; B. Spray coating and C. Spin coating. Adapted from[69,77]. 13

Figure 2.5. Size of heterogeneous nucleus as a function of the contact angle θc. Adapted from[87]. 16

Figure 2.6. Change in the Gibbs free energy for homogeneous and heterogeneous nucleation. ...17

Figure 2.7. Lamellar orientation of polymer crystals in thin films. A. Scheme showing the chain arrangement within the crystalline lamella; and B. Scheme showing the lamellar packing, which results in different surface topographies. 18

Figure 2.8. Scheme showing different polymer chain conformations throughout the thickness of a thin film. 20

Figure 2.9. Scheme showing the formation of irreversibly adsorbed and loosely adsorbed polymer layers near the substrate. Adapted from [19,107]. 23

Figure 2.10. Schematic representation of polymer chains within a thin film. In the bulk, the polymer chains adopt a random coil conformation with chain entanglements, creating a centrosymmetric

environment that is not SFG-active. At the interfaces, illustrated by the dotted circles, the centrosymmetry is disrupted, allowing these regions to generate an SFG signal. 26

Figure 2.11. SFG spectra showing the vibrational resonances of interfacial molecules. A. Highly ordered interface; and B. Disordered interface. Adapted from[14]...27

Figure 3.1. Experimental steps to produce the silica/PS/Ag sandwiched samples 35

Figure 3.2. Scheme of surface fixed axis (x,y,z), molecular coordinate system (a,b,c), and Euler angles θ, ψ, ϕ where the interface is in the x-y plane. Note that the b axis was omitted from the drawing because it is perpendicular to the page...37

Figure 3.3. C-H stretching vibrational modes for a phenyl ring. 40

Figure 3.4. SFG spectra for PS samples with a Mw of 20 x 10^3 g/mol (black), 100 x 10^3 g/mol (blue) and 400 x 10^3 g/mol (red). Curves are offset for clarity. A. ssp polarization and B. ppp polarization...42

Figure 3.5. SFG spectra in the phenyl ring C-H stretch region for PS samples with a Mw of 20 x 10^3 g/mol (black), 100 x 10^3 g/mol (blue) and 400 x 10^3 g/mol (red). Curves are offset for clarity. Open circles are the average SFG signal and the continuous lines are the fits obtained using Equation 3.4. A. ssp polarization, B. ppp polarization...42

Figure 3.6. Amplitudes of C-H stretch phenyl ring vibrational modes. A. $\nu 20b$, ssp; B. $\nu 2$, ssp; C. $\nu 7a$, ppp and D. $\nu 2$, ppp. Error bars represent the uncertainties from Table 3.2. 44

Figure 3.7. Ratio of ssp over ppp amplitudes for the $\nu 2$ vibrational mode. The uncertainties were determined as described in section A1 of Appendix A for the ratio of amplitudes. 45

Figure 3.8. Tilt angle analysis of the PS pendant phenyl ring using Equation 3.5. Curves show the ssp over ppp ratios for different tilt angles (θ) considering different values of σ (1°, 10°, 20°, and 30°). The grey region represents the experimental $\nu 2$ ssp over ppp ratio and its uncertainty (Figure 3.7). The overlap of the grey region with the back lines represents possible values for θ and σ. A. Mw 20 x10^3 g/mol. B. Mw 100 x10^3 g/mol and C. Mw 400 x10^3 g/mol. 45

Figure 3.9.A. δc as a function of Mw and B. Scheme of interfacial structure for low and high Mw PS. Low Mw: An entropically driven isotropic backbone conformation exists at the interface and the enthalpy is maximized by d-π* interactions and a high tilt angle enabled by torsions in the backbone; High Mw: An enthalpically driven tail-loop-train backbone conformation exists with phenyl rings tilted to maximize backbone/substrate interactions, while the enthalpy is also increased by π-π interactions between phenyl groups and edge-on interactions with the substrate. 49

Figure 4.1. A. Schematic illustration of the sample preparation method for dewetting studies, according to Sabzevari et al.[50]; and B. Trend in dewetting velocity (originally reported in terms of slip length) of the films as a function of the molecular weight. Each curve is named based on the interface that was placed in direct contact with the hydrophobic substrate. Here, T.I. indicates templated interface. 56

Figure 4.2. Adsorption parameters for PS adsorption on mica. 63

Figure 4.3. A. Adsorption parameters for PS adsorption on a hydrophobic substrate (initial coiled conformation); and B. Free energy of adsorption for PS on a hydrophobic substrate (initial extended conformation), where the percentages indicate the amount of polymer-substrate interactions that were effectively transferred from the mica to the hydrophobic substrate. 66

Figure 4.4. Scheme of the relationship between the chain's initial conformation, the adsorption entropy and enthalpy, and the experimental dewetting rate. 68

Figure 4.5. $ACH3/ACH2$ for the symmetric and asymmetric stretches as a function of the molar fraction of $nCH3\ /nCH2$. Here, ss and as are the symmetric and asymmetric stretches, respectively. 71

Figure 4.6. A. Scheme of IR transition dipole moment change for $CH2$ symmetric and antisymmetric stretches and B. Methylene group oriented with its C_2 axis near the surface normal. The SFG amplitude of each vibrational mode in ssp polarization is proportional to the z component of the IR transition dipole moment change for each mode. 72

Figure 4.7. SFG amplitudes of the PS backbone methylene groups (ssp polarization). 72

Figure 5.1. Scheme of methodology used in the study 80

Figure 5.2. A. C-H stretch vibrational modes of iPS phenyl ring. B. Phenyl ring Euler angles, tilt angle of iPS phenyl ring (θ), twist (ψ) and the azimuthal (φ) angles. C. C-H stretch vibrational modes of $CH2$. d. Tilt angle of iPS backbone $CH2$ groups (θb)..83

Figure 5.3. Optical microscopy images of the iPS films that are: A. amorphous and crystallized at 180 °C for B. 2.5 h, C. 5 h, D.10 h and E.16 h..85

Figure 5.4. A. SFG spectra of the amorphous and 16 h semi-crystalline iPS films collected in spp polarization. B. SFG spectra of the 16 h iPS film with and without the top surface coated with a thin layer of PMMA (ssp polarization). C. PMMA SFG spectrum in ssp polarization, showing the absence of features from 3000 cm^{-1} to 3100 cm^{-1}. 87

Figure 5.5. A. SFG spectra of iPS amorphous films and 2.5 h semi-crystalline films. B. SFG spectra of iPS amorphous films and 16 h semi-crystalline films. All spectra are in ssp polarization. 89

Figure 5.6. A. SFG spectra of a 5 h film, the curves are multiple spectra taken from different spots (curve numbers) of one specimen, in a single day. B. SFG spectra of iPS amorphous films and crystallized at 180 °C for 2.5 h, 5 h, 10 h and 16 h. C. Ratio of the SFG intensity $\nu 20b/\nu 2$ as a function of crystallization time (ssp polarization). D. Ratio of the SFG intensity $\nu 7b/\nu 2$ as a function of crystallization time (ssp polarization). Here, we note that, to account for the surface heterogeneity, the intensity ratios are based on the average of 24 to 52 spectra per crystallization time. Error bars represent the standard error. 90

Figure 5.7. Scheme of iPS lamellar orientation A. flat-on. B. edge-on..91

Figure 5.8. A. Scheme of crystalline structure of iPS, according to Natta et al.[244], for a flat-on crystalline orientation. B. Zoomed regions of the 3_1 helix of iPS, showing the angles between the $C2$ symmetry axes of the $CH2$ (θb) and phenyl ring groups (θ) with the surface normal. 92

Figure 5.9. A. Scheme of crystalline structure of iPS, according to Natta et al.[244], for an edge-on crystalline orientation. B. Oppositely oriented iPS phenyl groups are shown with the same frame color. 93

Figure 5.10. SFG spectra of iPS thin films: amorphous (black) and crystallized at 180 °C for 16h (red). A. ssp polarization, B. ppp polarization, C. Phenyl ring vibrational frequency region of ssp spectra fitted with Equation 5.1, D. Phenyl ring vibrational frequency region of ppp spectra fitted with Equation 5.1 and E. Backbone vibrational frequency region of ssp spectra fitted with Equation 5.1. 95

Figure 5.11. Tilt angle analysis of the pendant phenyl ring of iPS. Solid black curves represent the plots of A. Equation C1 (Method 1) and B. Equation C2 (Method 2), for different values of the tilt angle distribution width (σ = 1°, 15°, 30°). The shaded regions represent the experimental ratios of amplitudes and their standard error. Grey regions represent the amorphous sample, and the red regions represent the 16 h semi-crystalline films. The overlap of the shaded regions with the solid back curves represents possible values for θ and σ. 96

Figure 5.12. A. AFM height images of the iPS films crystallized at 180°C 2.5 h (5 µm x 5 µm), B. Zoomed region shown in a. in a red square, B. Height profile obtained over the arbitrary line 1, shown in B. 97

List of Tables

Table 3.1 Molecular weight and PDI of PS samples. 34

Table 3.2. Fitting parameters of the phenyl ring C-H stretch region in ssp and ppp polarization*43

Table 4.1. Adsorption parameters for PS adsorption on mica 62

Table 4.2. Adsorption parameters for PS adsorption on a hydrophobic substrate, varying the chain's initial conformation. 65

Table 4.3. Range of possible values of tilt angles for PS films 69

Table 5.1. Possible values of tilt angle assumed by the pendant phenyl ring of iPS at the iPS/air interface. 96

Chapter 1 . Introduction

In polymer thin films, the small thickness (nm - µm) results in a high interfacial area-to-volume ratio, making the interfacial region critically important. This region not only governs typical interfacial processes but also significantly influences the bulk properties of the films. This interfacial region leads to significant differences in chain conformation and local organization compared to the bulk. For instance, substantial differences in polymer chain conformation are reported just a few nm away from the interface[1]. Furthermore, the number of entanglements[2], the local concentration of specific groups[3], and the relaxation dynamics[4] of interfacial chains differ markedly from those in the bulk region. In this context, achieving a deeper molecular-level understanding of the interfacial properties is fundamentally important for improving thin films performance and stability, and for advancing numerous technological applications.

The conformation of polymer chains near interfaces depends on various factors. For example, polymer properties such as the polymer molecular weight [5] and the polymer concentration in polymer blends[6] are critical determinants of interfacial chain conformation. Environmental factors including the presence of a substrate, also play a significant role in shaping the interfacial chain conformation. Numerous studies have highlighted substantial differences in chain conformation at the surface versus the buried interface of polymeric thin films[7,8]. Additionally, the surface energy of the substrate and the sample history[9,10], such as the preparation conditions, are key factors that influence the local conformation of polymer chains[11]. Given the complexity of these variables, systematic studies are essential to understand their effects on interfacial polymer chain conformation and to establish a connection between local conformation, film properties, and macroscopic behavior.

One of the most advanced analytical techniques for studying the conformation of interfacial polymer chains is sum frequency generation (SFG) spectroscopy[12–14]. This non-destructive vibrational spectroscopy offers exceptional interface specificity, on the scale of a few nanometers, enabling the analysis of both the level of ordering and the net orientation of interfacial groups. A key advantage of SFG is its unique ability to probe buried interfaces, such as those between a thin film and its substrate, significantly broadening its applicability compared to other techniques.

Beyond its role in fundamental research, such as determining molecular conformation in diverse environments[5,15–18], SFG spectroscopy has proven to be a powerful technique in applied studies, where molecular insights are directly connected to film properties. For example, SFG has been utilized to investigate adhesion[11], dewetting[19], and the thermal behavior[4] of thin films. These studies highlight the potential of SFG spectroscopy as a powerful tool for obtaining molecular-level insights of critical polymer processes, but its application to certain critical processes remains largely untapped.

Through innovative approaches, this research employs SFG spectroscopy in combination with other analytical methods and with theoretical studies to establish correlations between interfacial chain conformation and the macroscopic behavior of thin films. To achieve this, we investigated key factors, including polymer properties (e.g. molecular weight), interface characteristics (e.g. free vs buried interfaces), and the thermo-mechanical history of the sample. Furthermore, this study explores new frontiers in polymer science that have not yet fully benefited from the molecular-level insights provided by SFG spectroscopy, with the goal of expanding its applications in the field. This study aims to bridge the gap between molecular-level understanding and practical applications, offering valuable insights for both academic research and industrial innovations in polymer science.

1.1. Thesis structure and objectives

This research leverages SFG spectroscopy to investigate the conformation of interfacial polymer chains in polystyrene thin films, aiming to enhance the understanding of polymer chain behavior and its influence on thin film properties. The specific objectives of this study are as follows:

1. **Analyze polymer conformation near metallic substrates:** Investigate the conformation of polymer chains near a strongly interacting metallic substrate and examine how the polymer molecular weight affects interfacial conformation.
2. **Examine interfacial environment effects:** Explore the influence of the interfacial environment (free surface vs. buried interface) on chain conformation across a range of polymer molecular weights.

3. **Correlate chain conformation with thin film macroscopic behavior:** Establish a link between interfacial chain conformation and the macroscopic behavior of thin films, with a focus on their dewetting behavior.

4. **Expand applications of SFG spectroscopy in polymer science:** Identify new opportunities in polymer science where the molecular-level insights provided by SFG spectroscopy can drive significant advancements.

This thesis is organized into six chapters, each summarized below:

- **Chapter 1:** Provides an overview of the research field, outlines the objectives, and describes the structure of the thesis.
- **Chapter 2:** Offers a comprehensive review of relevant literature, discussing key concepts and prior studies pertinent to this research.
- **Chapter 3:** Provides research results and discussion regarding the investigation of the effects of polymer molecular weight on the interfacial conformation of polystyrene chains near a silver substrate. A hypothesis is proposed to explain the observed conformations, based on the balance of enthalpy and entropy during adsorption. This chapter is presented as an unaltered published journal article.
- **Chapter 4:** Builds upon the findings of Chapter 3 by examining polymer chain conformations near strongly interacting mica substrates and the free surface of polystyrene films across various molecular weights. Theoretical calculations of entropy and enthalpy during polymer adsorption are performed to assess dewetting tendencies based on interfacial chain conformation. Additionally, this chapter establishes a correlation between interfacial chain conformation and the dewetting behavior of thin films. It is presented as a journal article to be submitted for publication.
- **Chapter 5:** Explores the pioneering application of SFG spectroscopy to determine the lamellar orientation at the surface of polystyrene thin films. This study demonstrates the potential of SFG spectroscopy in advancing new areas of polymer science. This chapter is presented as an unaltered published journal article.
- **Chapter 6:** Summarizes the main findings of this research and offers recommendations for future studies.

Chapter 2 . Literature Review

This chapter outlines the foundational concepts and methodologies related to this research and provides a comprehensive review of relevant literature.

2.1. Structure and properties of polystyrene

Polystyrene is a thermoplastic polymer that possesses properties that make it highly attractive for a variety of industrial applications. It is a clear and transparent material with a glassy state at room temperature, softening at temperatures above 100°C. Known for its high mechanical strength, polystyrene can be easily molded into various forms, dissolved in solvents, and fused to create foamed materials. These characteristics, combined with its versatility, have made polystyrene one of the most employed aromatic thermoplastics in the industry, particularly in the packaging industry and as thermal insulator in the construction industry[20]. Beyond its traditional use as a basic plastic, styrene has been combined with other monomers to produce novel copolymers with improved and specialized properties[21].

The structure of polystyrene consists of a carbon backbone with pendant phenyl groups. Its classification is determined by its tacticity, which refers to the spatial arrangement of the phenyl groups along the polymer chain. Atactic polystyrene (PS) is an amorphous polymer characterized by the random distribution of phenyl groups on either side of the chain (Figure 2.1.A). In contrast, syndiotactic polystyrene (sPS) and isotactic polystyrene (iPS) are semicrystalline polymers, where each phenyl group adopts alternating or the same spatial arrangement relative to the backbone, respectively (Figure 2.1.B and C).

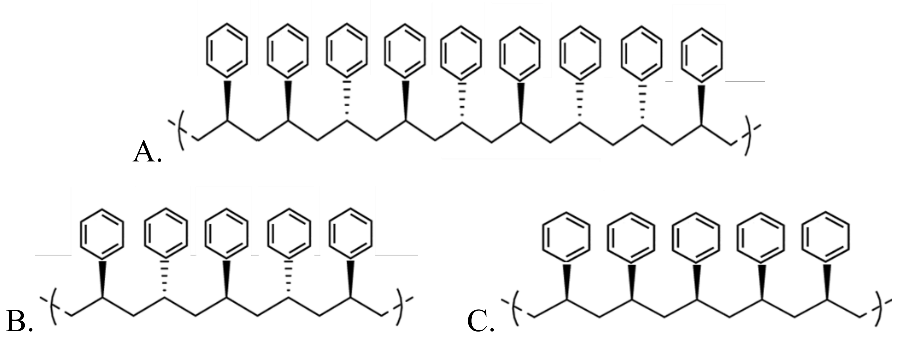

Figure 2.1. Structure of polystyrene. A. Atactic polystyrene; B. Syndiotactic polystyrene; and C. Isotactic polystyrene.

Polystyrene was selected as the model polymer for this study due to its structure and practical relevance. The presence of both a carbon backbone and an aromatic side group in its structure enables the extrapolation of the research findings to other polymers with similar structural elements. Additionally, polystyrene's extensive industrial use enhances the practical significance of the study's results. Isotactic polystyrene (iPS), in particular, is a slow crystallizer, making it ideal for tracking the crystallization process using SFG spectroscopy. Furthermore, the extensive literature available on PS SFG analysis[1,5–9] provides a solid foundation for data interpretation and facilitates comparisons with previous research.

2.2. Polymer molecular weight

Polymers do not have a single molecular weight but instead exhibit a molecular weight distribution. Their molecular weight characteristics are typically described by the average molecular weight and the molecular weight distribution. Both of these parameters play a crucial role in determining various properties of polymers. The average molecular weight of polymer materials is typically represented by the number average molecular weight (Mn) and the weight average molecular weight (Mw)[22]. The equations for calculating Mn and Mw are presented in Equation 2.1 and Equation 2.2, where i is the number of polymer chains and N_i is the number of chains with the molecular weight M_i. For linear polymers, the chain molecular weight is directly related to the chain length and to the degree of polymerization, and these terms can be interchanged in some contexts. In these instances, we refer to the polymer molecular weight as M indicating that we are discussing the general concept of chain length and degree of polymerization, rather than specifically distinguishing between Mn and Mw.

$$Mn = \frac{\sum_i N_i M_i}{\sum_i N_i} \qquad \text{Equation 2.1}$$

$$Mw = \frac{\sum_i N_i {M_i}^2}{\sum_i N_i} \qquad \text{Equation 2.2}$$

Polymers can be produced with narrow, broad, or even bimodal molecular weight distributions. The breadth of the molecular weight distribution is quantified by the polydispersity index (PDI). The polydispersity index is defined as Mw/Mn and a higher PDI indicates a broader distribution.

2.2.1. Effect of polymer molecular weight on bulk and interfacial polymer properties

The molecular weight is one of the most important characteristics that determines the polymer behavior. An important parameter that scales with M is the density of entanglements N_e. Equation 2.3 shows the relationship between N_e and M, where M_e is the molecular mass between entanglements[23]. As polymer chains become longer, the likelihood of physical entanglement increases, creating a network that resists deformation and enhances mechanical strength.

$$N_e \propto \frac{M}{M_e} \qquad \text{Equation 2.3}$$

As a result of the increased density of entanglements, an increase in M generally leads to a corresponding rise in the viscosity of polymer melts. According to the pure reptation models proposed by Brochard and de Gennes[24], the polymer bulk viscosity η under ideal conditions, scales with M as $\eta \propto M^3$. However, more recent models and experimental results have shown that $\eta \sim M^{3.4}$, when additional factors related to the complexity of chain dynamics are taken into account[25,26]. Both the viscosity and degree on entanglements directly affects a polymer's mechanical and flow properties.

Molecular-level parameters that vary with molecular weight, such as the number and the strength of intermolecular and intramolecular interactions, make molecular weight a critical factor in determining the bulk properties of polymers. For example, the solid-state properties such as the tensile strength, the modulus of elasticity, the impact resistance and the toughness[27,28], as well as the molten-state properties such as the viscosity and rheological properties[29,30] are dependent on the chain molecular weight. Solid-state polymer mechanical properties typically improve as molecular weight increases, but this effect plateaus beyond a certain point, with further increases having minimal impact[31]. However, substantially high molecular weight often means reduced processability, as it leads to increased viscosity in the polymer melt. Due to the differences in chain mobility, the molecular weight significantly affects the thermal properties and the crystallization behavior of polymer materials, including the crystallization temperature, degree of crystallinity, nucleation and growth rate and even the chain conformation during crystallization[32,33].

In addition to its significant impact on the bulk properties of polymers, molecular weight and molecular weight distribution also play a crucial role in determining interfacial properties, influencing key interfacial processes in polymer science. For example, interfacial (and surface) tension tends to increase with molecular weight[34–36], directly affecting processes such as wetting[37] and the compatibility of polymers in blends. The dependence of surface tension on molecular weight can be attributed to molecular-level factors. At the surface, molecules experience an asymmetric environment, resulting in fewer possible interactions compared to the bulk. Consequently, surface tension is intrinsically tied to the cohesive forces acting on surface polymer chains. High molecular weight polymers exhibit stronger intermolecular and intramolecular interactions per chain, increasing the energetic cost of the molecular rearrangements required to create an interfacial region.

Entropic contributions also play a significant role in determining the dependence of surface tension on the polymer molecular weight. In the bulk, polymer chains generally adopt a random coil conformation, with their radius of gyration (R_g) increasing with molecular weight (Figure 2.2A and C). However, in the confined surface region, where the thickness is typically around 1 nm, the density gradient between the surface and the bulk prevents high molecular weight chains from maintaining their expanded coil conformation. This occurs when the surface region thickness is smaller than the bulk radius of gyration of the polymer. Instead, these chains must undergo conformational rearrangements to fit within this restricted space, incurring a substantial entropic penalty (Figure 2.2. B). In contrast, low molecular weight chains experience less pronounced conformational constraints at the interface (Figure 2.2. D), leading to a lower entropic cost compared to their high molecular weight counterparts[38]. The increased entropic penalty for high molecular weight chains at the interface creates a stronger tendency for these chains to minimize their presence in the interfacial region. This behavior drives the polymer to reduce its surface area, ultimately resulting in higher surface tension for polymers with higher molecular weights. The differences in the entropic penalties experienced by interfacial polymer chains, based on molecular weight, lead to the preferential segregation of low molecular weight chains to the interfacial region in polydisperse materials, thus effectively reducing the polymer interfacial tension[39,40].

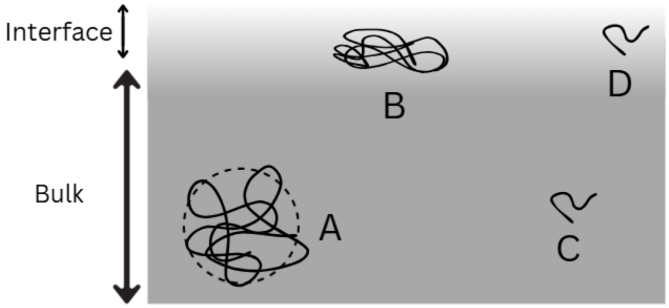

Figure 2.2. Chain conformations of polymers in the bulk and surface regions. A. High molecular weight polymer adopting a random coil conformation in the bulk, with the dashed circle representing the radius of gyration. B. High molecular weight polymer rearranged into a restricted conformation to fit within the narrow interfacial region. C. Low molecular weight polymer adopting a random coil conformation in the bulk; and D. Low molecular weight polymer conforming more easily to the surface region. Adapted from [38].

Evaluating the effect of polymer molecular weight on interfacial properties at buried interfaces is considerably more challenging than at free surfaces. This is primarily due to the limitations of analytical techniques for probing buried interfaces and the increased complexity arising from multiple factors that influence the energy balance at the buried interface, such as the type and strength of polymer/substrate interactions. For instance, in polymer thin films, the thickness of the adsorbed layer with restricted chain mobility has been reported to increase with polymer molecular weight[41,42]. In contrast, an opposite trend was observed in composite systems containing nanoparticles, where the adsorbed layer thickness decreased with increasing molecular weight. This discrepancy is likely due to differences in equilibrium times and the degree of chain packing[43]. These findings highlight the need for systematic studies to explore how polymer molecular weight influences buried interfacial properties. Such investigations can provide critical insights into the relationship between interfacial chain conformation and the macroscopic behavior of thin films.

2.2.2. Effect of polymer molecular weight on interfacial processes

Variations in interfacial properties, such as surface tension and surface chemical composition, have a direct impact on critical interfacial processes. For instance, the energy of adhesion is highly dependent on polymer molecular weight. Beyond intrinsic factors like the nature and strength of interactions, key parameters such as the density of entanglements and interfacial diffusion—both of which are functions of molecular weight—play a pivotal role in defining the adhesion characteristics of materials[44–46].

Slip, which occurs when the velocity of the polymer melt in the vicinity of the wall is nonzero, is strongly influenced by both the polymer molecular weight and molecular weight distribution[47]. Briefly, the slip mechanism in polymer melts is governed by the behavior of the polymer chains in the first monolayer near the wall. These chains are adsorbed to the wall and entangled with the bulk chains. When slip arises from the detachment or desorption of chains from the wall, it is referred to as adhesive failure or true slip. On the other hand, cohesive failure or apparent slip occurs when the adsorbed chains disentangle from the bulk chains. In the case of partial disentanglement, weak slip is observed, while the strong slip regime is characterized by complete disentanglement, where the adsorbed chains align in the direction of flow [48].

In their model for true slip of monodisperse entangled chains, Brochard and de Gennes demonstrated a significant molecular weight dependence of the slip length b, reporting that $b \propto M^3$. This scaling relationship arises in part from the molecular weight dependence of viscosity, which also scales as $\eta \propto M^3$ in the Brochard and de Gennes model. Similarly, in the weak slip regime, Mhetar and Archer[49] found a slip length relationship of $b \sim M^2$ for a series of polybutadienes with varying molecular weights. The molecular weight distribution also plays a critical role in slip behavior. For instance, Sabzevari et al. demonstrated that the presence of low molecular weight chains significantly enhances slip in highly entangled polymers [47]. It is important to note that are various other factors, such as the surface properties and the sample thermo-mechanical history that may influence the molecular weight influence on slip[50].

The wetting behavior of polymers is influenced by several factors, including the polymer viscosity and surface tension and the interplay between the entropic and enthalpic contributions acting on the polymer chains adsorbed to the substrate. These factors are dependent on the polymer's molecular weight[36,51]. Zhang et al.[52] observed that the homogeneity of polyvinyl butyral thin films was closely tied to the polymer's molecular weight, with high molecular weight polymers producing smooth, uniform films, while low molecular weight polymers resulted in inhomogeneous roughness or in dewetting. In Chapter 4, the effect of molecular weight on the dewetting behavior of polymer films will be examined in detail. While many studies have explored this topic, other factors affecting dewetting such as surface properties, film thickness[53], chain architecture[54] and the sample thermo-mechanical history[50], complicate the development of a single, unified correlation between molecular weight and wetting behavior.

2.3. Polymer thin films

Polymer thin films have a thickness ranging from nanometers to few micrometers. These materials are crucial in various technological applications, and their applicability will continue to rise as the demand for smaller devices increases. These films are characterized by a high surface-area-to-volume ratio, which significantly enhances their surface-related properties and interactions compared to bulk materials.

2.3.1. The influence of thin film thickness on its properties

The thickness of a polymer thin film is a critical parameter that significantly influences its properties. Small variations in thickness can lead to substantial changes in the surface-area-to-volume ratio and in the degree of confinement experienced by polymer chains within the film. While some properties such as the Young's modulus seem to be generally independent of the film thickness[55], others, including wetting behavior, thermal characteristics, and optical properties, are highly dependent on the thickness of the film. Achieving the optimal thickness is essential for balancing functionality and stability in thin-film applications.

The stability of thin films in terms of resistance to dewetting is particularly sensitive to changes in thickness[56]. Generally, the film stability decreases with decreasing the film thickness[57]. Rehse et al.[53] reported a critical thickness below which polystyrene thin films deposited on silicon substrates exhibit dewetting behavior. This critical thickness increases with the polymer molecular weight (critical thickness $< 0.55\ R_g$). When film thickness falls below this critical value, the increased level of confinement results in an elevated free energy of the polymer chains. To minimize their free energy, these chains migrate to thicker regions of the film, ultimately leading to dewetting.

The mobility and relaxation dynamics of polymer chains vary depending on their position within the film, typically forming a gradient along the direction normal to the film thickness[58].

Surface chains exhibit the highest mobility, followed by bulk chains, while chains in contact with the substrate display significantly reduced mobility. Variations in chain mobility depending on their location within the film lead to differences in thermodynamic behavior. Wang et al.[59] proposed a three-layer model for the glass transition temperature (T_g) in thin films, as illustrated in Figure 2.3. Consequently, as the thickness of a thin film decreases, the contribution of highly mobile surface chains to the overall film volume increases, often leading to a reduction in the bulk T_g of the films[57]. However, in the presence of strong interactions between the substrate and the polymer, T_g may increase with decreasing the film thickness[59]. Li et al.[4] examined this phenomenon in poly (methyl methacrylate) (PMMA) films deposited on a metallic substrate. The authors observed a decrease in T_g as the film thickness was reduced. To investigate the role of the free surface, the authors sandwiched the PMMA films between a metallic substrate and a silica optical window, effectively eliminating the free surface. Under these conditions, T_g increased significantly as the film thickness decreased, highlighting the critical role of interfacial chain mobility in determining the bulk thermal properties of thin films.

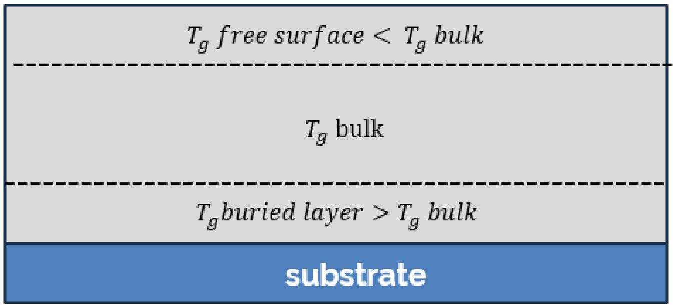

Figure 2.3. Model of 3-layer T_g variations in thin films when there are strong interactions between the polymer and the substrate. Adapted from[59]

Key optical properties of thin films, such as the absorbance spectrum, absorption coefficient, and refractive index, are influenced by the film thickness[60,61]. Light interference in thin films also depends on thickness, occurring due to multiple reflection and refraction of light at the top and bottom interfaces of the film. These light beams can interact constructively or destructively, modifying the intensity of the local fields at the interfaces and sometimes producing colorful patterns based on the wavelength and film thickness[62]. This phenomenon is particularly valuable in spectroscopic studies[63] as it enables selective analysis of specific film interfaces due to interference effects[64].

2.3.2. Polymer thin films fabrication methods

Thin films can be fabricated using a wide range of techniques, with the selection of the most suitable method determined by the specific application requirements, as well as factors like time efficiency, equipment availability, and cost considerations. Most of these methods such as dip coating, spray coating, solvent casting and spin coating utilize polymer solutions, allowing the control over film thickness by adjusting the polymer concentration and employing multiple coating cycles. Moreover, multiple cycles can be utilized to produce multilayer coatings with different polymers, enhancing the versatility and functionality of thin films for diverse applications[65].

Solvent casting is one of the simplest methods for producing thin films. The process involves pouring a polymer solution onto the surface of a substrate and allowing it to dry[66]. The drying rate can be controlled by adjusting ambient conditions such as temperature and atmospheric composition. One of the primary advantages of this method is its relatively slow drying rate compared to other techniques. This extended drying time allows for greater relaxation of the polymer molecules, effectively minimizing residual stresses compared to fast drying methods such as spin coating[67].

One particularly versatile method for coating substrates with complex shapes is dip coating. This technique is highly effective for producing high-quality coatings on substrates with intricate geometries, including porous structures, samples with holes, and complex patterns[68]. The process involves immersing the substrate into a polymer solution, allowing it to remain submerged for a set period, and then withdrawing it to drain and dry[69], as shown in Figure 2.4.A. This method is suitable for both laboratory-scale applications and industrial-scale production of large films, as it can be integrated with processes like roll-to-roll manufacturing for enhanced scalability[70]. However, it is important to note that the substrates used in roll-to-roll process are limited to flexible sheets or films. The uniformity of thin films is strongly influenced by the viscosity of the polymer solution and the wetting behavior of the polymer on the substrate.

Spray coating is an effective technique for producing high-quality polymer thin films, with applications in various technological fields, such as the fabrication of polymer solar cells[71]. In this method, a fine aerosol of polymer solution is sprayed directly onto the substrate (Figure 2.4. B). Spray coating offers significant potential for large-scale production, with reduced material waste compared to techniques like spin coating. A key advantage of spray coating is its adaptability to substrates of various sizes and shapes, including large, rigid, and complex geometries. However, achieving uniform thin films remains a challenge. The solvent properties, such as vapor pressure, boiling point, and surface tension, play a critical role in determining film homogeneity. To enhance uniformity, it is often necessary to use a solvent mixture that optimizes these properties[72].

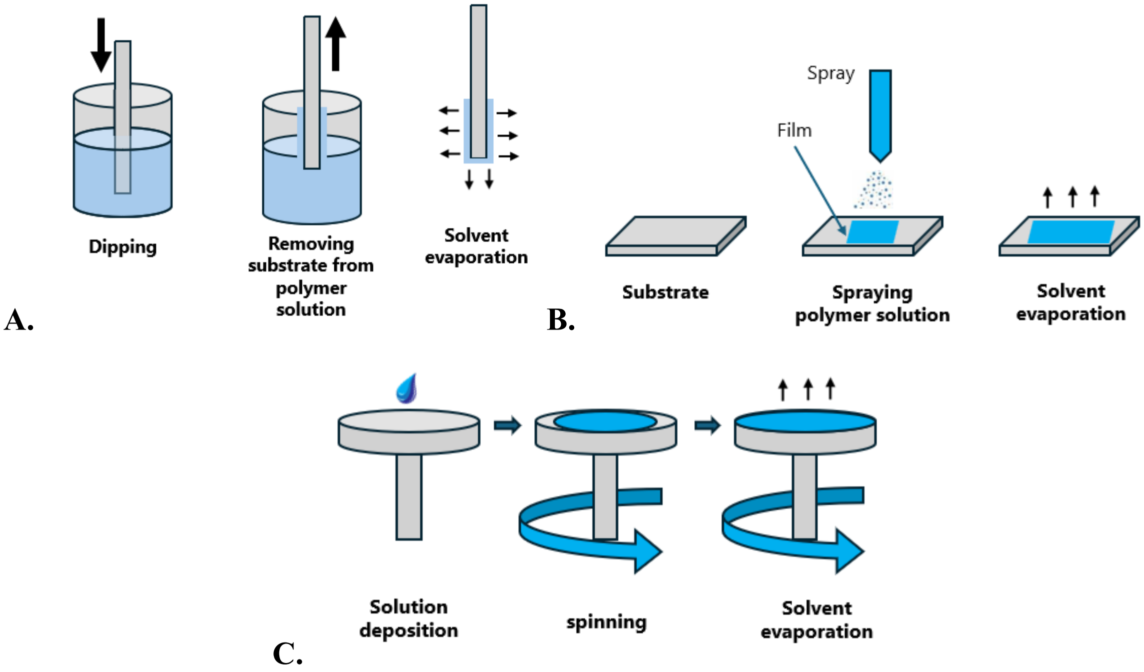

Figure 2.4. Scheme of polymer thin film fabrication methods. A. Dip coating; B. Spray coating and C. Spin coating. Adapted from[69,73].

Spin coating is a widely used technique for producing uniform polymer thin films. In this method, a small volume of polymer solution is poured onto the center of a substrate, which is then rapidly rotated at high speeds (typically 1,000–10,000 rpm). The centrifugal force spreads the solution evenly across the substrate's surface, while excess solution is expelled (Figure 2.4. C). The primary limitations of spin coating are related to substrate size and shape. This technique is generally suited for small, flat substrates, as achieving high-speed spinning on larger substrates presents significant challenges in terms of equipment design and process stability[69]. The rapid solvent evaporation and the strong centrifugal forces during spin coating often lead to the formation of residual stresses in the film, as the polymer chains adopt out-of-equilibrium conformations[67]. These residual stresses can cause various issues, such as delamination, dewetting, and other defects[74]. To mitigate these problems, annealing processes are commonly employed to facilitate chain relaxation and reduce residual stresses in spin-coated films. Despite these challenges, spin coating is the most widely used thin film fabrication method for SFG studies[3,75–77] because it produces thin films with exceptionally smooth surfaces and homogeneous thickness with high reproducibility, which are essential for minimizing unwanted reflections, interference variations, and other optical artifacts that can affect the accuracy and sensitivity of SFG measurements.

Solvent-free methods including chemical vapor deposition and physical vapor deposition are also available for thin film deposition, offering unique advantages. For example, in chemical vapor deposition monomers are vaporized and polymerized directly on the substrate surface. The key advantages of these methods include precise control over film thickness, compatibility with insoluble polymers, and the elimination of potential solvent damage to the substrate[78]. These techniques also enable the formation of films that are chemically bonded to the substrate, by employing substrates with self-assembled monolayers[79].

2.3.3. Free standing polymer thin films

Polymer thin films are generally produced and utilized on a supporting substrate. This reliance on a substrate is due to their extremely thin structure, which lacks the mechanical strength needed to maintain integrity independently, leading to risks of tearing, shrinking, or collapsing. However, innovative methods have been developed to create free-standing polymer thin films. These methods are important as they allow the mechanical testing of the films without the interference from the substrate[80,81] and enable the transfer of films from one substrate to another after fabrication.

One effective approach for producing free-standing films involves the use of sacrificial mica substrates[50]. Mica presents atomically flat cleavage planes that provide minimal physical anchoring for the films, making it an ideal substrate for this purpose. By employing a flotation method, the thin films can be gently detached from the mica substrate and floated onto a liquid bath, typically water, for subsequent use or substrate transfer. Alternative methods involve the use of other sacrificial substrates that can be later dissolved or chemically removed from the film[80].

2.4. Crystallization in polymer thin films

Polymer crystallization plays a pivotal role in defining the key solid-state characteristics of polymer-based materials. In various polymer applications, such as in polymer molding and coating, crystallization takes place in direct contact with a surface or substrate. When a polymer crystallizes in the presence of an external surface, it can lead to heterogeneous nucleation at the polymer-surface interface. This effect modifies the usual crystallization kinetics and crystalline structure, compared to homogeneous nucleation that occurs in the bulk without the presence of a substrate[82,83]. Crystallization in polymer thin films differs significantly from bulk crystallization, with both the crystallization kinetics and crystalline morphology being substantially influenced by confinement effects. Their extremely high interfacial area-to-volume ratio results in a significantly larger proportion of the material being in contact with the substrate during crystallization compared to bulk materials. Consequently, the influence of the substrate on nucleation and crystallization becomes a critical factor in shaping the crystallization behavior of thin films. These changes have a great impact on the optical, electrical[61], and mechanical[84] properties of the thin films, thus affecting their performance in various applications.

2.4.1. Comparison of homogeneous and heterogeneous nucleation

During homogeneous nucleation, random molecular oscillations lead to the formation of small clusters of aligned chains. Once these clusters exceed the critical nucleus size, they become stable and serve as seeds for further crystal growth. These nuclei are spherical, and the energy barrier for homogeneous nucleation is determined by the balance between the volume energy gain and the surface energy cost associated with forming the nucleus, as shown in Equation 2.4[85], where, $\Delta G_{Homogeneus}$ is change in the total Gibbs free energy of homogeneous nucleation, σ_c is the crystal surface energy, r_n is the radius of the spherical nucleus and G_V is the volume free energy per volumetric unit.

$$\Delta G_{Homogeneus} = 4\pi {r_n}^2 \sigma_c - \frac{4}{3}\pi {r_n}^3 G_V \qquad \text{Equation 2.4}$$

In contrast, the presence of a foreign surface during crystallization may function as seeds for polymer chain alignment, thus facilitating nucleation. The nucleus forms at the interface between the polymer and a substrate. Instead of a complete sphere, the nucleus takes the shape of a spherical cap. The extent of this cap, or how much of the sphere is formed, depends on the contact angle between the nucleus and the surface[86] (Figure 2.5). As a result, the contributions of surface energy and change in volume to the total energy barrier for heterogeneous nucleation are smaller than those for homogeneous nucleation.

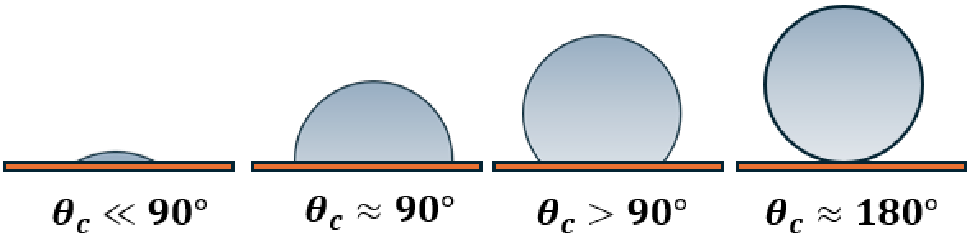

Figure 2.5. Size of heterogeneous nucleus as a function of the contact angle θ_c. Adapted from[87].

The relationship between the total Gibbs free energy for heterogeneous nucleation, $\Delta G_{Heterogeneous}$, and homogeneous nucleation, $\Delta G_{Homogeneous}$, is given by Equation 2.5, where $f(\theta_C)$ is a parameter that depends on the contact angle θ_c as expressed in Equation 2.6[88]. The parameter $f(\theta_C)$ ranges from 0 and 1, increasing as θ_c increases. For low θ_c values, $\Delta G_{Heterogeneous} \ll \Delta G_{Homogeneous}$, making nucleation more favorable at the polymer/substrate interface than in the bulk. This occurs because the nucleus formed during heterogenous nucleation has a smaller surface area compared to the full sphere formed during homogeneous nucleation (Figure 2.5 and Figure 2.6). As θ_c increases, the surface area of the nucleus grows, as the shape approaches a full sphere close to nonwetting conditions $\theta_c \approx 180°$ and $\Delta G_{Heterogeneous} \approx \Delta G_{Homogeneous}$.

$$\Delta G_{Heterogeneous} = f(\theta_c) * \Delta G_{Homogeneous} \qquad \text{Equation 2.5}$$

$$f(\theta_C) = \frac{(2+\cos\theta_C)(1-\cos\theta_C)^2}{4} \qquad \text{Equation 2.6}$$

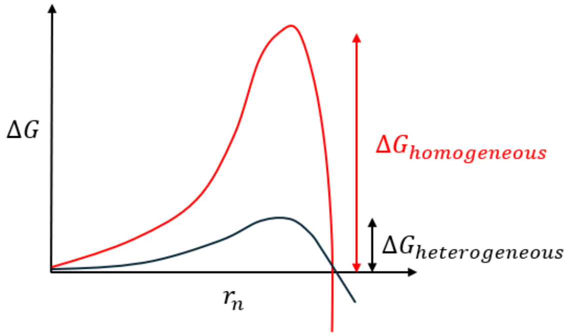

Figure 2.6. Change in the Gibbs free energy for homogeneous and heterogeneous nucleation.

2.4.2. Influence of substrate properties on polymer nucleation

Surface properties play a pivotal role in driving heterogeneous nucleation, significantly shaping the crystallization behavior of polymer thin films. Factors such as surface energy, roughness, and crystallinity influence the nucleation rate, crystal orientation, and morphology at the polymer-substrate interface. For example, higher surface roughness often promotes nucleation by concentrating thermal stresses on surface irregularities during cooling, leading to a local chain alignment. Lin et al.[89] reported a reduction in the nucleation induction time and a higher degree of crystallinity for isotactic polypropylene samples in contact with copper sheets with increasing the roughness of the substrate. However, this behavior can be influenced by other factors that also impact nucleation.

The surface energy of the substrate significantly impacts heterogeneous nucleation. This is because the substrate surface energy influences the wetting behavior of the polymer on the substrate. Generally, higher substrate surface energy results in a lower contact angle between the nucleus and the substrate, thereby decreasing the energy barrier for nucleation[90], as shown in Equation 2.5 and Equation 2.6.

The crystallinity of the substrate is also a key factor influencing nucleation. A comprehensive study of Chatterjee et al.[91] explored the nucleation behavior of polymer melts in contact with various surfaces. Their findings revealed that crystalline substrates exhibit significantly higher nucleation rates compared to amorphous surfaces, even among materials with similar chemical compositions. For example, isotactic polypropylene demonstrated transcrystalline growth (highly ordered crystalline layer at the interface between a polymer and a substrate, where the polymer crystals grow perpendicular to the substrate surface) on semi-crystalline iPS surfaces, while amorphous PS showed limited nucleation ability for the polymer. Crystalline substrate may also lead to a phenomenon called epitaxial growth[82,92], which occurs when a crystal grows on an existing crystalline surface, adopting a specific orientation influenced by the template. Depending on the system, the polymer chains may align parallel to the substrate's crystalline structure or at a characteristic angle. This phenomenon provides compelling evidence of molecular-level interactions that guide the orientation and arrangement of polymer chains during crystallization.

2.4.3. Crystallization in confined systems

In bulk materials the size of the crystalline spherulites typically ranges from microns to millimeters[93]. In thin films, the reduced thickness inhibits the isotropic growth of spherical spherulites. Consequently, the crystallization, that is predominantly initiated at the polymer-substrate interface, leads to the formation of crystals with specific lamellar orientations relative to the substrate[59,93]. The two primary lamellar orientations are edge-on and flat-on, where the polymer chain axes align parallel and perpendicular to the substrate plane, respectively, as illustrated in Figure 2.7 A. Various factors influence the formation of edge-on or flat-on lamella. For instance, the mechanical history of the film, including features like scratches or rubbed areas that can locally align polymer chains, increasing the nucleation rate and promoting a preferred edge-on lamellar orientation in these regions [94].

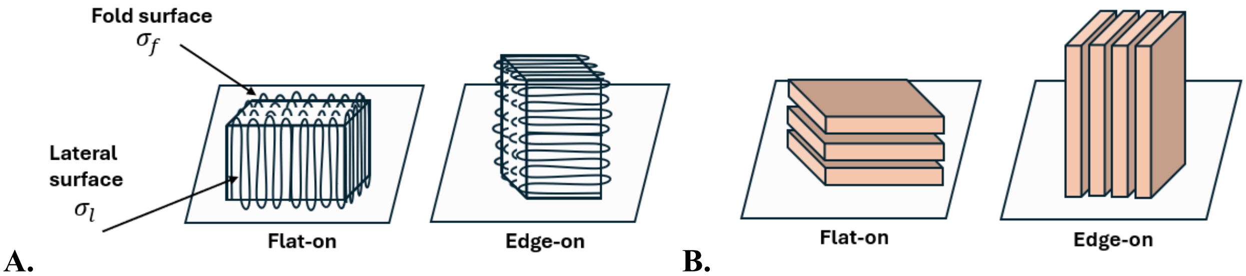

Figure 2.7. Lamellar orientation of polymer crystals in thin films. A. Scheme showing the chain arrangement within the crystalline lamella; and B. Scheme showing the lamellar packing, which results in different surface topographies.

The chain folding process that forms the lamella results in two distinct surfaces: the fold surface and the lateral surfaces (Figure 2.7 A). The surface energy of the lateral surface (σ_l) is significantly smaller that of the fold surface (σ_f)[93]. This greatly influences the lamellar orientation in thin films. For instance, when nucleation occurs at the air interface, an edge-on orientation is typically favored because it minimizes the system's overall surface energy[93]. However, in thin films, the edge-on lamellae grow in a direction perpendicular to the film thickness. This growth may be hindered in such confined systems, potentially favoring the formation of flat-on lamellae instead. Furthermore, the edge-on lamella results in a much larger interfacial area, which typically favours the formation of flat-on lamella in thin films (Figure 2.7 B)[93]. Wang et al.[59] observed an increase in the concentration of edge-on lamella in thin films of poly(bisphenol A hexane ether) as the thickness of the films increased.

The crystallization temperature also plays a critical role in determining the lamellar orientation in thin films. Due to the differences in chain mobility and in the local T_g (Figure 2.3), at low temperatures, the homogeneous nucleation at the surface of the film is faster than the heterogeneous nucleation near the substrate, thus increasing the surface concentration of edge-on lamella[59,95]. At higher temperatures, the heterogeneous nucleation becomes dominant, and the concentration of flat-on lamella at the film surface is higher than that of the edge-on orientation[59,95]. There is an interesting interplay between the influence of the crystallization temperature and the film thickness in the final crystalline morphology of thin films. Wang et al.[59] observed that, for films sufficiently thick, there will be the formation of edge-on lamella at the film surface even at elevated temperatures. This occurs because the growth of flat-on lamellae initiated at the substrate interface takes considerable time to reach the surface, allowing sufficient time for homogeneous nucleation of edge-on lamellae in the surface region of the films. This observation highlights the possible differences in lamellar orientation between the surface and the substrate regions of thin films. Consequently, analytical techniques capable of probing lamellar orientation at both the surface and the buried interfaces are essential.

The lamellar orientation at the surface of semi-crystalline polymer thin films is often investigated using advanced analytical methods, including time-of-flight secondary ion mass spectrometry,[95] x-ray[96] and Atomic Force Microscopy (AFM). Among these methods, AFM remains the most widely utilized technique due to its straightforward ability to resolve differences in surface topography arising from distinct lamellar packings. In AFM images, flat-on lamellae typically appear as terrace-like structures, while edge-on lamellae exhibit fibril-like morphologies[94,97]. However, AFM is limited to examining free surfaces, necessitating the detachment of the film from its substrate to analyze buried interfaces [97]. This detachment approach is not only a destructive technique but also introduces potential alterations in the interfacial structure and morphology during the detachment process, potentially compromising the accuracy of the results. In this context, SFG spectroscopy is a promising non-destructive analytical tool for probing lamellar orientation in thin films at both free surfaces and buried interfaces without the need for physical separation. By working as a complement to AFM and other analytical techniques, the use of SFG spectroscopy can potentially contribute to addressing critical gaps in the analysis of lamellar orientation in semi-crystalline polymer thin films.

2.5. Interfacial chain conformation

The chain conformation in polymer films varies depending on the location of the chains within the film[1] (Figure 2.8). This variation arises due to differences in enthalpic and entropic contributions acting on the chains[98], as well as disparities in relaxation dynamics[10], free volume[99] and the degree of chain entanglement[2] throughout the film.

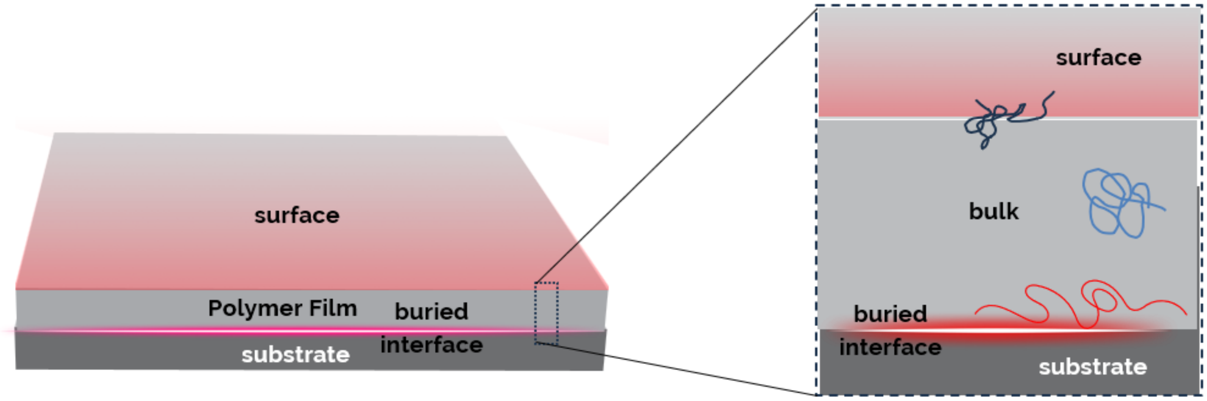

Figure 2.8. Scheme showing different polymer chain conformations throughout the thickness of a thin film.

The initial chain conformation of thin films is highly influenced by the fabrication method. For instance, the type of solvent used for preparing the polymer solution can significantly influence the interfacial chain conformation[9,100]. Furthermore, the film deposition technique is also of a critical importance. When spin-coating is used, the strong centrifugal forces combined with rapid solvent evaporation cause the polymer chains to be frozen in an out-of-equilibrium, extended conformation. For example, Tsuruta et al.[10] demonstrated significant differences in the conformation of polystyrene (PS) chains near a quartz substrate between films prepared by spin-coating and those produced via solvent casting, which is characterized by a slower solvent evaporation rate and the absence of centrifugal forces, allowing the polymer chains to relax into their most energetically favorable conformation. Out-of-equilibrium chain conformation may lead to various problems in thin films performance, such as in deformation and dewetting[100,101]. To reduce the influence of the film preparation method on the chain conformation, thin films are typically submitted to annealing to allow the relaxation of the chains.

2.5.1. The effect of annealing on the interfacial chain conformation

Polymer thin films are often annealed after deposition to relieve residual stresses and enhance their performance. The most commonly used method is thermal annealing, which involves heating the film above its bulk glass transition temperature (T_g) for a specified duration. Alternatively, solvent annealing can be employed, where the film is exposed to a solvent-rich atmosphere, allowing the polymer chains to reorganize and relax without the need for elevated temperatures[10,100]. Annealing conditions have a significant effect on the chain conformation, directly influencing the resulting film properties.

Due to differences in local relaxation dynamics and T_g (Figure 2.3), surface and bulk polymer chains relax more readily than those near the buried interface. The relaxation of surface chains can typically be done in shorter periods of annealing at temperatures close to or slightly above T_g[1,102]. In contrast, buried interfaces with slow relaxation dynamics require prolonged annealing times and temperatures significantly above T_g to change their interfacial conformation[19]. In fact, Tsuruta et al.[10] reported that PS chains near a quartz substrate remained unrelaxed even after annealing at temperatures nearly 100°C above the bulk T_g for 3 hours. Interestingly, the study revealed that these buried chains could be successfully relaxed using solvent annealing.

2.5.2. Surface vs buried chain conformation

The conformation of polymer chains near the surface and buried interfaces of polymer films exhibits significant differences. These differences occur in the conformation of the polymer backbone, as well as in the net orientation of specific groups. For instance, multiple studies across various systems have reported that the phenyl rings of PS are predominantly oriented along the surface normal at the film surface, while at the buried interface of the same film, they tend to align closer to the surface plane[7,8].

Near the air interface, polymer chains experience a loss of conformational entropy, which increases the system's free energy. Additionally, the energy change for each polymer segment in contact with air, rather than with another chain segment, is equivalent to the energy of evaporation and corresponds to an increase in internal energy. This effect, combined with the volumetric contraction caused by spatial restrictions at the interface (Figure *2.2*), results in chains near the free surface of polymer films tending to adopt a coiled conformation, minimizing the number of segments in contact with the free surface[103]. Entropic contributions are also responsible for the segregation of chain ends at the interfacial regions[104].

At the buried interface, the conformational entropy loss of the interfacial polymer chains can be balanced by the enthalpic gain from interactions between the polymer and the substrate. The interplay between entropic cost and enthalpic gain results in chain conformations that deviate from the isotropic, random-coiled configuration. The chain length plays a critical role in this balance. Longer chains can form a greater number of polymer-substrate interactions per chain, thereby maximizing their enthalpic gain, and often adopt an extended conformation when adsorbed onto substrates. In contrast, shorter chains, which can only make a limited number of polymer-substrate interactions, tend to retain a more isotropic conformation, with fewer segments anchored to the substrate[51].

Instead of simply promoting the relaxation of the buried chains, thermal annealing promotes the formation of an irreversibly adsorbed layer of polymer chains near the substrate, characterized by strong interactions and a tightly packed, flattened conformation. Adjacent to this layer lies a region of loosely adsorbed chains, which interact weakly with the substrate and adopt a more coiled, less densely packed conformation[19,41,105]. The conformation of these interfacial chains can be described by the tail-loop-train model (Figure 2.9), where the degree of packing and number of polymer-substrate interactions distinguishes the two layers.

The presence of an irreversibly adsorbed layer following prolonged thermal annealing has been extensively documented[1,19,41,64], often using the Guiselin[106] method. This technique involves subjecting the sample to extended thermal annealing, followed by multiple washing cycles in a good solvent to remove loosely adsorbed chains. The irreversibly adsorbed chains remain bound to the substrate, even after exposure to a good solvent for several days. Even though this strategy effectively demonstrates the existence of an irreversibly adsorbed layer, it does not provide reliable information with respect to the conformation of the chains near the substrate prior to solvent leaching. This is because exposure to solvents alters the interfacial conformation of the chains, potentially disrupting their original structure. Therefore, the development and application of analytical methods capable of directly probing buried chain conformations are crucial for gaining a deeper understanding of the molecular-level behavior of buried interfaces.

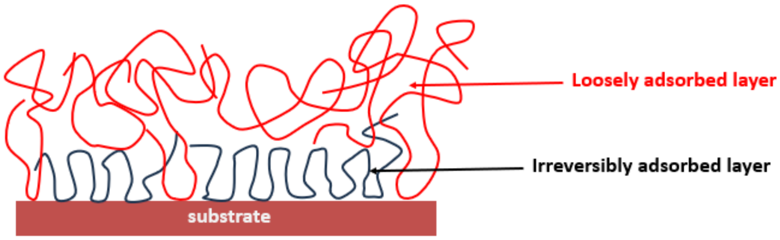

Figure 2.9. Scheme showing the formation of irreversibly adsorbed and loosely adsorbed polymer layers near the substrate. Adapted from[19,107].

2.5.3. System parameters influencing the interfacial chain conformation

Several parameters of the system, including surface characteristics and polymer properties, play a critical role in shaping the interfacial conformation of polymer chains. Factors such as surface energy, chemical composition, and roughness interact with polymer chain length, flexibility, chemical structure and molecular weight to dictate the resulting structure at the interface. Understanding how these parameters influence chain behavior is essential for tailoring the performance of thin films.

The molecular weight of a polymer is a critical factor influencing its interfacial chain conformation. It plays a key role in the enthalpic and entropic interplay during polymer adsorption and determines the extent of backbone extension at buried interfaces[51]. Additionally, differences in free volume at the free surface contribute to variations in the orientation of specific structural groups, such as phenyl rings. For instance, Bzeih et al.[5] demonstrated the impact of the molecular weight of PS on the tilt angle of its pendant phenyl rings at the PS/air interface. Their findings revealed that lower molecular weight PS samples adopt higher tilt angles due to increased free volume. However, research addressing the effect of the PS molecular weight on the chain conformation at buried interfaces is scarce.

Steric factors significantly influence the arrangement and packing of polymer chains, thereby impacting their interfacial conformation. Hong et al.[6] investigated the effect of the local concentration of phenyl groups on their interfacial orientation near a PS/graphene interface. They found that at low concentrations of phenyl groups, these groups tended to lie parallel to the substrate plane. In contrast, at higher concentrations, steric restrictions caused the phenyl groups to adopt an upright orientation. Similarly, Opdahl et al.[3] studied the surface conformation of poly(ethylene-co-propylene) rubber copolymers with varying concentrations of methyl groups per chain. Their results showed that at high methyl group concentrations, steric hindrance from adjacent groups led to random orientations or orientations directed towards the bulk. On the other hand, at low methyl group concentrations, the methyl groups segregated and oriented themselves at the film surface, demonstrating the critical role steric effects play in determining interfacial chain behavior.

The surface energy of the substrate, along with the type and strength of the polymer-substrate interactions, plays a critical role in determining the interfacial conformation of polymer chains. Wilson et al.[11] demonstrated that altering the substrate surface energy induces significant changes in the interfacial orientation of PS chains. They observed that near a hydrophobic substrate, the orientation of the phenyl groups was similar to that at the air interface. On the other hand, on a hydrophilic substrate containing OH surface groups, the phenyl groups of PS tilted toward the substrate to form H-π-interactions. This reorientation resulted in significantly improved adhesion of PS films to the hydrophilic substrate compared to the hydrophobic one, highlighting the critical influence of chain conformation on film performance. Additionally, factors such as the inclusion of fillers or foreign bodies, such as nanoparticles, have also been reported to profoundly affect the interfacial conformation of polymer chains, further emphasizing the complexity of interfacial behavior[108].

2.6. Sum frequency generation (SFG) spectroscopy

Sum-frequency generation spectroscopy is a second-order nonlinear vibrational spectroscopy technique used to investigate molecular structures at interfaces. A detailed theoretical background of SFG spectroscopy, as well as the methodologies for spectra analysis are provided in section 3.4 of Chapter 3. In summary, SFG spectroscopy involves probing interfacial molecular chains using a tunable infrared beam (ω_{IR}) and a high-intensity visible beam (ω_{VIS}). The resulting SFG signal arises from the interaction of these beams with the interfacial chains and has a frequency equal to the sum of their frequencies ($\omega_{SFG} = \omega_{IR} + \omega_{VIS}$)[14].

2.6.1. Comparing SFG spectroscopy with other interfacial analytical methods

Given the critical role of interfacial molecular conformation in governing numerous processes in polymer science, the ability to directly probe these conformations using non-destructive techniques is of great importance. For a method to be fully suitable for such analyses, it must exhibit high selectivity towards interfacial chains at the nanoscale (~1 nm) and be capable of probing both free and buried interfaces effectively. SFG spectroscopy fulfills these criteria, serving as a highly powerful tool for such investigations by providing detailed compositional and orientational insights into molecular arrangements at interfaces.

SFG spectroscopy can be utilized independently or in combination with other powerful analytical techniques to study interfaces. For instance, AFM offers valuable insights into surface topography, making it particularly effective for analyzing crystalline and semi-crystalline interfaces or for investigating dewetting phenomena[50,93,95]. However, AFM lacks the ability to provide direct compositional or molecular-level net orientational information and is restricted to examining free interfaces. Another important analytical technique for interfacial analysis is x-ray reflectivity (XRR), which is well-suited for probing both free and buried interfaces, delivering critical data on electron density variations, thickness, and interfacial roughness[109]. However, XRR does not offer the chemical specificity or molecular orientation details that SFG spectroscopy uniquely provides.

Neutron reflectivity is a highly advanced technique for interfacial analysis, standing out for its ability to deliver precise depth profiles and detailed structural information, including insights into buried interfaces. However, the method often necessitates isotopic labeling of samples, which can potentially alter the behavior of the labeled samples compared to their unlabeled counterparts[110]. Secondary ion mass spectroscopy (SIMS), on the other hand, offers chemical and isotopic composition of interfaces with high sensitivity. However, it is a destructive method and lacks the orientational information of SFG.

In this context, SFG spectroscopy stands out as an exceptional analytical tool for probing the interfacial conformations of polymer chains. Its non-destructive nature, combined with its ability to provide molecular-level insights into both compositional and orientational aspects, makes it uniquely suited for studying the nanoscale structure of free and buried interfaces.

2.6.2. Key features of SFG spectroscopy

The distinct interface specificity of SFG spectroscopy arises from its intrinsic selection rules, rather than limited penetration depth, as seen in other techniques. Even though the laser beams can interact with the bulk material, the SFG signal originates exclusively from the interfacial groups. This is because the selection rules for SFG state that centrosymmetric environments are not SFG-active. In most polymeric materials, the bulk is centrosymmetric and therefore does not produce an SFG signal. However, at interfaces, the centrosymmetry is disrupted, enabling the generation of an SFG signal (Figure 2.10).

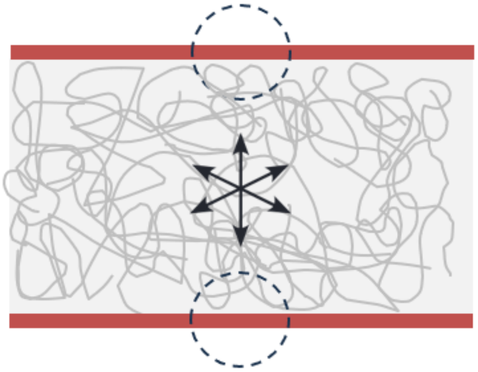

Figure 2.10. Schematic representation of polymer chains within a thin film. In the bulk, the polymer chains adopt a random coil conformation with chain entanglements, creating a centrosymmetric environment that is not SFG-active. At the interfaces, illustrated by the dotted circles, the centrosymmetry is disrupted, allowing these regions to generate an SFG signal.

An SFG spectrum contains the vibrational resonances of interfacial molecules, providing valuable compositional insights specific to the interface. However, it is important to highlight some differences between SFG spectra and conventional attenuated total reflectance Fourier transform infrared (ATR-FTIR) spectra:

- ATR-FTIR spectra includes the vibrational responses of both bulk and interfacial molecular chains. As a result, the contribution from interfacial chains is often negligible in the overall spectrum. On the other hand, the SFG spectra possesses high selectivity for the interfacial chains, with negligible contribution from the bulk.
- The intensity of ATR-FTIR spectra is unaffected by the molecular orientation or the degree of molecular ordering. In contrast, these factors significantly influence the intensity of SFG spectra, making it sensitive to the structural arrangement at the interface (Figure 2.11).

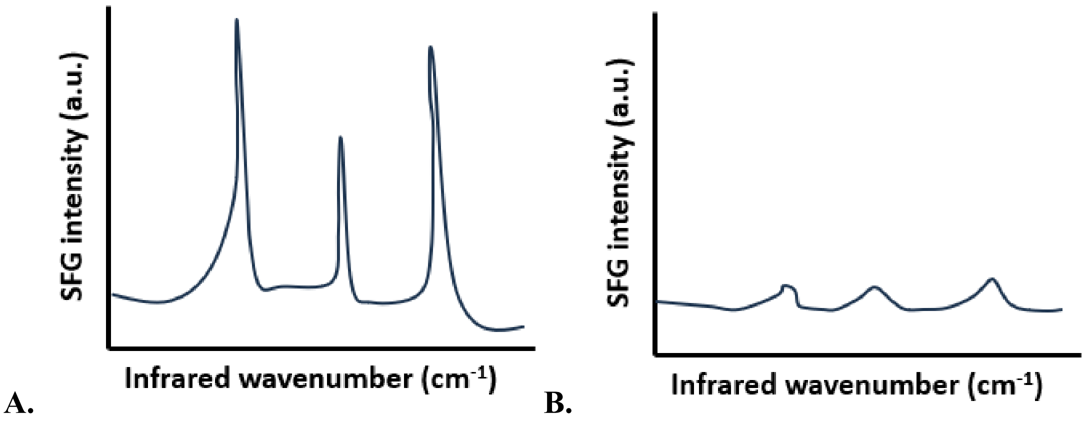

Figure 2.11. SFG spectra showing the vibrational resonances of interfacial molecules. A. Highly ordered interface; and B. Disordered interface. Adapted from[14].

The sensitivity of SFG spectra to interfacial molecular ordering has been extensively utilized to study the relaxation dynamics of interfacial chains, particularly in systems where relaxation results in the randomization of interfacial groups[10,102]. In such cases, a clear reduction in SFG intensity is observed over time during annealing, reflecting the progressive relaxation of the molecules.

In SFG spectroscopy, each beam is polarized, and its polarization is described using three consecutive letters representing the states of the SFG, visible, and infrared beams, respectively.

The polarization state refers to the orientation of the electric field's oscillation relative to the plane of incidence. For instance, s-polarized light has an electric field oscillating perpendicular to the plane of incidence, parallel to the surface. On the other hand, p-polarized light has an electric field oscillating within the plane of incidence, which includes components both perpendicular to the surface and parallel to it[14].

The two most common polarization combinations in SFG are ssp and ppp. These combinations are sufficient to extract orientational information about molecular groups at an interface. In the ssp polarization configuration, the intensity of the vibrational resonances is directly related to the z-component of the vibrational dipole. This enables a rapid qualitative analysis of SFG ssp spectra, where the resonance intensity provides insights into the orientation of specific molecular groups at the interface. Furthermore, the relative amplitudes of vibrational modes in ssp and ppp polarizations provide quantitative information about the angular orientation of molecular groups, as discussed in detail in Chapters 3 and 5.

2.6.3. Directly probing buried interfaces using SFG spectroscopy

SFG spectroscopy is particularly valuable for studying buried interfaces, such as polymer-substrate or solid-liquid boundaries. However, the successful analysis of these buried interfaces necessitates meticulous experimental strategies to overcome inherent challenges. One critical requirement is the precise control of sample geometry and refractive indices to achieve phase-matching conditions, which is essential for filtering out signals originating from other interfaces present in the film. This is particularly important for systems with multiple interfaces, as each can contribute to overlapping signals, complicating the isolation of the desired buried interface information.

A major limitation in the analysis of buried interfaces is the attenuation of the SFG signal. This attenuation arises from scattering and absorption by overlaying materials, especially in systems with thick or optically dense layers, which reduce the effective signal strength from the buried interface. Furthermore, interpreting SFG spectra is challenging due to the presence of substrate effects, background noise, and contributions from other interfacial regions. These overlapping signals often obscure the buried interface-specific vibrational modes, making spectral deconvolution and interpretation more complex.

For thin polymeric films containing a free surface, the SFG signal at the polymer/substrate interface is generally reported to be significantly weaker (around an order of magnitude smaller) than the signal observed at the polymer/air interface[8]. To address this, researchers have developed innovative experimental strategies aimed at minimizing contributions from the polymer/air interface to better isolate the buried interface signal[111]. For instance, optimizing sample geometry, such as adjusting the incidence angle or film thickness using thin-film interference models [8,19], can enhance the sensitivity to the buried interface. Additionally, sandwiched configurations, where the polymer is enclosed between two substrates, have been employed to eliminate the influence of the polymer/air interface.

In systems involving metallic substrates, researchers have exploited the unique optical properties of metals to improve the analysis of buried interfaces. For example, Lu and co-workers [7,112] demonstrated that the strong non-resonant response of metals and the resulting plasmonic field at the polymer/metal interface could be leveraged to enhance the buried interface signal. This approach enables selective probing of polymer conformations near metals, providing direct and precise measurements of the interfacial molecular structure. Such innovations, combined with advanced data analysis techniques and complementary methods, continue to push the boundaries of SFG spectroscopy for studying buried interfaces, paving the way for a deeper understanding of these critical interfacial systems.

Chapter 3 . Influence of polymer molecular weight on chain conformation at the polystyrene/silver Interface

3.1. Preface

This chapter was previously published as: https://doi.org/10.1021/acs.langmuir.1c01211

"Influence of polymer molecular weight on chain conformation at the polystyrene/silver interface" Bianca Martins de Lima, Patrick Hayes, and Paula Wood-Adams, (2021). *Langmuir*, 37(33), 10036–10045.

In this study, we investigated the effect of polystyrene molecular weight on chain conformation near a strongly interacting silver substrate, providing valuable insights on the relationship between chain length and interfacial conformation near metallic substrates. The use of SFG spectroscopy to study metallic interfaces is particularly advantageous due to the signal amplification generated by plasmon field formation at the polymer/metal interface, enabling direct and precise measurements of these buried interactions.

We utilized atactic polystyrene samples with molecular weights ranging from 20,000 g/mol to 400,000 g/mol and observed a strong correlation between molecular weight and interfacial chain conformation. High-molecular-weight polystyrene exhibited a greater number of interactions between the polymer backbone and the substrate, achieved through the tilting of pendant phenyl groups toward the surface normal. In contrast, low-molecular-weight polystyrene adopted a more isotropic backbone conformation near the substrate, with fewer polymer/substrate interactions and phenyl groups tilting toward the substrate plane.

These distinct conformations arise from the balance between entropy and enthalpy during polymer adsorption, which is strongly influenced by chain length. Additional factors, such as variations in polymer free volume and the relative abundance of chain ends, further contribute to the observed differences in interfacial behavior.

Minor adjustments, including the numbering of figures, tables, and references, were made to ensure consistency with the rest of the thesis. Since the following manuscript is presented in its entirety, there may be some overlap with other sections of the thesis, such as repeated descriptions of abbreviations and equations.

3.2. Abstract

The dependence between the conformation of polystyrene (PS) and its molecular weight (Mw) in the vicinity of a metal interface was investigated by sum frequency generation (SFG) spectroscopy. Tilt angles $\theta \geq 50°$ (the angle between the C_2 axis of the pendant phenyl ring and the surface normal) were observed for all samples, due to the interaction between the aromatic rings and the metal surface. Furthermore, it was found that θ decreases with increasing Mw for PS samples ranging from 20 x10^3 g/mol to 400 x10^3 g/mol. The intensity of the backbone SFG signal was higher for high Mw PS, compared to low Mw PS, indicating a greater number of backbone interactions with the silver substrate surface for the high Mw sample. These structural differences are driven by different entropic and enthalpic contributions to the free energy of adsorption for different polymer Mw. Differences in the polymer free volume and in the relative amount of chain ends with higher mobility may also influence the chain conformation. These results suggest that important interfacial properties of polymeric thin films, such as adhesion and wettability, could be tailored by modifying the polymer Mw to achieve the desired interfacial conformation.

3.3. Introduction

Polymer/solid interfaces regulate many critical processes and properties such as adsorption[41], adhesion[11,113], wall-slip[47], and wettability[19]. For example, in the aerospace industry, polymer coatings are applied to metallic substrates to improve their corrosion resistance[114], while in biomedical applications they can be applied to implants to reduce their failure rate[115]. In these applications, a strong adhesion between the different layers of materials (substrate/polymer coating/top layer (if any)) is essential to ensure the long-term properties[114,115]. Furthermore, the adsorption of polymers on the surface of particles has been used in environmental applications[116], as well to improve the stability of colloidal systems[117].

The importance of polymer/substrate interfaces is even more pronounced in polymeric thin films, in which there is a large contribution of the interfacial chains in the total film volume and therefore in the overall film properties. For example, Li et al.[4] have shown a significant increase in the glass transition temperature (T_g) of poly(methyl methacrylate) (PMMA) thin films confined between two solid surfaces with decreasing the film thickness, due to the larger contribution of the chains near the solid interface, which have slower relaxation dynamics than the bulk chains. Furthermore, Hong et al.[118] have recently demonstrated that the T_g of PS thin films can be modified by anchoring different aromatic compounds on the substrate, which leads to different conformations of the PS chains due to π-π interactions between the polymer and the substrate.

The molecular ordering of the chains in the vicinity of a substrate is governed by the type and intensity of the interaction between the polymer/substrate pair. Generally, substrates that have high surface energy and the possibility of having a strong chemical interaction with the polymer (eg. H-π, π-π and d-π interactions) are considered highly interactive substrates. On the other hand, weakly interactive substrates usually present low surface energy combined with the absence of such strong chemical interactions. Wilson et al.[11] revealed different conformations of PS chains in the vicinity of surface-modified glass of varying hydrophilicity, as a result of π-H bonding between the polymer and the substrate. Similarly, the conformation of the deuterated polystyrene (*d*-PS) phenyl rings at the liquid/*d*-PS interface can be modified by changing the surface tension of the liquid[119], or by the presence of biological molecules that can adsorb on the polymer interface[120]. Furthermore, while prior research evidences the randomization of the PS phenyl rings near a weakly interactive quartz substrate[10,107], these phenyl groups form an organized structure near highly interactive surfaces such as graphene[6] and silver[7]. The final conformation near a substrate is a balance between the forces acting on different functional groups within the polymer backbone[121] and side groups, as well as entropic and enthalpic factors[107] that govern the polymer adsorption. These findings are promising for allowing the tailoring of interfacial properties and processes via controlling the polymer/substrate interactions.

The Mw of polymeric materials influences the microstructure and dynamics of interfacial chains, especially due to changes in the free volume[122], number of entanglements, and entropic and enthalpic effects[51,123] during polymer adsorption. Li et al.[64] demonstrated the key role of Mw in the adsorption dynamics of PS chains on sapphire and they determined the Mw effect on the chain fraction forming the irreversibly adsorbed layer at equilibrium. Recently, our research group investigated the effect of the PS Mw on the polymer conformation at the PS/air interface. Our findings highlighted the correlation between the phenyl ring orientation and the PS Mw, due to changes in the polymer free volume[5]. However, there is a lack of studies analyzing how Mw influences the phenyl ring orientation in the vicinity of highly interactive substrates, such as metals.

SFG spectroscopy stands out as a powerful technique to study molecular conformations at buried interfaces[111], since it has high interface-specificity for probing the few atomic layers comprising the interface. In the SFG experiment, a high-intensity visible laser beam (ω_{vis}) and a tunable IR laser beam (ω_{IR}) are spatially and temporally overlapped at the interface, generating the SFG signal (ω_{SFG}) at a frequency that corresponds to the sum of the incident beam frequencies ($\omega_{SFG} = \omega_{vis} + \omega_{IR}$)[14]. The selection rules of SFG forbid its generation in centrosymmetric regions, such as the bulk region of most materials, and SFG becomes therefore exclusive to the interfacial region, where centrosymmetry is broken.

This study addresses the correlation between the Mw of PS chains and the conformation assumed by the chains in the vicinity of a highly interactive silver surface studied by SFG spectroscopy. The motivation for this study relies on the fact that polymer/metal interfaces are present in several applications, such as in polymer molding[124,125] in electronics[126], and in space applications[127]. More specifically, we have decided to study the polymer/silver interface because this interface has been previously studied[7,112], and this would facilitate the interpretation of the results. Polymer/silver interfaces occur in several applications, for example, polymer coatings can be applied on silver substrates for surface plasmon applications[128] and their application on silver mirrors has been proposed to improve the performance of cooling systems in order to reduce electricity consumption[129]. Furthermore, silver coatings can be applied to polymer substrates to create a reflective and conductive surface[130] or to add extra functionalities to polymer particles[131], such as antimicrobial properties in biomedical applications. Lastly, polymer/silver interfaces are also of great importance in the final properties of polymer/silver nanocomposites[132–134].

In the vicinity of the PS/Ag interface, we hypothesized that the possibility of occurrence of chemisorption of the pendant phenyl rings, combined with the changes in the free volume and entropic and enthalpic contributions result in different conformations with changing Mw. Here, we report the SFG spectra of the PS/Ag interface of monodisperse PS samples of Mw ranging from 20 x 10^3 g/mol to 400 x 10^3 g/mol in the region of the backbone and phenyl ring C-H stretch vibrational frequencies. The spectral changes are analyzed to determine the tilt angle variation of the pendant phenyl ring with Mw. Furthermore, the drivers for different conformations are discussed in terms of free volume and the enthalpy/entropy balance. To the best of our knowledge, this is the first time a correlation between the PS pendant phenyl ring tilt angle and the polymer molecular weight is reported for a PS/metal interface. This expands the understanding of polymer molecular structures near metallic substrates, in which the possibility of the occurrence of chemisorption may greatly affect the final chain conformation.

3.4. Experimental section

3.4.1. Materials

Monodisperse atactic polystyrene was obtained from Scientific Polymer Products Inc. and used as received, without further purification. The nominal molecular weight, the number-average molecular weight (Mn), and the polydispersity index (PDI) of the PS used in this study are summarized in Table 3.1, as reported by the supplier.

Table 3.1 Molecular weight and PDI of PS samples.

Nominal molecular weight (x 10^3 g/mol)	Mn (g/mol)	PDI (Mw/Mn)
20	19,500	1.01
200	177,800	1.03
400	424,900	1.06

3.4.2. Sample preparation

Fused silica IR grade windows (ISP Optics Corp.) were used as substrates for film deposition. The windows were cleaned by immersion into hot piranha solution for 1 hour (80°C, 3:1 H_2SO_4/30 vol % H_2O_2), followed by multiple rinsing cycles with water (HPLC grade, Sigma Aldrich) until neutral pH was achieved (measured at the edge of the windows using pH test strips). Then, the substrates were blow dried and placed in a vacuum oven at 120°C for 1 hour, for further drying. The dry substrates were held under vacuum to cool down to ambient temperature.

Thin films with thickness of around 100 nm were produced by spin coating PS solutions in toluene on the windows. The spin coating was performed at 2000 rpm for 1 min. The same thickness was achieved for the different Mw by adjusting the solution concentration (1% - 2% PS). For measuring the films' thicknesses, thin films were spin-coated on glass slides using the same conditions as the SFG samples (solution concentration and spin coating parameters) and a scratch was gently made in the films to produce a region without polymer. Then, the thicknesses of the films were analyzed using a profiler (DEKTAK 150). The films were annealed at 150°C (bulk T_g ≈105°C) under vacuum for 4 hours and cooled down to ambient temperature under vacuum.

The PS surface was then coated with a 500 nm layer of silver by electron-beam evaporation (2-3 angstroms/s, 6 x 10^{-8} torr), according to the method previously reported by Lu et al.[7] to produce a sandwiched configuration of fused silica/PS film/Ag. It is important to note that the sample was kept at 25°C during the silver layer deposition to avoid the possibility of thermal degradation. Furthermore, the energy of the arriving particles during deposition is low, so that they may not cause any breakage of the polymer chains. Even though analyzing the polymer after the metal coating for signs of degradation is challenging because the polymer film is sandwiched between the silica window and the silver layer, there are evidences regarding the absence of degradation: 1. the SFG spectra, that contain the resonances expected for PS and are comparable with the literature, 2. the visual and mechanical integrity of the film (transparent film, no darkness, no signs of dewetting or significant surface irregularities), 3. The consistency of the spectra acquired comparing different spots in a single sample, as well as multiple samples. The coated samples were subjected to a second annealing at 150°C under vacuum for 4 hours and cooled down to ambient temperature under vacuum. The SFG spectra were collected from the samples, with the incident beams entering the sample through the silica window and being reflected at the polymer/silver interface. A scheme of the experimental methodology is presented in Figure 3.1. The samples of different Mw were prepared on the same day and annealed together, to minimize any differences between the samples other than the Mw of polystyrene.

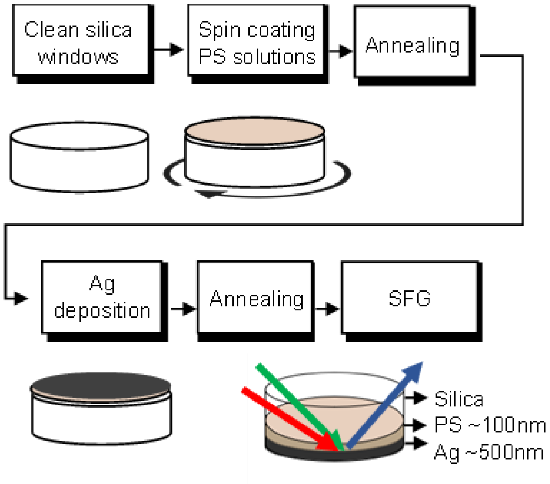

Figure 3.1. Experimental steps to produce the silica/PS/Ag sandwiched samples

3.4.3. SFG measurements

The details of our scanning SFG system (EKSPLA) are provided elsewhere[5,135]. Briefly, the system comprises a PL2241 series laser, with an optical parametric generator (OPG) PG501/DFG and a monochromator MS2001. The laser generates a fundamental 1064 nm beam and a second harmonic 532 nm beam (visible beam) that pumps the OPG to generate the tunable IR beam. The IR scanning frequencies targeted the C-H stretch region of the polymer backbone and phenyl ring, ranging from 2750 to 3100 cm^{-1}. The visible and infrared beams incidence angles are 60° and 55°, respectively, with respect to the surface normal. The pulse energy of the visible beam was adjusted to 10 μJ to avoid damaging the silver layer. The spectra were collected in ssp and ppp polarization combinations, where the letters represent the polarization of the SFG, visible, and IR beams, respectively.

The spectra were normalized by dividing the SFG signal by the product of the visible and IR energies[5]. A sample of PMMA that exhibits an intense SFG peak at 2955 cm^{-1} was used to calibrate the frequencies in the PS spectra. Two specimens per molecular weight were analyzed and for each specimen, at least 6 ssp and 6 ppp spectra were collected at 6 different spots. At least 2 ssp and 2 ppp spectra for each Mw were acquired in a single day. The spectra collected on the same day were averaged and fitted using Igor Pro 8 software (WaveMetrics). The fitting parameters for the average daily ssp or ppp spectra were then averaged for all days. The details regarding the calculation of the uncertainties are provided in section A1 of Appendix A.

3.5. Theoretical background

3.5.1. Sum frequency generation spectroscopy

The SFG field arises from the second-order nonlinear component of the induced polarization $\boldsymbol{P}_{SFG}^{(2)}$, as shown in Equation 3.1[14].

$$\boldsymbol{E}_{SFG} \propto \boldsymbol{P}_{SFG}^{(2)} = \varepsilon_0 \chi^{(2)} \boldsymbol{E}_{VIS} \boldsymbol{E}_{IR} \qquad \text{Equation 3.1}$$

Where $\boldsymbol{E}_{SFG}$, $\boldsymbol{E}_{IR}$, and $\boldsymbol{E}_{VIS}$ are the SFG, IR, and visible electric fields, ε_0 is the vacuum permittivity and $\chi^{(2)}$ is the second-order nonlinear susceptibility tensor. The tensor $\chi^{(2)}$ is the macroscopic average of the first-order molecular hyperpolarizability β, which relates the nonlinear response of the molecule to the incident and emitted fields. Considering a molecular fixed coordinate system (a,b,c), the relationship between $\chi^{(2)}$ and β can be described by Equation 3.2[5].

$$\chi_{ijk}^{(2)} = \frac{N}{\varepsilon_0}\sum_{lmn}\langle R_{il}(\theta,\psi,\phi)R_{jm}(\theta,\psi,\phi)R_{kn}(\theta,\psi,\phi)\beta_{lmn}\rangle \qquad \text{Equation 3.2}$$

Here, N is the number of molecules per unit area and the Euler angles θ, ψ, ϕ, describe the relationship between the molecular fixed axes and the surface fixed axes (Figure 3.2). The product of the rotational matrices using the three Euler angles, $R_{il}(\theta,\psi,\phi)R_{jm}(\theta,\psi,\phi)R_{kn}(\theta,\psi,\phi)$, is present to convert from the molecular coordinate system (a,b,c) to a surface fixed coordinate system (x,y,z). The brackets indicate orientational average and the indices l, m, and n are generic indices taking values of a, b, or c.

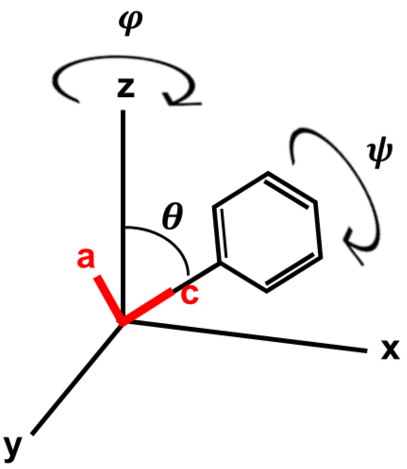

Figure 3.2. Scheme of surface fixed axis (x,y,z), molecular coordinate system (a,b,c), and Euler angles (θ, ψ, ϕ) where the interface is in the x-y plane. Note that the b axis was omitted from the drawing because it is perpendicular to the page.

A simplified expression for β is often used in SFG spectroscopy experiments, where ω_{IR} is near a vibrational energy level, and ω_{Vis} is typically far from the energy level of an electronic transition[5,14].

$$\beta_{lmn} = \frac{1}{2\hbar}\frac{M_{lm}A_n}{\omega_q - \omega_{IR} - i\Gamma_q} \qquad \text{Equation 3.3}$$

Here, ω_q is the frequency of the resonant vibrational mode q, and Γ_q is a damping constant. Additionally, M_{lm} and A_n are the Raman polarizability and IR transition dipole moments, respectively. To be SFG active, a vibrational mode must be both Raman and IR active. Furthermore, when the frequency of the IR beam (ω_{IR}) approaches the frequency of the vibrational mode ω_q the term $\omega_q - \omega_{IR}$ approaches zero, and the magnitude of β (and consequently $\chi^{(2)}$) increases significantly and the SFG signal is resonantly enhanced[8,14,136]. The SFG intensity (I_{SFG}) can be fitted using a Lorentzian function, according to Equation 3.4 [14,111,137]. In Equation 3.4, χ_{eff} is the effective second-order nonlinear susceptibility tensor at the interface, which has contributions from the resonant vibrational modes and from the nonresonant background. Additionally, A_q is the amplitude of the vibrational mode q, χ_{NR} and α are the non-resonant contributions from the Ag interface and the phase of the non-resonant signal, respectively.

$$I_{SFG} \propto \left|\chi_{eff}\right|^2 = \left|\chi_{NR}e^{i\alpha} + \sum_q \frac{A_q}{\omega_{IR} - \omega_q + i\Gamma_q}\right|^2 \qquad \text{Equation 3.4}$$

3.5.2. SFG on metallic substrates

SFG near metallic interfaces has some peculiarities compared to SFG for molecules deposited on dielectric materials. The high value of χ_{NR}, due to the generation of a plasmon field, leads to a significant enhancement in the overall SFG signal. For an azimuthally isotropic interface with a dielectric material, the non-vanishing elements of $\chi^{(2)}$ are $\chi^{(2)}_{yyz}$ in ssp polarization and $\chi^{(2)}_{xxz}$, $\chi^{(2)}_{zzz}$, $\chi^{(2)}_{zxx}$, $\chi^{(2)}_{xzx}$ in ppp polarization[14]. At a metal interface, the only elements that have a significant contribution to the SFG spectrum are those with a z IR component, $\chi^{(2)}_{yyz}$ in ssp and $\chi^{(2)}_{xxz}$, $\chi^{(2)}_{zzz}$ in ppp polarization, due to the high reflectivity of metals in the infrared region

The infrared spectrum of molecules near metals is highly sensitive to the molecular orientation. The relative intensity of the IR absorption of molecules near metals is proportional to the projection of the vibrational IR transition dipole moment in the direction of the surface normal[138,139]. In other words, for molecules analyzed by SFG with the IR beam in p polarization, the IR absorption response would be maximized when the direction of the dipole change of the vibrational mode coincides with the surface normal and it would be minimized when the IR transition dipole moment variation is parallel to the surface.

The intense plasmon field generated at the polymer/metal interface enables the use of the sandwiched sample configuration (silica/PS/Ag) to analyze the conformation of the PS chains in the vicinity of the PS/Ag interface using SFG. The intensity of the plasmon field is maximized at the Ag/PS interface and decays exponentially in the direction normal to the silver surface. The decay in the plasmon field intensity as a function of the distance from the silver surface for the sample used in this study was estimated following the approach published by Read and co-workers[140]. The result is presented in Figure A1 and discussed in section A2 of Appendix A. The plasmon field intensity will be 5 times lower at the PS/silica interface, which makes the contribution of this interface negligible in the SFG spectrum. Lu and co-workers have demonstrated experimentally that in this sandwiched configuration, the SFG signal is generated predominantly at the polymer/Ag interface[7,112].

3.5.3. Tilt angle calculation

The three Euler angles, namely the tilt (θ), the twist (ψ) and the azimuthal (φ) angles describe the orientation of the pendant phenyl ring with respect to the surface fixed coordinate system (Figure 3.2). In the orientation analysis, we consider the twist and azimuthal angles as isotropically distributed. We believe that this assumption is reasonable since the samples were annealed above T_g, removing any net orientation of the phenyl rings in the plane of the surface (x-y plane), leading to isotropic φ distribution, and since the phenyl ring is considered to have free rotation around the C_2 axis, leading to isotropic ψ distribution[5,8,111]. The spectral differences observed for the different Mw are therefore attributed to changes in θ, however, we acknowledge that the real interface might have a more complex structuring that is not fully captured by just a change in the tilt angle.

The five different C-H stretch vibrational modes of the phenyl ring are illustrated in Figure 3.3. The ratio between ν_2 amplitudes in ssp and ppp polarizations can also be used to calculate the average value of θ, as described in Equation 3.5, where F_{ssp} and F_{ppp} are the Fresnel factors for the PS/Ag interface and the brackets represent an ensemble average. The derivation of Equation 3.5, as well as the calculation of the Fresnel factors for the PS/Ag interface, were reported by Lu et al.[7] and are used as reported in this study.

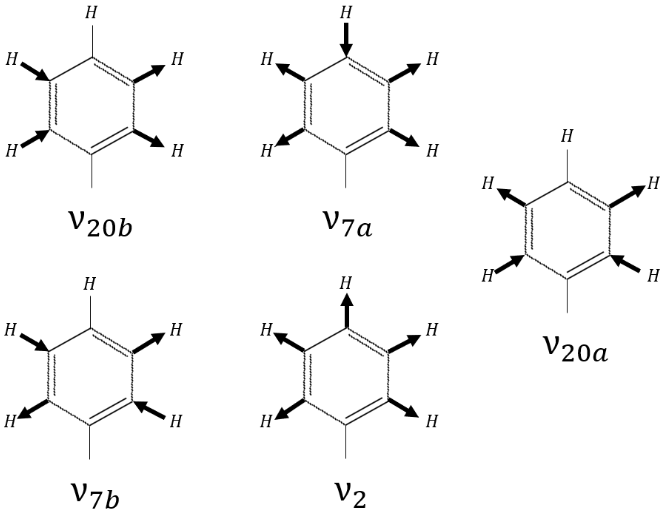

Figure 3.3. C-H stretching vibrational modes for a phenyl ring.

$$\frac{\chi^{(2)}_{eff,ssp,v2}}{\chi^{(2)}_{eff,ppp,v2}} \cong \frac{F_{ssp,yyz}\chi_{yyz,v2}}{F_{ppp,xxz}\chi_{xxz,v2}+F_{ppp,zzz}\chi_{zzz,v2}} \cong \frac{0.26\langle cos\,\theta\rangle-0.08\langle cos^3\theta\rangle}{0.63\langle cos\,\theta\rangle+0.08\langle cos^3\theta\rangle} \qquad \text{Equation 3.5}$$

A second approach for the tilt angle calculation uses the ratio between the amplitudes of the ν_{20b} and ν_2 vibrational modes in ssp polarization, as expressed in Equation 3.6[10,13,141]. This relation can be used to obtain the θ distribution if the values of the hyperpolarizabilities are known[5,6], or it can be used in a qualitative analysis[142] otherwise. The applicability of this approach to SFG spectra on metal surfaces is discussed in section A3 of Appendix A. Qualitatively, Equation 3.6 shows that the intensity of the ν_{20b} vibrational mode will increase with respect to that of the ν_2 mode, as the tilt angle increases (Figure A2)[8].

$$\left|\frac{A_{\nu20b,ssp}}{A_{\nu2,ssp}}\right| = \left|\left(\frac{\beta_{caa,\nu20b}}{\beta_{aac,\nu2}}\right)\left(\frac{2(\langle cos\,3\theta\rangle-\langle cos\,\theta\rangle)}{(7+2r)\langle cos\,\theta\rangle+(1-2r)\langle cos\,3\theta\rangle}\right)\right| = R \qquad \text{Equation 3.6}$$

Above, $A_{\nu20b}$ and $A_{\nu2}$ represent the amplitudes of ν_{20b} and ν_2 vibrational modes, respectively. Additionally, $\beta_{caa,\nu20b}$ and $\beta_{aac,\nu2}$ are the first-order molecular hyperpolarizability tensor components for ν_{20b} and ν_2 modes, respectively, and r is defined as the ratio between β_{ccc}/β_{aac} for the ν_2 mode.

3.6. Results and discussion

3.6.1. Tilt angle analysis

The average SFG spectra of the PS/Ag interface for PS samples ranging from 20 x10^3 g/mol to 400 x10^3 g/mol in ssp and ppp polarization are shown in

Figure 3.4. The SFG spectra present C-H vibrational modes of the polymer backbone (2800-3000 cm^{-1}) and of the phenyl ring (3000-3100 cm^{-1}). Previous studies have observed backbone vibrational modes at ~2850 cm^{-1}, ~2875 cm^{-1}, ~2905 cm^{-1}, ~2935 cm^{-1}, and ~2960 cm^{-1} and assigned these modes to the CH_2 ss, CH_3 ss, CH, CH_2 as and CH_3 as, respectively, where ''ss'' and ''as'' represent the symmetric and antisymmetric stretch[10,19,105]. In this current study, most of these vibrational resonances could not be resolved, and therefore the fitting was focused on the phenyl ring region, which has well-defined vibrational resonances. However, it is important to note that there is a significant difference in the intensity of the backbone vibrational modes centered at ~2900 cm^{-1} (CH stretch) between the two extremes of Mw analyzed, with the 400 x 10^3 g/mol presenting the highest intensity in this region. A similar high intensity resonance at ~2900 cm^{-1} was previously observed at the PS/quartz interface after long annealing and it was attributed to a high number of backbone/substrate interactions[107].Out of the 5 vibrational modes of the phenyl ring (Figure 3.3), only the modes ν_{20b}, ν_{7a}, and ν_2 are observed at the PS/Ag interface. These modes appear in ~3022 cm^{-1}, ~3035 cm^{-1} and ~3058 cm^{-1}, respectively[7,8,10,19]. The SFG spectra in the phenyl ring C-H stretch region were fitted using the Lorentzian equation (Equation 3.4) and the fitted spectra are presented in Figure 3.5. The fitting parameters are summarized in Table 3.2.

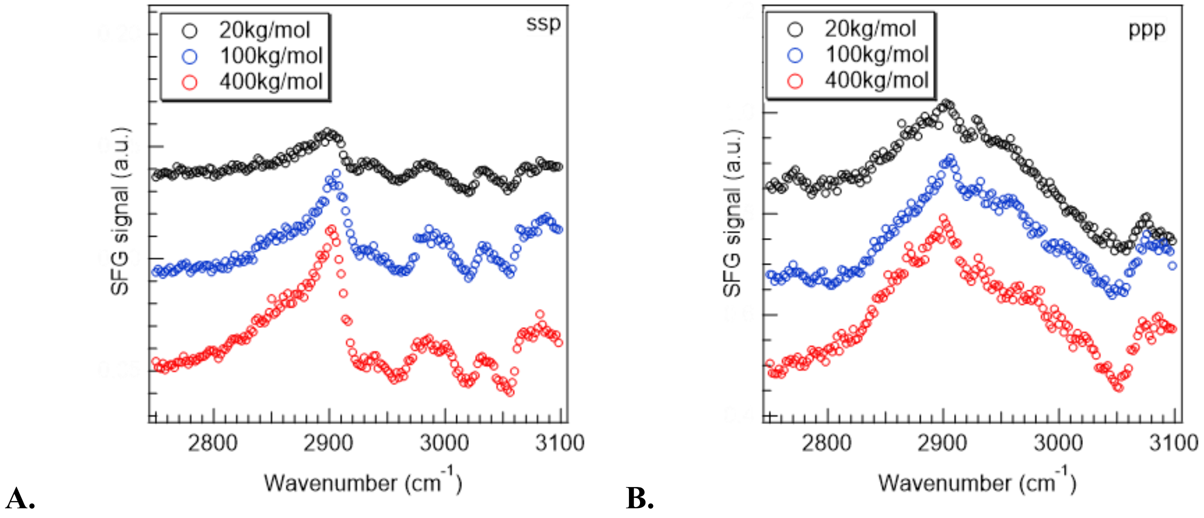

Figure 3.4. SFG spectra for PS samples with a Mw of 20 x 10^3 g/mol (black), 100 x 10^3 g/mol (blue) and 400 x 10^3 g/mol (red). Curves are offset for clarity. A. ssp polarization and B. ppp polarization.

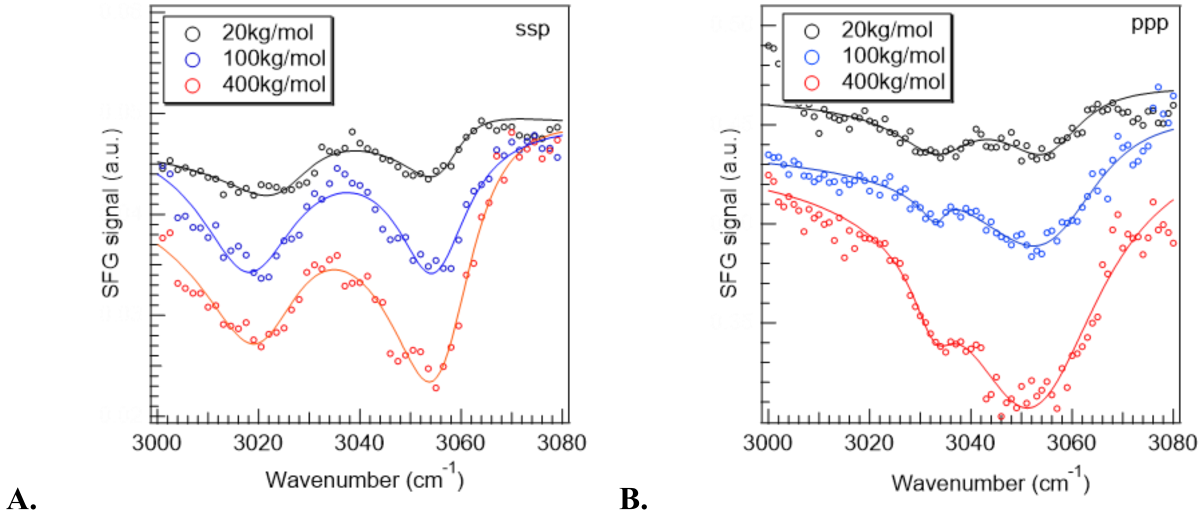

Figure 3.5. SFG spectra in the phenyl ring C-H stretch region for PS samples with a Mw of 20 x 10^3 g/mol (black), 100 x 10^3 g/mol (blue) and 400 x 10^3 g/mol (red). Curves are offset for clarity. Open circles are the average SFG signal and the continuous lines are the fits obtained using Equation 3.4. A. ssp polarization, B. ppp polarization.

Table 3.2. Fitting parameters of the phenyl ring C-H stretch region in ssp and ppp polarization*

	Ssp			ppp			
Mw (x 10^3 g/mol)	20	100	400	20	100	400	Mode
Frequency (cm^{-1})	3020.5±0.7	3021.7±0.5	3023.0±0.4	Absent			ν_{20b}
A_q	0.25±0.03	0.35±0.03	0.35±0.03				
Γ_q (cm^{-1})	12±1	11±1	10±1				
Frequency (cm^{-1})	Absent			3035.5±0.6	3036.9±0.7	3035.5±0.6	ν_{7a}
A_q				0.10±0.04	0.06±0.04	0.08±0.04	
Γ_q (cm^{-1})				5±1	4±2	4±1	
Frequency (cm^{-1})	3057.6±0.4	3058.5±0.3	3058.4±0.3	3056.6±0.7	3058.3±0.8	3058.1±0.6	ν_2
A_q	0.19±0.01	0.31±0.02	0.50±0.02	0.43±0.06	0.81±0.09	1.4±0.2	
Γ_q (cm^{-1})	8.1±0.6	8.5±0.5	9.2±0.4	11±1	15±1	18±1	
χ_{NR}	0.1781±0.0007	0.2068±0.0007	0.2093±0.0008	0.583±0.001	0.624±0.002	0.696±0.003	
α	250±3	252±3	243±2	246±5	226±4	238±3	

*The uncertainties were determined as described in section A1 of Appendix A.

The amplitudes of C-H stretch vibrational modes as a function of the PS Mw are shown in Figure 3.6. The amplitudes of the ν_2 mode increase with increasing Mw in ssp and ppp polarization. The IR transition dipole moment of the ν_2 mode is in the direction of the C_2 axis of the phenyl ring, therefore, an increase in the ν_2 amplitude suggests a decrease in the tilt angle as Mw increases. This mode is a strong IR and Raman mode[13], and this is possibly the reason for its high sensitivity to orientation variations. The ν_2 mode was also reported as the most sensitive mode to Mw changes at the PS/air[5] interface. Compared to the mode ν_2, the modes ν_{20b} and ν_{7a} are weaker in Raman intensity[13], and are less sensitive to the Mw variation. The IR transition dipole moment of the ν_{20b} mode is perpendicular to the phenyl ring C_2 axis and since it is a weak Raman mode, the relatively strong intensity seen in the SFG spectra for this mode implies that the C_2 axis is largely tilted towards the surface[7], which increases the z component of the ν_{20b} IR transition dipole moment.

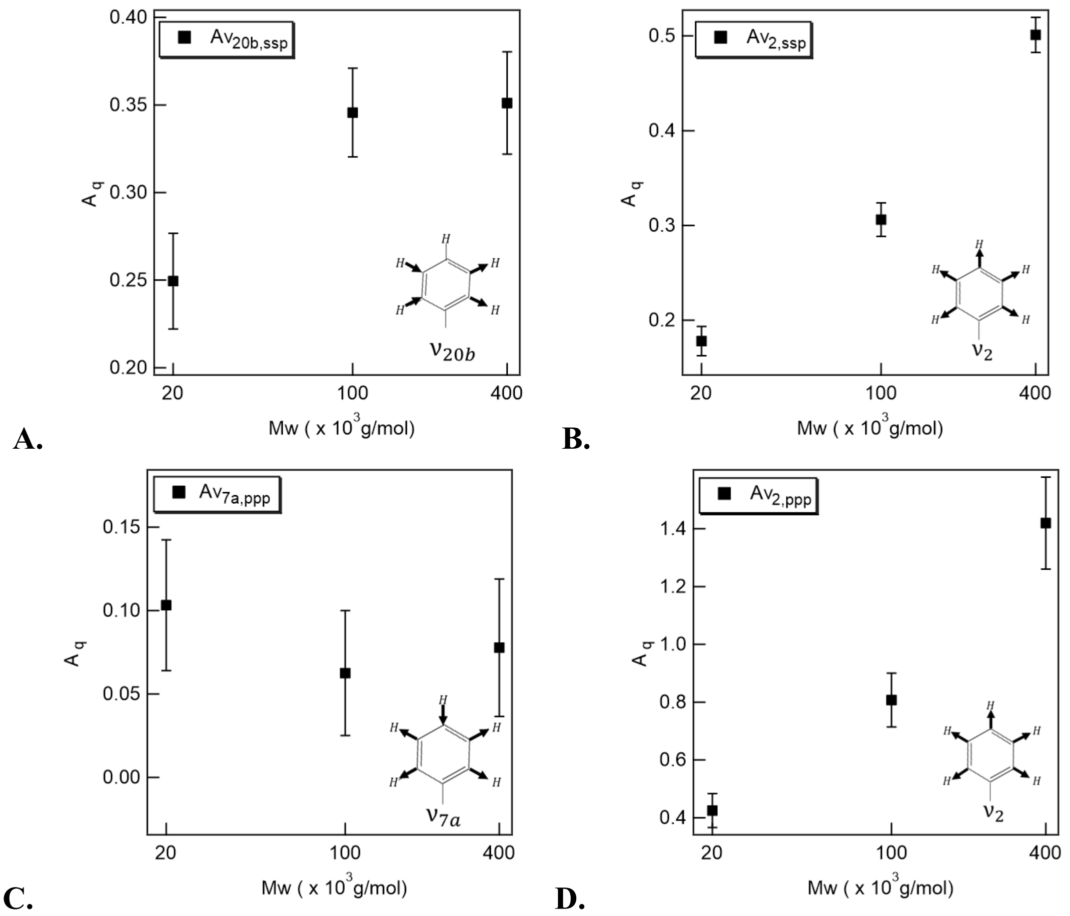

Figure 3.6. Amplitudes of C-H stretch phenyl ring vibrational modes. A. ν_{20b}, ssp; B. ν_2, ssp; C. ν_{7a}, ppp and D. ν_2, ppp. Error bars represent the uncertainties from Table 3.2.

The ratio between the amplitudes of the ν_2 mode in ssp and ppp polarization as a function of Mw is shown in Figure 3.7. The data reveals a trend of decreasing the ssp/ppp ratio as Mw increases. The data in Figure 3.7 is replotted in Figure 3.8 where the grey zones indicate the possible values of θ for each tilt angle distribution width (σ). If the samples are assumed to have a similar σ, this trend would represent a decrease in the tilt angle with increasing the Mw of the PS sample. For instance, for $\sigma = 1°$, the average value of θ would be in the range of 69° to 90°, 54° to 74° and 50° to 62° for PS samples with Mw of 20 x10^3 g/mol, 100 x10^3 g/mol and 400 x10^3 g/mol, respectively. The range of possible values for θ results from the uncertainty in the ν_2 amplitude ssp over ppp ratio, as shown in Figure 3.7. Interestingly, the trend of decreasing tilt angle with increasing Mw resembles the trend observed previously for the PS/air interface[5], even though the physical-chemical drivers for the different conformations are expected to be different for the two interfaces. Lastly, the second method (Figure A3) for tilt angle analysis using Equation 3.6 and the R value (the ratio of the amplitudes of ν_{20b} and ν_2 in ssp polarization) qualitatively corroborates the trend of decreasing the tilt angle as Mw increases.

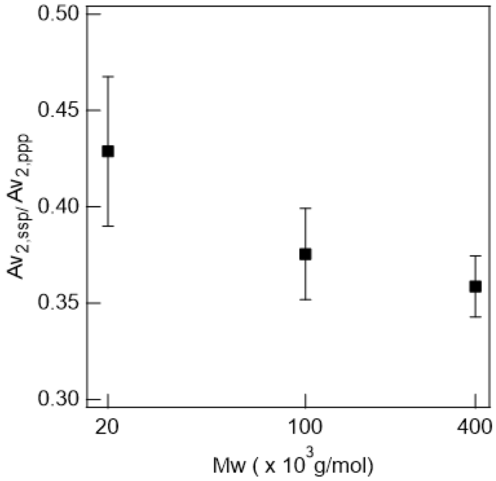

Figure 3.7. Ratio of ssp over ppp amplitudes for the ν_2 vibrational mode. The uncertainties were determined as described in section A1 of Appendix A for the ratio of amplitudes.

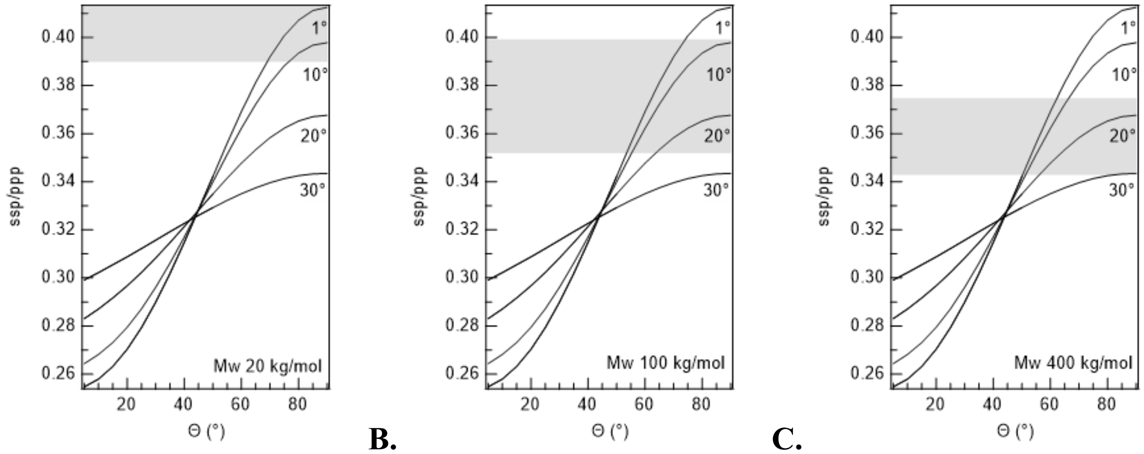

A. **B.** **C.**

Figure 3.8. Tilt angle analysis of the PS pendant phenyl ring using Equation 3.5. Curves show the ssp over ppp ratios for different tilt angles (θ) considering different values of σ (1°, 10°, 20°, and 30°). The grey region represents the experimental ν_2 ssp over ppp ratio and its uncertainty (Figure 3.7). The overlap of the grey region with the back lines represents possible values for θ and σ. A. Mw 20 x10^3 g/mol. B. Mw 100 x10^3 g/mol and C. Mw 400 x10^3 g/mol.

The changes in the two ratios (Figure 3.7 and A3) could also be attributed to changes in the tilt angle distribution width rather than pure changes in the average tilt angle itself. We continue this analysis by focusing on the data in Figure 3.8. The PS with the lowest Mw analyzed (20 x 10^3 g/mol) can only assume a narrow tilt angle distribution (σ <15°) (Figure 3.8 A). On the other hand, as the Mw of the PS increases, wider angle distributions become possible (Figure 3.8 B and C). Therefore, one could argue that the spectral changes show that σ increases (wider distribution, towards randomization) with increasing Mw, rather than changes in the average tilt angle. However, if the trend in the ssp/ppp ratio was due to increasing σ for the samples with higher Mw, one would expect an overall decrease in the amplitude of the SFG vibrational modes with increasing Mw, because the SFG intensity decreases with decreasing ordering of the interface[14], which is the opposite of what is observed. In fact, an increase in the ν_2 vibrational amplitude occurs as Mw increases (Figure 3.6 B and D), and the vibrational resonances are clearly observed in the 400 x 10^3 g/mol spectra, which is not consistent with a wide σ. Therefore, we hypothesize that the changes in the ν_2 ssp/ppp ratio can be mostly attributed to changes in the average tilt angle of the pendant phenyl ring at the PS/Ag interface.

The existence of a net orientation of the phenyl groups at the PS/Ag interface differs from the randomized conformation of the phenyl groups reported for weakly interactive substrates[10,107]. In this sense, the interaction between the substrate and the pendant phenyl ring is critical in driving the organization of this side group. The high values of the tilt angle obtained for all samples analyzed ($\theta \geq 50°$) are expected due to the interactions between the metal and the aromatic ring. The most favorable conformation of C_6 aromatic rings in the vicinity of a silver substrate was proven to be a face-on adsorption[143,144], which would be equivalent to $\theta \approx 90°$. The θ values found in this study are in agreement with previous research in which high values of tilt angle were reported for the PS phenyl ring in the vicinity of highly interactive substrates. For example, Wilson et al.[11] obtained $\theta \sim 50°$ at the interface between PS and modified hydrophilic glass. In their system, the possibility of π-hydrogen bonding between the aromatic rings and the hydroxyl groups at the glass surface favored high tilt angles. Furthermore, $\theta \sim 70°$ was measured at the *d*-PS/water interface in which π-hydrogen bonding is possible[119]. Lastly, our results are comparable with the $\theta > 65°$ reported by Lu et al.[7] at the PS/Ag interface. Note that Lu et al.[7] did not investigate the effect of the PS Mw on the chain conformation and orientation at the PS/Ag interface. Furthermore, both the Mw and the annealing conditions are different than the present study.

3.6.2. Possible physical-chemical factors affecting PS conformation

The adsorption of macromolecules is accompanied by losses in conformational entropy, therefore, the driving force for adsorption is the enthalpic gain of the polymer/substrate interaction. The molecular weight plays an important role in the overall entropy/enthalpy balance, since the higher the Mw, the higher the conformational entropy loss upon adsorption[145], but also the higher the enthalpic gain due to increasing the number of polymer/substrate interactions per chain[123,146,147]. According to de Gennes scaling theory[123], the free energy of adsorption of a single molecule is a function of a dimensionless energy parameter (δ), which is a balance between the attractive enthalpic gain and the entropic loss per monomer adsorbed on a substrate. The value of δ does not depend on Mw since it is related to the adsorption of a single monomer. Bouchaud and Daoud[51] reported a critical value, δ_c, which is a function of the chain length and determines the dominant effects for the adsorption of a single chain. The value of δ_c is proportional to the degree of polymerization, N, to the power of -3/5 ($\delta_c \sim N^{-3/5}$). The higher the value of δ_c compared to δ, the more dominant is the entropic contribution to the free energy of adsorption and the chains in the vicinity of the substrate will tend to assume an isotropic conformation to minimize the entropy loss during adsorption. Similarly, the lower the value of δ_c compared to δ, the more dominant is the enthalpic contribution and the multi-segment adsorption occurs by extension of the polymer chain on the substrate (train-loop-tail configuration[148]). The calculated δ_c values as a function of Mw for the samples analyzed in this study are shown in Figure 3.9A, and show that the enthalpic gain driving multi-segment adsorption becomes more dominant with increasing Mw. Therefore, we may expect that low Mw PS would tend to assume a more isotropic conformation near the interface, while the high Mw PS would tend to maximize the enthalpic gain by increasing the number of polymer/substrate interactions.

The final conformation of the interfacial chains for the low Mw sample is entropically driven, resulting in an isotropic conformation. In this condition, high tilt angles are possible for the pendant phenyl ring to maximize d-π* interactions with silver. In fact, the measured tilt angle for the 20 x10^3 g/mol at the PS/Ag interface resembles the one reported for the same Mw at the PS/air interface[5]. At the air interface, the chains have a higher degree of freedom and there is no enthalpic contribution of adsorption, indicating that this conformation is entropically favorable for this Mw.

On the other hand, for high Mw samples, the significant entropy loss needs to be overcome by the enthalpic gain of multi-segment adsorption. For a high Mw PS sample (Mw = 290 x 10^3 g/mol) near a weakly interacting substrate, Sen et al.[107] hypothesized that multi-segment PS backbone/substrate interactions are responsible for increasing the enthalpic gain in the overall system. The authors suggested that the randomization of the phenyl rings in the vicinity of the substrate occurs to optimize the number of substrate/backbone interactions. This phenomenon is expected to also occur near highly interactive substrates. For long chains, the optimized adsorption of the pendant phenyl ring lying flat on the substrate (d-π* interactions) would require torsions in the polymer chain[11] and the disruption in the local structure would propagate throughout the chain, hindering the multi-segment adsorption. Therefore, we propose that the optimized thermodynamic conformation in enthalpically driven adsorption (high Mw) aims at maximizing the backbone/substrate interactions at the PS/Ag interface, at a cost of tilting the phenyl rings away from the Ag substrate (Figure 3.9B). Due to the Ag-phenyl ring interactions, the phenyl groups assume a high tilt angle maximizing the edge-on interaction with the Ag substrate and possibly π-π interactions between the phenyl rings, instead of the randomized conformation seen at the interface with a weakly interacting substrate as reported by Sen et al.[107].

The intensity of the SFG signal in the backbone region (2800-3000 cm^{-1}) in

Figure 3.4A corroborates this hypothesis as follows. The SFG signal in the backbone region is significantly more intense for the samples with Mw of 100 x10^3 g/mol and 400 x10^3 g/mol compared to the 20 x10^3 g/mol sample, revealing that the number of backbone/substrate interactions is larger for the high Mw samples. The low intensity of the SFG signal in the backbone region for the 20 x10^3 g/mol sample strengthens the theory of the chains assuming a more isotropic conformation at the interface (Figure 3.9B).

The recent findings of Hong et al.[6] highlight the effects of the backbone accommodation as a key factor in the final polymer conformation. In the vicinity of a PS-PMMA blend/graphene interface, the authors reported that at low PS concentrations, the phenyl rings tend to be lying at the interface, to favor π-π interactions with graphene. As the local phenyl ring concentration increases, the phenyl rings are tilted to an upright orientation, in order to optimize π-π interactions between the phenyl rings, while keeping an edge-to-face interaction with graphene. The authors reinforce that this conformation is enthalpically favorable and that the backbone would not be able to accommodate face-to-face π-π interactions with graphene at high phenyl ring concentration.

These findings support our argument of the backbone accommodation playing an important role in the final conformation of PS chains and are in agreement with the differences seen in θ as a function of Mw, since the local phenyl ring concentration is a function of Mw, due to changes in the free volume[122]. In a previous study, our research group has highlighted the difference in the free volume as being one of the main factors in driving differences in θ as a function of Mw at the PS/air interface[5].

The relative amount of chain ends for the different Mw might also be responsible for the changes in tilt angle. The phenyl rings near chain ends have higher mobility and their orientation can be easily adjusted to optimize the interactions with the substrate. Delle Site et al.[121] reported the chemisorption of chain ends containing aromatic groups in polycarbonate melt in contact with nickel. Tsuruta et al.[10] showed the segregation of PS chain ends in the vicinity of a quartz substrate. Therefore, it is reasonable to assume that the adsorption of chain ends also occurs at the PS/Ag interface, and that the relative amount of the chain ends, which is a function of Mw (% of chain ends = 2/N*100 = 1%, 0.2% and 0.05% for 20 x 10^3 g/mol, 100 x 10^3 g/mol and 400 x 10^3 g/mol, respectively), is also affecting the measured tilt angle of the phenyl rings.

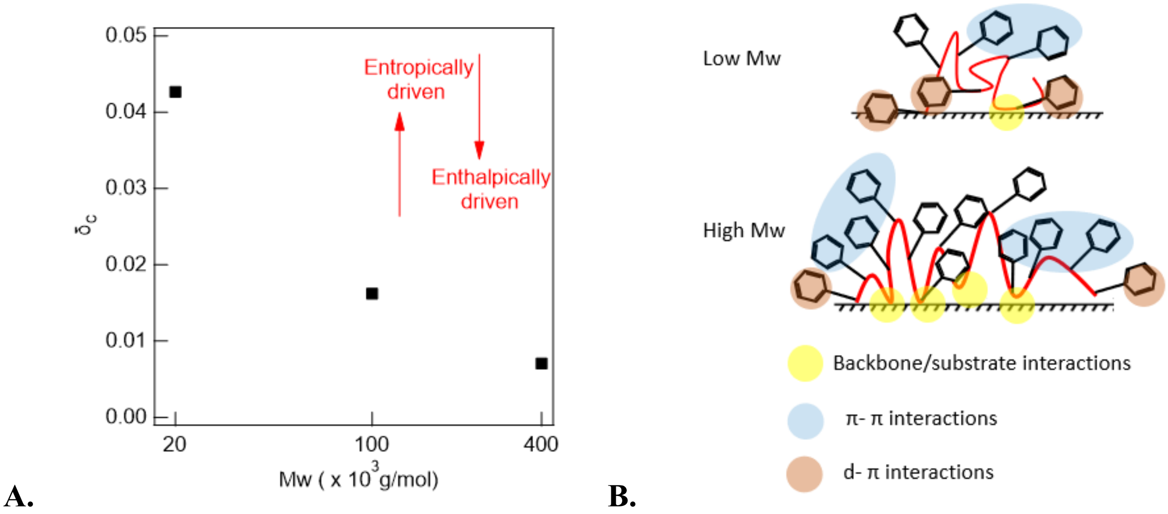

Figure 3.9.A. δ_c as a function of Mw and B. Scheme of interfacial structure for low and high Mw PS. Low Mw: An entropically driven isotropic backbone conformation exists at the interface and the enthalpy is maximized by d-π* interactions and a high tilt angle enabled by torsions in the backbone; High Mw: An enthalpically driven tail-loop-train backbone conformation exists with phenyl rings tilted to maximize backbone/substrate interactions, while the enthalpy is also increased by π-π interactions between phenyl groups and edge-on interactions with the substrate.

3.7. Conclusions

The effect of the Mw on the conformation of PS chains in the vicinity of the PS/Ag interface was investigated by SFG. The spectra of PS samples with Mw ranging from (20 x 10^3 g/mol to 400 x 10^3 g/mol) were acquired in the backbone and phenyl ring C-H stretch regions. The determination of the possible values for the tilt angle of the pendant phenyl ring was performed by analyzing the vibrational resonances amplitudes in the ssp and ppp spectra.

In the backbone region, the intensity of the SFG signal increased with increasing Mw, revealing a higher number of backbone/substrate interactions for the high Mw samples. In the phenyl ring vibrational region, a strong correlation between the amplitude of the ν_2 vibrational mode and Mw was identified. The amplitude of this vibrational mode significantly increases with increasing Mw, indicating a trend of decreasing the tilt angle as Mw increases. The range of possible values for θ was calculated using the ratio of the ν_2 amplitudes in ssp and ppp polarization, showing that high tilt angles $\theta \geq 50°$ occurred for all samples. These high tilt angles near the silver surface are comparable with previous research of PS conformation near highly interactive substrates and they suggest a strong interaction between the phenyl rings and the metal surface for the lowest Mw sample. Furthermore, the analysis of the tilt angles shows a trend of decreasing average angle with increasing Mw.

We hypothesize that the enthalpy/entropy balance during the polymer adsorption plays a key role in driving the PS conformation. We suggest that the high Mw samples adsorb on the silver interface through an enthalpic-driven process, in which the high number of backbone/substrate interactions per chain is responsible for maximizing the adsorption enthalpic gain. The phenyl rings are tilted away from their most stable conformation (lying at the interface) to optimize the backbone/substrate interactions and accommodate the backbone conformation. The observed smaller tilt angles at higher Mw may also be facilitated energetically due to π-π interactions between the aromatic rings. Furthermore, we propose that the final conformation of the low Mw PS is entropically driven, in which the entropy is maximized by a nearly isotropic backbone conformation near the interface and the system benefits energetically from the enthalpic gain of the phenyl rings d-π^* interactions with the substrate (θ~80°). We believe that this study provides significant insights about the dependence of the orientation and conformation of the adsorbed polymer chain on its Mw at metal/polymer interfaces.

Chapter 4 . The role of interfacial polymer conformation on the dewetting behavior of thin films

4.1. Preface

This chapter presents a journal manuscript prepared for submission.

In the previous chapter, we demonstrated that the molecular weight of polystyrene significantly influences the conformation of polymer chains near a silver substrate. Building on this foundation, this study explores the effect of molecular weight on the interfacial conformation of polystyrene chains near two distinct interfaces: the air interface and a highly interactive mica substrate. Furthermore, we establish a connection between interfacial chain conformation and the dewetting behavior of polymer thin films.

In this work, we investigated the conformation of polystyrene chains at the free surface and near a mica substrate as a function of molecular weight. By integrating theoretical calculations of entropic and enthalpic contributions to adsorption and SFG spectroscopy orientation analysis, we developed a model linking interfacial chain conformation to the dewetting behavior of thin polymer films.

Our results reveal significant differences in chain conformation at the two interfaces. At the air interface, chains predominantly exhibit isotropic conformations regardless of molecular weight. However, near the mica substrate, high molecular weight chains tend to adopt an extended conformation, driven by the enthalpic benefits of multisite adsorption. This extended backbone conformation enhances film stability and significantly reduces the dewetting rate compared to films where chains assume an initial coiled conformation of the same molecular weight.

These findings provide valuable insights into the role of interfacial polymer conformation in governing the macroscopic properties of polymeric materials. This work opens the way for further studies linking molecular-scale conformations to the bulk behavior of polymer thin films, with implications for materials design and application.

Minor adjustments, including the numbering of figures, tables, and references, were made to ensure consistency with the rest of the thesis. Since the following manuscript is presented in its entirety, there may be some overlap with other sections of the thesis, such as repeated descriptions of abbreviations and equations.

4.2. Abstract

Effectively understanding, controlling, and tailoring the dewetting behavior of polymeric thin films is essential for enhancing their stability and performance across a wide range of applications. This behavior is closely tied to the nature and strength of the interactions between polymer chains and the substrate. In this study, we employed theoretical calculations and sum frequency generation (SFG) spectroscopy to explore the correlation between the initial conformation of polymer chains near the substrate and the films dewetting behavior. Our results reveal that the films thermal-mechanical history, including the annealing conditions and interfacial environment (whether buried or exposed), can significantly alter the interfacial chain conformation, subsequently influencing dewetting dynamics. The molecular weight of the polymer and the chain initial conformation play critical roles in determining the dewetting rate of films placed in contact with weakly interacting substrates. For chains with a coiled initial conformation, the dewetting rate increases rapidly with the sample molecular weight due to the greater entropic cost of adsorption. On the other hand, in films where chains exhibit an extended initial conformation, a higher molecular weight results in a greater number of polymer-substrate interactions, leading to a reduced dewetting rate. This explains low dewetting rates observed for high molecular weight polystyrene samples having an initially extended conformation, despite their high entropic cost of adsorption. Through a comprehensive analysis, we established clear correlations between chain molecular weight, annealing conditions, interfacial chain conformation, and dewetting dynamics. These findings provide valuable insights into the interplay between molecular structure and the macroscopic behavior of thin films, offering guidance for optimizing film stability in various applications.

4.3. Introduction

The dewetting behavior of polymer thin films holds significant scientific interest, and a deep understanding of this process is essential for numerous technological applications, such as high-performance coatings[149–151], electronics[152] and optical devices[153,154]. In most processes, dewetting is undesirable as it compromises the long-term stability of the film. To address this, various strategies have been developed to prevent and suppress dewetting in polymer thin films[155], such as the addition of nanofillers[149,156], modifying substrate surface parameters[157] and applying capping materials to the film surface[158]. Nonetheless, dewetting can be highly desired, as precise control of dewetting is a powerful strategy to create unique micro and nanopatterns in polymer thin films[159–163], which can further be used as templates for inorganic pattern fabrication[164,165].

Dewetting experiments provide valuable insights into the rheological and frictional properties of polymer melts[166]. In particular, dewetting is closely associated with slip at the polymer/substrate interface[54,167]. By analyzing the profile of the dewetting hole, key flow dynamics parameters, such as the slip length, can be determined[168,169]. This is because slippage at the polymer/substrate interface significantly affects both the dewetting velocity and the morphology of the rim formed during film retraction[168].

The dewetting process depends on several factors that influence the overall balance of entropy and enthalpy of the chains near the substrate[170]. The enthalpic gain from the interactions between the adsorbed chains and the substrate represents a resistance force to dewetting. On the other hand, the conformational entropic cost from the confinement of the chains near the substrate is an important driving force for the occurrence of dewetting[54].

The adsorption strength, which can be tailored by changing the binding energy between the polymer and the substrate[54,171], has a key role in regulating the dewetting pattern and kinetics. The stronger the adsorption strength, the higher the enthalpic gain per polymer-substrate interaction, and the higher the resistance to pulling out the binding points between the chains and the substrate. Several studies have reported the effect of the adsorption strength on the dewetting behavior of polymeric thin films for various pairs of polymer/substrate[54,171–173]. Generally, these studies show that the weaker the polymer's adsorption onto the substrate, the faster will be the dewetting process.

The chain architecture is also an important factor affecting the dewetting process. For molecules with similar chemical composition and molecular weight (MW), the effect of chain architecture on dewetting can be rooted in the differences in the entropic penalty of adsorption and in the chain's ability to make multiple interactions with the substrate[170,174]. For example, when comparing the dewetting behavior of linear, star, and ring polystyrene (PS) of similar MW, Wang et al.[167] showed that the dewetting kinetics are drastically affected by the chain architecture, with star and ring PS exhibiting lower dewetting rates compared to their linear counterparts [167].

The relationship between the polymer chain length and the dewetting behavior of thin films is a complex and multifaceted subject, as the chain length affects the polymer viscosity[175], level of entanglements, and entropy/enthalpy balance[51]. Increasing the polymer chain's length has a favorable enthalpic effect on the wetting process, arising from the greater number of possible polymer-substrate interactions per chain. On the other hand, it has a detrimental effect from the increased entropic cost of adsorption of longer chains, which drives dewetting. Due to this competition of enthalpic and entropic contributions, the understanding of the effect of the polymer chain length on the dewetting process requires case-specific attention. McClements et al. explored the effect of the chain length of poly(styrene-co-butadiene) on the wetting behavior of thin films[172,173]. When deposited on weakly adsorbing substrates (low adsorption energy per polymer-substrate contact point), the entropic factors dominated, and the increase in the chain length reduced its overall affinity towards the substrate. An opposite trend was observed when the films were deposited on a strongly adsorbing substrate (high adsorption energy per polymer-substrate contact point) under the same conditions. The enthalpic factors dominated the adsorption process, with longer chains having enhanced affinity towards the substrate. These observations can be explained in terms of polymer adsorption's entropy/ enthalpy balance. Near weakly adsorbing substrate, the substantial entropic loss of polymer confinement, which increases with chain length, represents a barrier for the adsorption of long chains. On the other hand, near strongly adsorbing substrates, long polymer chains benefit from the substantial enthalpic gain of a greater number of polymer-substrate interactions, which overcomes the confinement entropic cost. Similarly, Peschka et al.[176] observed faster dewetting and an increase in the film instability with increasing the polymer chain length. In contrast with these previous studies, Reiter et al.[166] and Xu et al.[171] observed a decrease in the velocity of dewetting with increasing the polymer chain length. According to Reiter and de Gennes[101], the chain's initial out-of-equilibrium conformation resulting from the film deposition method (e.g. spin coating) can contribute to unexpected dewetting behaviors of polymer thin films.

A recent study of Li et al.[18], revealed significant differences in the conformation of the chains at the surface and near the substrate during the dewetting of PS films. In fact, many authors have reported that the conformation of the chains near the substrate significantly influences the dewetting behavior of polymer thin films. For example, Li et al. [19] demonstrated that the conformational changes of the buried interfacial chains during prolonged annealing of PS were responsible for promoting dewetting. Furthermore, Barkley et al.[108] demonstrated that the presence of nanoparticles near the interface alters the conformation of interfacial adsorbed chains, and these conformational differences are directly linked to the dewetting suppression effect of nanoparticle filling. Lastly, the intriguing findings of Sabzevari et al.[50] on the influence of the sample's thermal and mechanical history on the dewetting behavior of thin films reinforce the importance of further exploring the theme. The authors analyzed the dewetting behavior of linear PS thin films of various MW transferred to hydrophobic substrates by flotation after being initially deposited and annealed on freshly cleaved mica substrates. The authors compared the differences in the dewetting dynamics when each of the two interfaces (the buried and the free interfaces) of the films was transferred to the hydrophobic substrate. While low MW samples exhibited similar dewetting behavior, regardless of the interface transferred, a substantial disparity in the dewetting dynamics for the two interfaces of the same film occurred for high MW samples. Faster dewetting occurred when the film surface was transferred to the hydrophobic substrate, compared to when the buried interface was transferred. These results suggest that the changes in the conformation of the interfacial chains during the annealing stage are reflected in the different dewetting behaviors of the two interfaces of the films.

Beyond the aforementioned aspects, various other factors such as the film thickness[177–179], the substrate surface roughness[157], and the segregation of one component to the interfacial region in polymer blends [180] also affect the dewetting dynamics and kinetics. The previously mentioned multi-dimensional and eventually divergent observations highlight the challenges for achieving a molecular-level understanding of dewetting and demonstrate the need to further link the macroscopic dewetting behavior with molecular-level properties. In the present study, we investigated the correlation between the dewetting behavior of PS thin films and the chain conformation as a function of the polymer MW. We combined theoretical calculations of the entropy/enthalpy balance of the adsorbed chains with experimental data of interfacial chain conformations of PS samples exhibiting varying dewetting behaviors to establish the relationship between the sample chemical, thermal, and mechanical history, the polymer MW, and the dewetting behavior of thin films. This study contributes to achieving a deeper understanding of the relationship between molecular structures and macroscopic film behavior.

4.4. Methodology section

4.4.1. Theoretical calculations of the free energy of adsorption

4.4.1.1. Case study: polystyrene films

The work of Sabzevari et al.[50] was selected as a case study for theoretical calculations to elucidate the relationship between the adsorption entropy and enthalpy and the observed dewetting behavior of polymers. In their study, the authors deposited films of PS with various MW on mica substrates. These films were then thermally annealed (150 °C for 1h) and transferred to hydrophobic substrates (hydrophobized silicon wafers produced by silanization using dodecyl tri-dichlorosilane (DTS)) by flotation for subsequent dewetting studies. During the film transfer, the researchers selectively placed either the top or the bottom interface of the film in direct contact with the hydrophobic substrate. This was achieved by catching the floating film either from the surface or from beneath the water. A schematic representation of the methodology employed by the authors is presented in Figure 4.1 A.

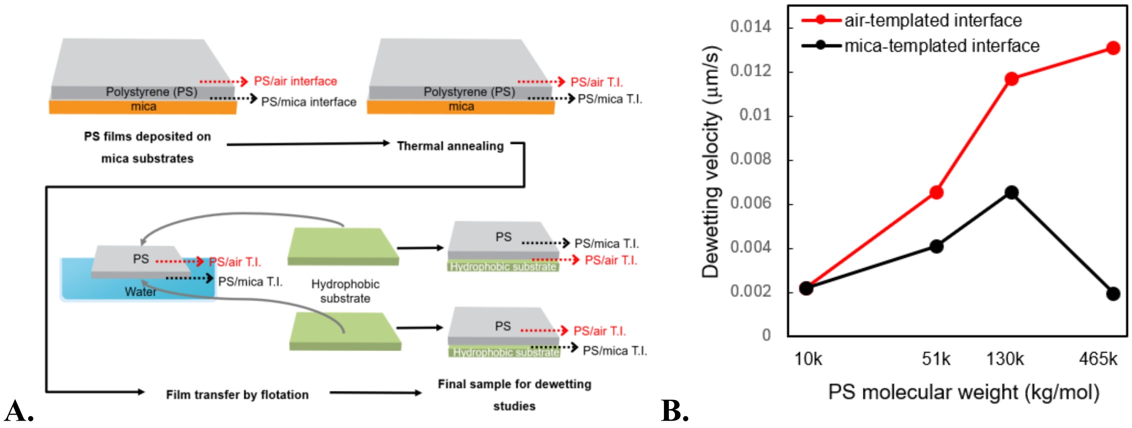

Figure 4.1. A. Schematic illustration of the sample preparation method for dewetting studies, according to Sabzevari et al.[50]; and B. Trend in dewetting velocity (originally reported in terms of slip length) of the films as a function of the molecular weight. Each curve is named based on the interface that was placed in direct contact with the hydrophobic substrate. Here, T.I. indicates templated interface.

The dewetting velocity trend reported by Sabzevari et al.[50] is illustrated in Figure 4.1 B. In summary, low MW samples (10 kg/mol) exhibited slow dewetting velocity regardless of which interface was placed in contact with the hydrophobic substrate. However, for high MW samples ($MW \geq 51 kg/mol$), there was a significant disparity in dewetting velocity between the two interfaces. Faster dewetting occurred when the air-templated interface was placed in contact with the hydrophobic substrate, for all samples.

Based on these observations of the dewetting behavior of PS thin films, we conducted a theoretical analysis to examine the effects of polymer molecular weight, polymer-substrate adsorption energy (ϵ_{ad}), and interfacial chain conformation on the free energy of adsorption. First, we examined the expected templated conformations of the PS chains annealed in contact with air and with the mica substrate. Then, we assessed the free energy of adsorption of the PS chains on a hydrophobic substrate considering different initial chain conformations (coiled and extended). The purpose of these calculations was to explore how the order of magnitude of the free energy of adsorption (ΔG) can be affected by the chain's initial conformation, and its expected influence on the dewetting behavior of the films. The molecular weight of the samples used in the theoretical analysis are the ones used on the SFG experiments, to allow posterior comparison of the results. However, they fall within the range of MW used during Sabzevari's study[50].

4.4.1.2. Theory of the free energy of adsorption of polymers

The adsorption of polymers at interfaces is governed by the balance between entropy and enthalpy in the system. When polymers adsorb onto substrates, they lose conformational entropy. Therefore, adsorption will occur spontaneously only if the enthalpic gain from adsorption surpasses this entropic loss. The higher the adsorption energy between the polymer and the substrate (ϵ_{ad}, adsorption energy per point of polymer-substrate interaction) the greater the enthalpic gain per chain. The adsorption energy is determined by the type and strength of the chemical interactions between the polymer and the substrate. This energy can range from fractions of $-k_bT$ (where k_b is the Boltzmann constant and T is the absolute temperature) for weak van der Waals interactions, up to approximately $-12\ k_bT$ for strong hydrogen bonding[181,182].

Spontaneous adsorption can occur even when the adsorption energy of each polymer-substrate interaction is very small. This is because each polymer chain can make multiple interactions with the substrate through multi-segment adsorption, thereby increasing the total enthalpic gain per chain[182]. However, only a fraction of the monomers in a polymer chain will effectively adsorb onto the substrate. Adsorbed polymer chains are typically described as being composed of trains (segments adsorbed on the substrate), loops (segments between the trains that are not adsorbed on the substrate), and tails (end segments not adsorbed on the substrate)[148]. Among these, only the trains contribute to the enthalpic gain of adsorption through effective polymer-substrate interactions. The higher the adsorption energy, the greater the fraction of adsorbed monomers per chain[183].

The fraction of adsorbed monomers is also influenced by the chain flexibility, measured in terms of the Kuhn segment length (b)[183,184]. While the Kuhn segment length has little impact on the fraction of adsorbed monomers at low adsorption energy values, at high adsorption energy values, more rigid chains (with larger Kuhn segment lengths) tend to have a higher fraction of adsorbed monomers[183]. The polymer molecular weight is another factor that influences the number of polymer-substrate contact points per chain. The higher the polymer molecular weight, the greater the number of possible polymer-substrate contact points per chain, leading to higher adsorption enthalpic gain[182]. In practice, non-equilibrium conditions can alter this expected adsorption behavior[101].

The conformational entropic loss during adsorption arises from the confinement of the polymer chain in the interfacial region between the bulk polymer and the substrate, as well as the immobilization of the adsorbed segments. Although calculating the entropic cost of polymer adsorption is challenging, it can be estimated using a parallel plate confinement model[185,186]. In this model, the polymer chain is considered to be confined between two plates at a distance d from each other. The closer the plates (i.e., the smaller the value of d), the higher the level of confinement and the greater the entropic loss. In addition to the absolute value of d, the ratio d/P (where P is the chain's persistence length, $2P = b$) also dictates the level of confinement. Strong confinement occurs when $d/P \ll 1$, while weak confinement occurs when $d/P \gg 1$. Smyda and Harvey[185] reported that the entropic cost of confinement ($-T\Delta S$ per chain persistence length) can range from $\sim 0.01\ k_bT$ for $d/P = 50$, to $\sim 9k_bT$ for $d/P = 0.1$.

For the calculations presented in this work, the adsorption energies, based on data from available literature, have been approximated to suit the specific conditions of this study. Additionally, the enthalpic gain was assumed to arise solely from the interactions between the polymer and the substrate and the adsorption entropy was estimated by considering the entropic loss due to the confinement of a polymer chain between two plates.

4.4.2. Probing the interfacial conformation of PS chains

Aiming to elucidate the origin of the dewetting disparity between the two interfaces of the same PS film reported by Sabzevari et al.[50], we used sum frequency generation (SFG) spectroscopy to probe the conformation of interfacial PS chains.

Monodisperse polystyrene samples with M_n of 27, 130 and 344 kg/mol from Polymer Source, Inc. were used as received. These values of MW were chosen as they fall between the range of PS MW used for the study of Sabzevari et al.[50] Thin films of PS of ~100 nm were produced by spin-coating PS solutions in toluene onto freshly cleaved mica substrates. The concentration of the PS solutions ranged from 1% to 1.75% w/w, depending on the polymer MW, to achieve the desired thickness. Film thickness was measured with a DEKTAK 150 profiler, using the method previously reported[187,188]. The films deposited on mica were vacuum-dried for 48 hours in a desiccator filled with silica gel desiccant beads. Then, the films were annealed at 150 °C for 1h under nitrogen atmosphere. The thin films were floated in HPLC-grade water (Sigma Aldrich) and transferred to fused silica optical windows (IR grade, ISP Optics Corp.). The optical windows were previously cleaned with hot piranha solution (80 °C, 3:1 H_2SO_4/30 vol % H_2O_2) for one hour, then thoroughly rinsed with HPLC-grade water until neutral pH was achieved. The transfer from the water bath to the optical window was achieved by collecting either the top or bottom interface of the film. The experimental design for film preparation is similar to the one illustrated in Figure 4.1 A, with the modification of using an optical window instead of a hydrophobic substrate to collect the films from water. The films were submitted to a second round of drying under vacuum for 48 hours and then used for SFG measurements.

Detailed information about our SFG system (EKSPLA) can be found in our previous publications[5,187,188]. The spectra were collected with the incident beams coming through the optical window and being reflected at the polymer/air interface. This geometry allows to selectively probe the conformation of the PS chains present at the polymer/air interface, with minimum signal contribution from the chains at the polymer/silica interface[187]. Therefore, the samples produced by catching the PS films from the top and bottom interfaces can be used to probe the conformation of mica-templated and air-templated interfacial chains, respectively.

SFG spectra were obtained using ssp and ppp polarizations, with each letter representing the polarization state of the SFG, visible, and IR beams, respectively. To compensate for fluctuations in laser power, the SFG signal was normalized by the product of the visible and IR beam energies[187,188]. Additionally, the frequency calibration was performed using the spectrum of poly(methyl methacrylate) (PMMA), which has a prominent resonance at 2955 cm^{-1}. Each SFG spectra used to analyze the PS chain conformations is the average of at least 10 spectra collected from at least five film specimens. The SFG spectra parameters (e.g. the amplitudes of the vibrational modes) were obtained by fitting the SFG spectra with a Lorentzian equation (Equation B1 of Appendix B)[187,188]. The SFG spectra of the PS films analyzed in the present study fitted with Equation B1 are shown in section B2 of Appendix B. We employed two methods[5–7,187,188] to determine the range of possible tilt angles of the PS phenyl ring (θ, the angle between the C_2 axis of the phenyl ring and the surface normal). The reported values represent the overlap between the results obtained from each method. Further details about each method used, and their individual angle range results are provided in section B3 and B4 of Appendix B.

4.5. Results and discussion

4.5.1. Theoretical analysis of the free energy of adsorption

4.5.1.1. Templated interfacial chain conformation after thermal annealing

According to the procedure of Sabzevari et al.[50], PS thin films deposited on mica were thermally annealed. Thermal annealing allows for the relaxation and conformation rearrangement of the interfacial chains. It has been previously demonstrated that the conformation of interfacial chains near adsorbing substrates and free surfaces can be substantially different[7,8]. Therefore, one may expect differences in the conformation of the chains that were in contact with air, and in contact with mica after thermal annealing.

4.5.1.2. Chain conformation at the air-templated interface

Under equilibrium conditions, polymer chains near the air interface predominantly adopt a random coil Gaussian conformation[189]. The chains at the interface lose conformational entropy, which makes their presence in the interfacial region unfavorable[103]. In the absence of an attractive force capable of drawing multiple chain segments to the interface – such as that provided by a highly interactive substrate - the conformation of these interfacial chains will aim at minimizing the number of segments exposed to the interface, with the majority of the chain remaining coiled within the bulk.

It is important to note that while the functional groups at the interface may have a preferred orientation with respect to the surface normal[5,8,190], most of the chain's segments remain buried within the bulk, retaining an isotropic conformation.

4.5.1.3. Chain conformation at the mica-templated interface

Mica is a type of phyllosilicate with perfect cleavage planes. The surface of freshly cleaved mica contains potassium cations, hydroxyl groups, and atoms of silicon, aluminum, and oxygen[191]. Polystyrene can interact with mica both through its pendant phenyl rings and its carbon backbone. Strong $cation - \pi$ interactions may occur between the phenyl rings and the potassium ions on the mica surface, with a maximum adsorption energy of approximately $-79\ kJ/mol$, as observed in the interaction between benzene and K^+ ions[192]. Additionally, weaker $OH - \pi$ interactions can occur between the phenyl groups and the hydroxyl groups on mica, with an estimated adsorption energy of around$-30\ kJ/mol$, based on benzene adsorption on a silica substrate, which is also rich in OH groups [193]. The adsorption energy of the polystyrene backbone, which is composed of CH, CH_2 and CH_3 groups, was estimated based on the reported adsorption energy of octane on kaolinite, which is another type of phyllosilicate. The backbone adsorption energy per PS monomer was estimated to be approximately $-14\ kJ/mol$ at $373\ K$, considering it to be one-quarter of the adsorption energy of a single octane molecule on kaolinite[194]. The temperature of $373\ K$ is used in our modeling, as the dewetting studies were performed above the glass transition temperature of polystyrene, which is approximately $373\ K$. The adsorption enthalpic gain (ΔH_{ad}) arising from the polymer-substrate interactions can be estimated according to Equation 4.1, where N is the number of monomers in the chain and Θ is the fraction of adsorbed monomers.

$$\Delta H_{ad} = \epsilon_{ad} N \Theta \qquad \text{Equation 4.1}$$

Multisite interactions between the pendant phenyl rings and the substrate requires substantial torsions in the PS chain backbone[11,188]. Additionally, estimating the ratio between phenyl ring and backbone interactions remains challenging, even with extensive computational efforts. Therefore, for simplicity, we will consider exclusively the backbone-substrate interactions for the calculation of ΔH_{ad}. In this scenario, for PS adsorbed on mica, the fraction of adsorbed monomers is ~0.85, according to the molecular dynamics simulation of Kramarenko[183]. The calculated magnitude of ΔH_{ad} for PS with various MW on mica are presented in Table 4.1.

To estimate the entropic cost of confinement, we must first assess the thickness of the adsorbed layer, since that determines the value of d. This parameter is estimated to be around 2 nm, using the measurements of Sen et al.[107] for the thickness of the adsorbed layer of polystyrene on silicon oxide substrates after 1 hour of annealing. Therefore, $d/P \cong 2$ and $-T\Delta S \cong 0.34\ kT$ per persistence length[185,195]. The estimated magnitudes of the entropic cost of confinement ($-T\Delta S$) of the PS samples are shown in Table 4.1.

Table 4.1. Adsorption parameters for PS adsorption on mica

PS molecular weight $(\boldsymbol{kg/mol})$	PS/mica adsorption parameters $(\boldsymbol{kJ/mol})$	
27	$-0.3x10^4$	$\boldsymbol{\Delta H_{ad}}$
130	$-2x10^4$	
344	$-4x10^4$	
27	$0.6x10^2$	$\boldsymbol{-T\Delta S}$
130	$3x10^2$	
344	$8x10^2$	
27	$-0.3x10^4$	$\boldsymbol{\Delta G}$
130	$-2x10^4$	
344	$-4x10^4$	

Accounting for the enthalpic gain and entropic cost of adsorption, the total free energy of adsorption can be estimated (Table 4.1). For all MW analyzed, the enthalpic gain of adsorption on mica overcomes the entropic cost, and $\Delta G < 0$, leading to spontaneous adsorption. Figure 4.2 provides an overview of the magnitude of the adsorption parameters for the PS adsorption on mica. The higher the PS MW, the greater the magnitude of ΔH_{ad} and ΔG. It is also possible to observe that, even though the magnitude of the entropic cost of adsorption scales with MW, this scaling is minimal compared to the increase in ΔH_{ad} with MW. Additionally, for low MW, the contribution of the entropic factor to ΔG is significant, while for high MW, the contribution of the entropic factor to ΔG is negligible.

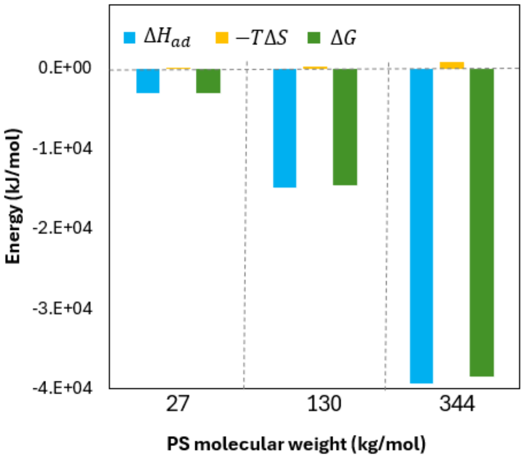

Figure 4.2. Adsorption parameters for PS adsorption on mica.

These results are in agreement with the de Gennes scaling theory[123] and can be used to elucidate the conformation of interfacial chains near strongly adsorbing substrates. According to the theoretical work of Bouchaud and Daoud[51], the conformation of the chains near substrates is substantially influenced by the chain length. For short chain adsorption, entropic factors dominate, and the interfacial chains will tend to assume an isotropic conformation near the substrate. On the other hand, for long chain adsorption, enthalpic factors dominate, and the chains will assume an extended conformation near the substrate, to maximize the number of polymer-substrate interactions.

Based on these calculations, we hypothesize that the conformational templating effect of the thermal annealing in contact with mica depends on the chain MW. Low MW PS chains will have an isotropic conformation near the substrate (due to the balanced competition of entropic and enthalpic factors), and high MW PS chains will have an extended conformation near the substrate, as enthalpic contributions dominate the adsorption process. The same relationship between the interfacial chain conformation and the chain MW was previously observed for the PS/silver interface, which is also a strongly adsorbing substrate for PS[188].

4.5.2. Effect of the initial chain conformation on the dewetting behavior

In the previous section, we examined the expected conformational differences between the mica-templated and air-templated interfaces. Here, we will investigate how the initial chain conformation—shaped by the templating process—affects the dewetting behavior of PS films when transferred to hydrophobic substrates.

4.5.2.1. Coiled chains (air-templated interface) transferred to the hydrophobic substrate

Hydrophobic substrates are commonly used in dewetting studies due to their non-sticking properties. The PS interactions with these substrates are through van der Waals interactions, with an adsorption energy of approximately $-3\ kJ/mol$ at $373\ K$[196]. If we consider a random coil initial conformation, under equilibrium, the fraction of adsorbed monomers is approximately 0.06[183]. It is important to note that, since at low adsorption energies the chains will tend to desorb from the substrate, to estimate this value of Θ, Kramarenko et al.[183] considered the first atom of the chain to be grafted to the surface. Therefore, we may conclude that for free chains $\Theta \leq 0.06$.

Estimating the thickness of the adsorbed layer in contact with the hydrophobic substrate is challenging. Since the chains desorb in contact with this substrate, there is a lack of experimental measurements of this condition. For this model, we consider the same thickness of the adsorbed layer, and therefore the same entropic cost of confinement used in the calculations in section 4.5.1.3. This is made because the chains near the hydrophobic substrate will be weakly adsorbed, and a difference of only 0.3 nm in the thickness of strongly adsorbed and weakly adsorbed PS samples on sapphire was previously reported[105]. We reinforce that small differences in the thickness of the adsorbed layers would not alter the comparison in terms of the order of magnitude of the adsorption parameters performed in this study. The calculated values of ΔH_{ad}, $-T\Delta S$, and ΔG are presented in Table 4.2.

Table 4.2. Adsorption parameters for PS adsorption on a hydrophobic substrate, varying the chain's initial conformation.

PS molecular weight $(\boldsymbol{kg/mol})$	Adsorption parameters $(\boldsymbol{kJ/mol})$			
	Coiled initial conformation (air-templated interface)	Extended initial conformation (mica-templated interface) 7.0%*	Extended initial conformation (mica-templated interface) 9.0%*	
27	$-0.5x10^2$	$-0.5x10^2$	$-0.6x10^2$	$\boldsymbol{\Delta H_{ad}}$
130	$-2x10^2$	$-2x10^2$	$-3x10^2$	
344	$-6x10^2$	$-6x10^2$	$-8x10^2$	
27	$0.6x10^2$	$0.6x10^2$	$0.6x10^2$	$\boldsymbol{-T\Delta S}$
130	$3x10^2$	$3x10^2$	$3x10^2$	
344	$8x10^2$	$8x10^2$	$8x10^2$	
27	$0.1x10^2$	$0.1x10^2$	$-0.8x10^1$	$\boldsymbol{\Delta G}$
130	$0.6x10^2$	$0.6x10^2$	$-0.4x10^1$	
344	$2x10^2$	$2x10^2$	$-1x10^1$	

* The percentages indicate the amount of polymer/substrate interactions that were effectively transferred from the mica to the hydrophobic substrate.

The results show that the enthalpic gain of adsorption does not overcome the entropic penalty and $\Delta G > 0$ for all MW analyzed, leading to a tendency of dewetting when the chains are placed in contact with a hydrophobic substrate. The dewetting velocity will then depend on the magnitude of the driving force for dewetting (the entropic penalty) and the resistance force of dewetting (the enthalpic gain)[54].

The comparison of the magnitude of ΔH_{ad}, $-T\Delta S$, and ΔG is shown in Figure 4.3 A. Even though ΔH_{ad} scales with the PS MW, the enthalpic gain is insufficient to overcome the entropic penalty of adsorption. The higher the PS MW, the greater the magnitude of the entropic contributions and of ΔG, leading to faster dewetting.

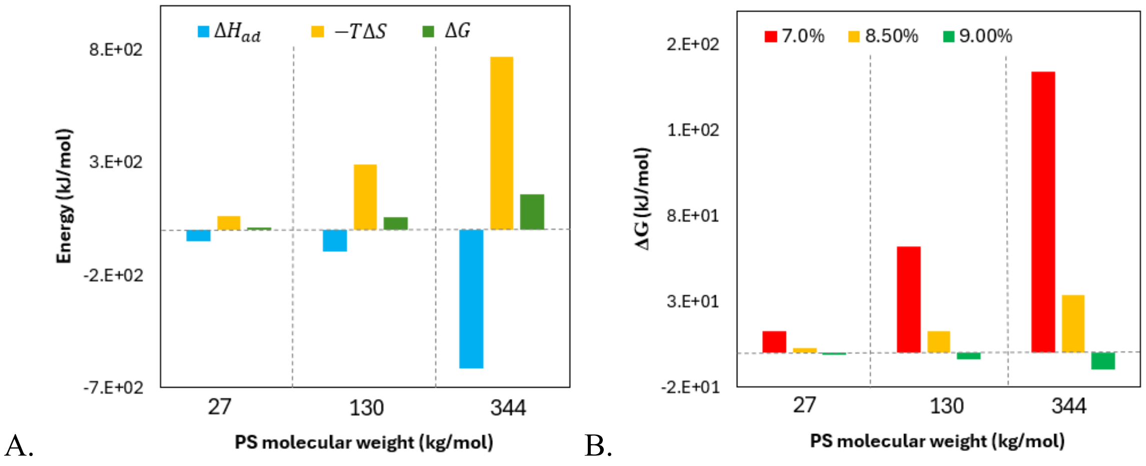

Figure 4.3. A. Adsorption parameters for PS adsorption on a hydrophobic substrate (initial coiled conformation); and B. Free energy of adsorption for PS on a hydrophobic substrate (initial extended conformation), where the percentages indicate the amount of polymer-substrate interactions that were effectively transferred from the mica to the hydrophobic substrate.

4.5.2.2. Extended chains (mica-templated interface) transferred to the hydrophobic substrate.

To assess the influence of the chain initial conformation on the free energy of adsorption, we simulate the placement of extended chains (eg. PS chain conformation templated in contact with mica) in contact with a hydrophobic substrate. The extended chain conformation allows for an increased number of initial polymer-substrate interactions, which increases the enthalpic gain of adsorption per chain. In theory, the conformation of the chains templated near the mica substrate are extended in a way that allows a fraction of adsorbed monomers of $\Theta \sim 0.85$[183] (see section 4.5.1.3). The substrate transfer from mica to the hydrophobic substrate will likely cause a significant reduction in the number of effective contact points between the polymer and the new substrate. Figure 4.3 B compares the effect of increasing the number of polymer-substrate interactions in terms of the percentage of the initial Θ that will be effectively transferred from mica to the hydrophobic substrate. It is possible to see that even if only a small portion of the initial polymer-mica interactions are transferred to the hydrophobic substrate, this has a major effect on ΔG .The threshold at which ΔG switches its signal is between 8.5 and 9% of the initial value of Θ. It is important to mention that this signal change in ΔG will not avoid dewetting as this is an out-of-equilibrium initial conformation. However, it can help stabilize the films and drastically reduce the dewetting kinetics.

4.5.3. Overview of the relationship between initial chain conformation and the dewetting behavior of thin films.

In the previous sections, we calculated the magnitudes of the entropic and enthalpic factors acting on polymer chains when placed on hydrophobic substrates, based on the chain's initial conformation. We have postulated that the balance between enthalpic and entropic factors plays a crucial role in dewetting kinetics. Furthermore, we hypothesized that the disparities in the dewetting rate for the two interfaces of high MW films arise from an initial higher number of adsorbed monomers, which is only possible for extended chains, and can enhance the film stability, and reduce the dewetting rate. In this section, we summarize these findings and explore the relationship between the theoretical values of the adsorption entropy and enthalpy, with the experimental observations of Sabzevari et al.[50] on the dewetting behavior of thin films.

Figure 4.4 illustrates the relationship between the initial conformation of the polymer chains and the resulting dewetting rate. Low MW PS samples exhibited a low dewetting rate, regardless of the interface transferred onto the hydrophobic substrate (Figure 4.1 B). Since the driving force for dewetting, namely the entropic cost of adsorption, is low for both interfaces, the dewetting rates remain slow in both cases. In contrast, high MW samples experience a higher entropic cost of adsorption, leading to faster dewetting, in the absence of other forces that could stabilize the films. For these samples, conformational templating had a significant impact on dewetting kinetics, with air-templated chains exhibiting faster dewetting and mica-templated chains showing slower dewetting rates (Figure 4.1 B). This effect can be attributed to the greater number of polymer-substrate interactions possible when the chains adopt an initial extended initial conformation.

The relationship between the chain's initial conformation and dewetting kinetics, as hypothesized in this study, offers a compelling explanation for the increasing dewetting rates with molecular weight (MW) in air-templated PS samples (Figure 4.1 B), driven by the increase in the adsorption entropy. It also accounts for the slow dewetting rates observed in the 10 and 465 kg/mol mica-templated samples. However, this hypothesis alone does not fully explain the trends seen in mica-templated interfaces of intermediate MW samples (51 and 130 kg/mol), which exhibited an unexpected increase in dewetting rates before sharply decreasing for the 465 kg/mol sample. To verify our hypothesis, better understand the behavior of intermediate MW samples, and explore other conformational factors that could contribute to the dewetting rate disparity between interfaces, such as phenyl ring ordering and chain-end segregation, we performed SFG spectroscopy studies to investigate the interfacial conformation of the samples. The results are summarized in the following section.

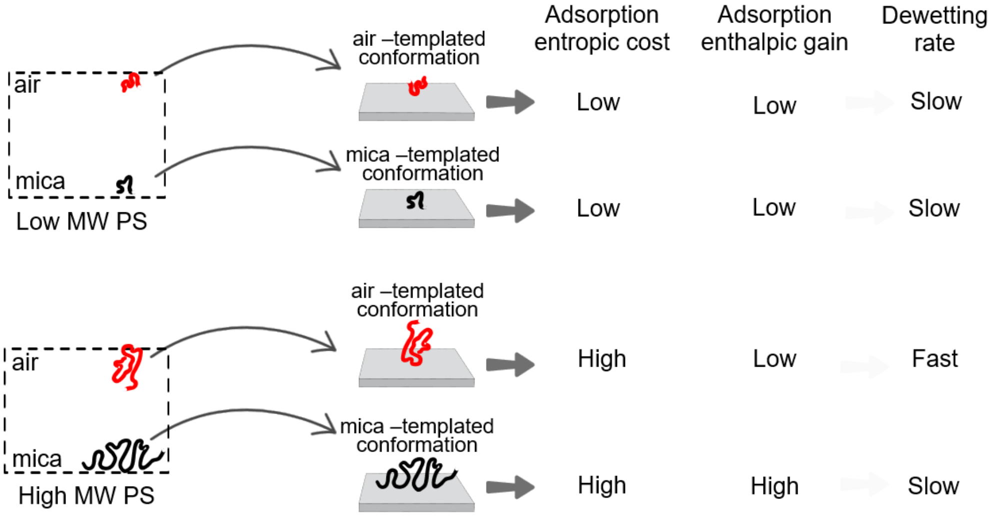

Figure 4.4. Scheme of the relationship between the chain's initial conformation, the adsorption entropy and enthalpy, and the experimental dewetting rate.

4.5.4. Probing PS interfacial chain conformation with SFG spectroscopy

4.5.4.1. Phenyl ring orientation

The orientation of the phenyl groups near the substrate interface may significantly impact the film's dewetting behavior. The type and strength of interactions can vary depending on whether the phenyl groups are aligned parallel to the substrate or adopting an upward position. As a result, it is crucial to consider this factor when investigating the causes behind the observed dewetting rate differences in this study. The details of the SFG analysis of the phenyl ring tilt angles in PS samples are provided in sections B3 and B4 of Appendix B. The range of possible tilt angles for the PS films examined is summarized in Table 4.3.

Table 4.3. Range of possible values of tilt angles for PS films

PS MW (kg/mol)	Interface	Tilt angle range*
27	air-templated	33 ° - 38 °
	mica-templated	33 ° - 36 °
130	air-templated	33 ° - 42 °
	mica-templated	32 ° - 37 °
344	air-templated	26 ° - 35 °
	mica-templated	44 ° - 47 °

* Range corresponds to the overlap between the two methods used for tilt angle analysis (section B3 of Appendix B), considering a narrow tilt angle distribution of 1°.

Despite slight variations in the tilt angle range among the samples, no clear correlation was found between tilt angle and dewetting kinetics. For example, the 344 kg/mol mica-templated interface exhibited the highest tilt angle values, yet its dewetting behavior is expected to be comparable to the 27 kg/mol samples for both interfaces (Figure 4.1 B), which exhibits lower tilt angles. Moreover, although the 344 kg/mol air-templated interface, exhibited the lowest tilt angle and the fastest dewetting rate within this set, the two interfaces of the 130 kg/mol samples also exhibited fast dewetting without having low tilt angles. These results suggest that while the phenyl rings adopt different orientations depending on the interface and molecular weight, these variations are not the primary factor driving the observed differences in dewetting behavior.

It is important to highlight that, although phenyl groups have the potential to form strong interactions with the substrate (as discussed in section 4.5.1.3), these interactions would require significant torsional adjustments in the polymer backbone[11], which hinders efficient multisite adsorption via phenyl ring interactions. Instead, as previously reported for the polystyrene/silver interface[188], despite the phenyl groups having a higher adsorption energy compared to the backbone segments, in high molecular weight samples, the preferred conformation near strongly interacting substrates involves the phenyl rings tilting away from the surface. This orientation facilitates multisite adsorption through the polymer backbone, optimizing the overall enthalpic gain per chain. These findings support our approach in section 4.5.1.3 of calculating the enthalpic gain of adsorption based on backbone interactions rather than phenyl ring interactions, as this configuration maximizes the total energy gain for the polymer chains.

4.5.4.2. End group segregation

One hypothesis proposed by Sabzevari et al.[50] to explain the disparity in dewetting rates among the samples is the segregation of polymer chain ends. This segregation could potentially affect both the type and strength of interactions between the polymer and the substrate, thereby influencing the dewetting rate. It is important to highlight that the molar fraction of chain ends (of nCH_3/nCH_2) per chain is substantially low and it decreases significantly as the molecular weight of the sample increases ($nCH_3/nCH_2 = 2/2N$). Consequently, only a large extent of chain end segregation to the interfacial region would be sufficient to alter the surface chemistry to a degree that affects macroscopic surface properties, such as dewetting.

The comparison between the molar concentration ratio of CH_3 and CH_2 groups and their corresponding SFG amplitude ratio (A_{CH_3}/A_{CH_2}) serves as a useful indicator of the occurrence of surface segregation[3]. If the groups are randomly distributed in the interfacial region and their net orientation remains constant, a positive linear relationship between the molar concentration ratio and the SFG amplitude ratio would be expected. Figure 4.5 presents the values A_{CH_3}/A_{CH_2} as a function of the molar fraction of methyl groups [$nCH_3\ /nCH_2$], for both the symmetric (*ss*) and asymmetric (*as*) stretches. In comparing the two interfaces of the same MW, higher values of A_{CH_3}/A_{CH_2} for both *ss* and *as* stretches are observed at the mica-templated interface compared to the air-templated interface, except for the *ss* stretch of the 344 kg/mol sample. This suggests a greater degree of methyl group segregation at the mica-templated interface, compared to the air-templated interface. Additionally, for the air-templated interface, the negative correlation observed between A_{CH_3}/A_{CH_2} and $nCH_3\ /nCH_2$ indicates a greater degree of end groups segregation as MW increases. However, no direct correlation can be established between chain end segregation and the dewetting behavior of the samples shown in Figure 4.1 B. For instance, the A_{CH_3}/A_{CH_2} ratios differ substantially between the air and mica-templated interfaces for the 27 kg/mol sample, yet these interfaces exhibit similar dewetting behavior. Furthermore, the 130 kg/mol sample shows relatively similar A_{CH_3}/A_{CH_2} ratios at both interfaces but exhibit significantly different dewetting rates.

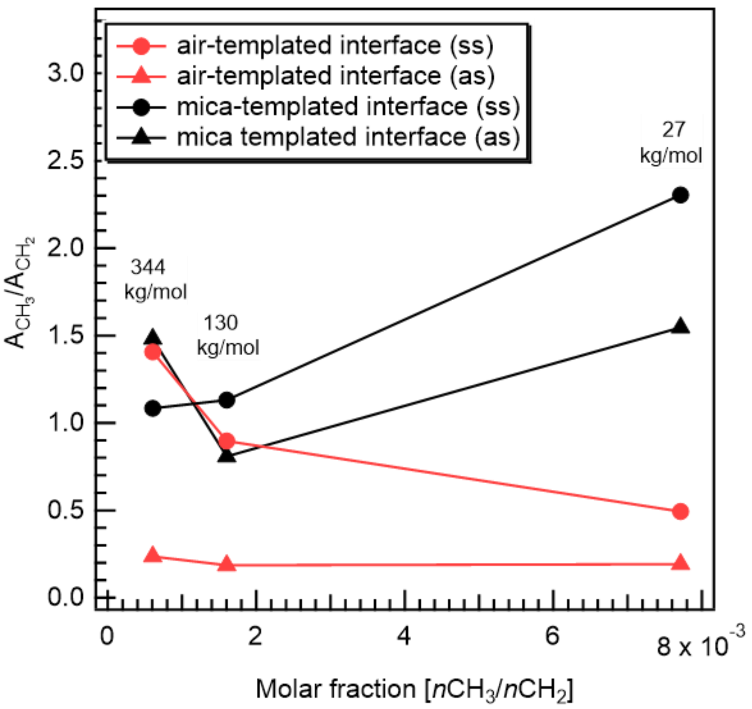

Figure 4.5. A_{CH_3}/A_{CH_2} for the symmetric and asymmetric stretches as a function of the molar fraction of $nCH_3\ /nCH_2$. Here, ss and as are the symmetric and asymmetric stretches, respectively.

4.5.4.3. Backbone conformation

Based on the calculations and hypotheses presented in section 4.5.3, the initial chain conformation (either extended or coiled) is the key factor influencing the disparity in dewetting behavior between the air-templated and mica-templated interfaces of PS samples. To test this hypothesis, we analyzed the backbone conformation of the PS samples using the SFG amplitudes of the CH_2 groups. These amplitudes are influenced by both the interfacial concentration of the methylene groups and their orientation.

When comparing samples of the same composition (e.g. identical PS molecular weight across two interfaces), accounting for orientational differences is relatively straightforward. In ssp polarization, the SFG response of each vibrational mode is proportional to the component of the vibrational dipole aligned with the z-axis, which is perpendicular to the surface. Methylene groups oriented with their symmetry C_2 axis near the surface normal will exhibit strong symmetric stretches and weak asymmetric stretches (Figure 4.6). If the CH_2 orientation shifts to align their symmetry axis more closely with the surface axis, the amplitude of the symmetric stretches will decrease while that of the asymmetric stretches will increase. Figure 4.7 illustrates the amplitudes of the methylene symmetric and asymmetric vibrational modes for the PS films.

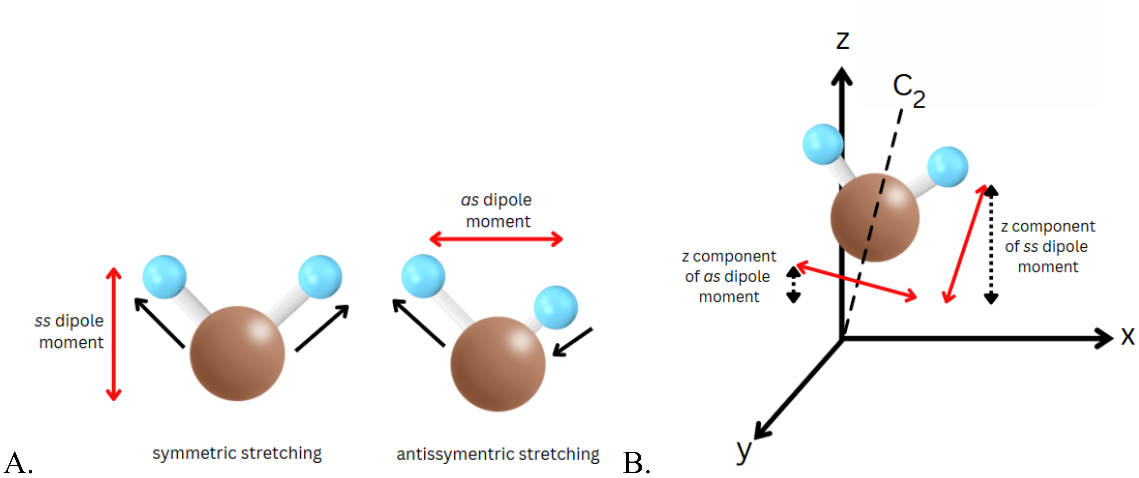

Figure 4.6. A. Scheme of IR transition dipole moment change for CH_2 symmetric and antisymmetric stretches and B. Methylene group oriented with its C_2 axis near the surface normal. The SFG amplitude of each vibrational mode in ssp polarization is proportional to the z component of the IR transition dipole moment change for each mode.

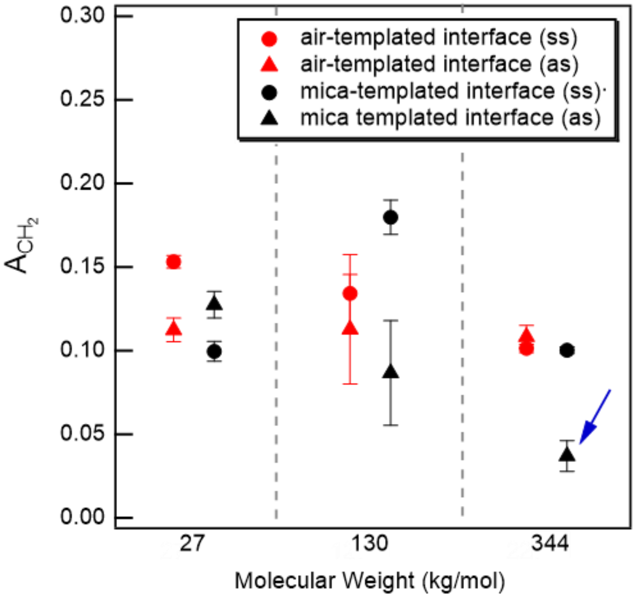

Figure 4.7. SFG amplitudes of the PS backbone methylene groups (ssp polarization).

The *ss* and *as* amplitudes for the 27 kg/mol sample are similar, indicating a similar backbone orientation regardless of the interface. In contrast, for the 130 kg/mol sample, for the mica-templated interface, there is an increase in the *ss* amplitude and a decrease in the *as* amplitude, compared to the air-templated interface. This suggests that, at the mica-templated interface, the methylene groups are preferentially oriented with their symmetric axis closer to the surface normal compared to the air-templated samples. This shift of backbone methylene orientations towards the surface normal was previously linked to the occurrence of polymer chain extension, with the chain axis lying at the surface plane[197]. The extension of the atactic PS chains also result in a substantial increase in the number of *trans* configurations[197]. This increase in the number of *trans* configurations of the methylene groups may alter the local concentration of methylene groups in contact with the surface, and it may also lead to SFG signal cancellation through destructive interference, thereby significantly reducing the SFG amplitude of this vibrational mode.

The 344 kg/mol sample exhibits a substantial decrease in the *as* amplitude at the mica-templated interface (highlighted by the blue arrow), compared to the air-templated interface (Figure 4.7) which is not accompanied by an increase in the *ss* amplitude, which rules out the possibility of a simple change of the methylene tilt angle. One possible explanation for this drastic decrease in the *as* amplitude is the extension of the PS backbone parallel to the surface, increasing the number of *trans* configurations, as observed in other polymeric systems[3].

The SFG analysis of the PS samples thus aligns with the theoretical considerations discussed in section 4.5.3, supporting the occurrence of chain extension in the 344 kg/mol sample at the mica-templated interface. Additionally, these findings provide insight into the dewetting behavior of the 130 kg/mol sample, which shows the fastest dewetting rate at the mica-templated interface compared to the other mica-templated samples (Figure 4.1 B). For this sample, it is possible to see that there is some level of rearrangement of the chain backbone towards extension, when comparing the air-templated interface to the mica-templated interface, in terms of the methylene groups tilting towards the surface normal. These chain level conformational difference results in a slower dewetting rate for the mica-templated interface relative to the air-templated one. However, the backbone is not yet substantially extended, indicated by no observed chance in the number of *trans* configurations, unlike the 344 kg/mol sample which shows both increased number of trans configuration and the tilting of the methylene groups towards surface normal. This intermediate conformation, between random coil and extended conformation, explains why the 130 kg/mol sample has a higher dewetting rate at the mica-templated interface compared to the 344 kg/mol sample, but still lower dewetting rate than the 130 kg/mol air-templated interface.

4.6. Conclusion

Polystyrene thin film samples exhibiting differences in dewetting behavior were analyzed through both theoretical calculations and SFG spectroscopy to explore the relationship between interfacial chain conformation and dewetting dynamics. Theoretical analysis of the entropic and enthalpic forces governing polymer chain adsorption revealed that PS films annealed while deposited on a highly interacting substrate like mica, and exposed to air at the opposite interface, develop significantly different chain conformations at each interface. These interfaces exhibit a templating effect of the polymer chains conformation with a coiled conformation being expected near the air-templated interface, and an extended chain conformation being expected near the mica-templated interface. Moreover, the extent of chain extension near the mica-templated interface was found to depend on the PS MW, with higher MW leading to a greater degree of chain extension. The analysis also suggested that when these templated interfaces are transferred to a weakly adsorbing substrate, dewetting will occur, as the entropic cost of adsorption outweighs the adsorption enthalpic gain. However, the results showed that the initial chain conformation directly impact the dewetting kinetics of the thin films: initially extended chains display lower dewetting rates compared to coiled chains, due to a higher number of polymer-substrate interactions, despite the increased entropic cost of adsorption.

The theoretical results were validated by the SFG spectroscopy analysis of the chains interfacial conformation. Firstly, the SFG orientational analysis showed no correlation between the dewetting rate of the PS thin films and either the phenyl ring tilt angle or the chain end segregation. Secondly, the observed trends in the amplitudes of the backbone methylene groups indicated the extension of the PS chain backbone in high molecular weight PS samples, consistent with the predictions of the theoretical model.

This study revealed that variations in initial chain conformations alone are sufficient to explain the observed disparities in dewetting rates across different PS samples. The results highlight the critical role of the polymer film thermal and mechanical history in determining the molecular-level organization of the polymer chains, as well as the macroscale behavior of the film, such as dewetting. Beyond dewetting, the findings have broader implications for understanding the slip behavior and rheological properties of thin polymer films. Since interfacial chain conformation plays a key role in modulating the number of chain-substrate interactions, it directly influences slip at the interface, which in turn affects the film's flow properties. These insights are critical for applications requiring precise control over the mechanical and rheological properties of thin films, such as in coatings, microelectronics, and biomedical applications.

Chapter 5 . Lamellar orientation at the surface of isotactic polystyrene thin films analyzed by sum frequency generation spectroscopy

5.1. Preface

This chapter was previously published as: https://doi.org/10.1016/j.aca.2023.340904

"Lamellar orientation at the surface of isotactic polystyrene thin films analyzed by sum frequency generation spectroscopy" Bianca Martins de Lima, Patrick Hayes, and Paula Wood-Adams, (2023). *Analytica Chimica Acta*, 1248, 340904.

Previously, we demonstrated that SFG spectroscopy is a powerful technique for analyzing the conformation of polymer chains at different interfaces, offering valuable insights into how interfacial conformations influence the macroscopic properties of polymer films. In this chapter, we explore the pioneering use of SFG spectroscopy in the analysis of the surface lamellar orientation in semi-crystalline polymeric thin films. Through the combination of the SFG orientation analysis and the theoretical analysis of the expected SFG response of each possible lamellar orientation, we have successfully determined a flat-on lamellar orientation at the surface of iPS films, with the chain axes having perpendicular orientation relative to the substrate. Furthermore, this finding was confirmed by AFM studies.

Moreover, we reported the evolution of SFG spectral features during the progress of iPS crystallization. The intensity ratios of phenyl ring resonances can be used as markers for assessing the degree of surface crystallinity. Furthermore, we report the challenges associated with SFG measurements on heterogeneous surfaces, which is the case of most semi-crystalline polymer films.

This work represents a novel application of SFG spectroscopy to investigate the lamellar orientation of semi-crystalline polymer surfaces. It also pioneers the use of SFG for evaluating surface conformations in both semi-crystalline and amorphous iPS thin films, linking spectral intensity ratios to crystallization dynamics and surface structure.

The findings emphasize the versatility of SFG spectroscopy as a valuable technique for studying polymeric crystalline structures at interfaces. This approach opens avenues for examining more complex polymer systems and crystalline configurations, especially in cases where traditional imaging methods like AFM are not applicable, such as buried interfaces.

Minor adjustments, including the numbering of figures, tables, and references, were made to ensure consistency with the rest of the thesis. Since the following manuscript is presented in its entirety, there may be some overlap with other sections of the thesis, such as repeated descriptions of abbreviations and equations.

5.2. Abstract

Analyzing the orientation of polymeric crystalline lamella at the surface of thin films can be challenging. Even though atomic force microscopy (AFM) is often sufficient for this analysis, there are cases when imaging is not sufficient to confidently determine lamellar orientation. Here, we used sum frequency generation spectroscopy (SFG) to analyze the lamellar orientation at the surface of semi-crystalline isotactic polystyrene (iPS) thin films. The SFG orientation analysis indicated that the iPS chains are oriented perpendicular to the substrate (flat-on lamellar orientation), which was confirmed by AFM. By analyzing the evolution of the SFG spectral features with the progress of crystallization, we demonstrated that the ratios of the SFG intensities of the phenyl ring resonances are a good indication of the surface crystallinity. Furthermore, we explored the challenges associated with SFG measurements of heterogeneous surfaces, which is commonly present in many semi-crystalline polymeric films. To the best of our knowledge, this is the first time that the surface lamellar orientation of semi-crystalline polymeric thin films was determined by SFG. Also, this work pioneers in reporting the surface conformation of semi-crystalline and amorphous iPS thin films by SFG and in linking the SFG intensity ratios to the progress of the crystallization and the surface crystallinity. This study demonstrates the potential applicability of SFG spectroscopy in the conformational analysis of polymeric crystalline structures at interfaces and opens the way to the investigation of more complex polymeric structures and crystalline arrangements, especially for the case of buried interfaces, where AFM imaging is not an option.

5.3. Introduction

Semi-crystalline polymeric thin films with outstanding thermal[198], mechanical[199] and opto-electrical[200] properties have been used for high performance applications, such as transistors[201–204], sensors[205–207] and membranes[208,209]. In such systems, the isotropic spherulitic growth is hindered due to confinement effects[210–212] and the crystalline lamellae can grow with chains having a parallel or perpendicular orientation with respect to the substrate surface, the so-called edge-on and flat-on orientations, respectively[59]. Changes to the lamellae orientation of thin films can greatly affect their properties and application performance[213–215], therefore, it is crucial to optimize the film fabrication methods, as well as the characterization strategies for this class of materials.

The surface of thin films plays an important role in the interaction of the films with their surroundings, and they may act as barriers[216], adhesion interfaces[217], as well as adsorption sites[218]. Several conditions contribute to the formation of different crystalline structures for a given system, such as the crystallization temperature[219,220], the film thickness[221] and the polymer/substrate interactions[222]. Therefore, the understanding of the crystalline structure of the film surface is critical to tailor and to optimize the film's performance for each application.

The analysis of the lamellar orientation of polymeric thin films usually relies on using X-ray scattering, atomic force microscopy (AFM), transmission electron microscopy (TEM) and electron diffraction (ED)[210,212,223–225]. Among these methods, AFM is surface specific, while the others provide the lamellar orientation information throughout the film thickness. Determining the surface lamellar orientation using AFM is usually a straightforward process, because significant differences in the surface topography[226] often occur for edge-on or flat-on spherulitic orientations, with the first appearing as a fibril-like surface, and the latter as terraces[94,220]. However, sometimes, it is challenging to make this determination only based on the AFM images, and other methods to confirm the lamella orientation become necessary[210,224]. Additionally, AFM is only applicable to free surfaces and other approaches are needed for buried interfaces.

Sum frequency generation (SFG) spectroscopy is a second-order, non-linear analytical technique useful for the analysis of molecular conformations at surfaces and buried interface [12,14,111]. Previous studies have highlighted the applicability of SFG in the analysis of semi-crystalline polymers[77,227–229]. Recently, Kawaguchi et al.[229] observed changes in the SFG spectra of isotactic polypropylene due to changes in the lamellar orientation, with significant contribution of the crystals in the interior of the films. Subsequently, Abe et al.[77] used SFG microscopic imaging to perform chemical mapping of semi-crystalline polymeric films, demonstrating that the SFG imaging could differentiate isotactic polypropylene from uniaxially oriented poly(vinylidene fluoride) (PVDF) due to differences in the lamellar orientation, reflected in the SFG images.

However, this study relied on grazing-incidence wide-angle X-ray diffraction to determine lamellar orientation. The forementioned studies highlight the potential of using SFG to study chain conformation in semi-crystalline polymeric thin films and the importance of developing new methods to support the orientation analysis of the crystalline lamella in polymeric thin films. However, there is lack of studies exploring the use of SFG to determine the lamellar orientation at the surface of polymeric thin films.

In the present work, we demonstrate that SFG can be used to determine the lamellar orientation of the surface crystals of isotactic polystyrene (iPS) thin films. This polymer was chosen as model molecule because it is a slow crystallizer[230], allowing the production of fully amorphous films and the monitoring of the crystallization process at different stages. Furthermore, its amorphous isomer, atactic polystyrene (aPS) is widely studied by SFG, facilitating the spectra interpretation[5,10,13,19,188]. However, to the best of our knowledge, this is the first time that the surface structure of amorphous and semi-crystalline iPS are studied by SFG spectroscopy.

5.4. Experimental section

5.4.1. Sample preparation

The iPS samples were obtained from Polymer Source, Inc. and used as received. The iso content of the sample is > 90%, as indicated by the supplier. The weight average molecular weight (Mw) and the polydispersity index (PDI) were 216,600 g mol^{-1} and 3.46, respectively, analyzed by gel permeation chromatography (performed by the supplier, at 30 °C, using an Agilent Technologies 1260 Infinity II GPC/SEC System equipped with a triple detector and tetrahydrofuran as the mobile phase).

The iPS powder was placed in an oven at 240 °C under nitrogen atmosphere for ten minutes (melting temperature, Tm, 223 °C) and then quenched using an ice bath to produce an amorphous sample, enabling the following solubilization. Solutions of iPS in toluene 1% w/w were prepared and then filtered using poly(tetrafluoroethylene) (PTFE) filters from Fisher Scientific (pore size 0.45 μm) to remove possible insolubilized crystals.

Thin films of iPS of 100 nm were produced by spin coating (2000 rpm) freshly filtered iPS solutions onto fused silica optical windows (IR grade, ISP Optics Corp.). The optical windows were previously cleaned with hot piranha solution (80 °C, 3:1 H_2SO_4/30 vol % H_2O_2) for 1 h, followed by abundant washing with HPLC grade water (Sigma Aldrich) until neutral pH was measured at the edge of the window using pH test strips. The films were dried under vacuum for 48 h in a desiccator containing silica gel desiccant beads. To measure the thicknesses of the films, thin films were deposited on glass slides, using the same conditions mentioned above. A gentle scratch was made at the center of the films, to expose a region without polymer. Then, the thicknesses of the films were determined using a profiler (DEKTAK 150).

Amorphous films of iPS were made by placing the dried films in an oven at 240 °C under nitrogen atmosphere for 10 minutes, followed by quenching using an ice bath while avoiding any contact between the polymer and the water. This step allowed the iPS chains to relax the conformation forced by the spin coating and to melt any crystals not removed during filtration or formed during the film deposition. Similar procedures for producing amorphous films of iPS are reported in the literature[231,232]. Semi-crystalline films of iPS were made by submitting the amorphous films to isothermal crystallization at 180 °C under nitrogen atmosphere for fixed period of times (2.5 h, 5 h, 10 h and 16 h). The semi-crystalline films were named with respect to the isothermal crystallization time (e.g. 16 h film refers to the film crystallized for 16 h). The progress of the crystallization and the microstructure were analyzed by optical microscopy (Fein Optic, M50RT Metallurgical Reflected/Transmitted Brightfield/Darkfield Microscope). Furthermore, the surface topography was analyzed by atomic force microscopy (AFM, Tosca 400 by Anton Paar, tapping mode). The imaging results were used to validate the lamella orientation obtained by SFG. A summary of the study methodology is presented in Figure 5.1.

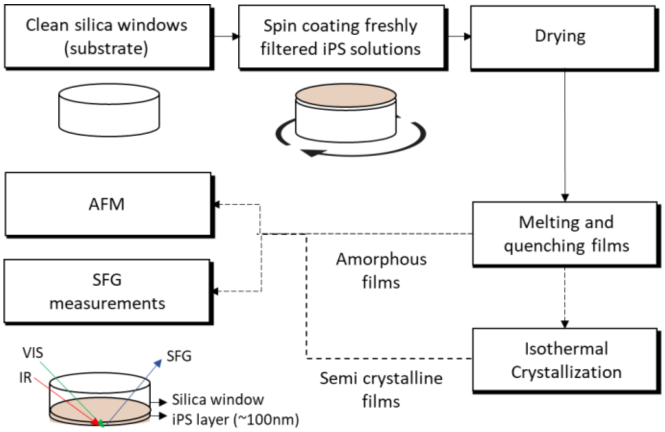

Figure 5.1. Scheme of methodology used in the study

5.4.2. SFG measurements

Details regarding our SFG system (EKSPLA) are provided elsewhere[5,135]. Briefly, the instrument is comprised of a Nd:YAG laser (PL2241 series), an optical parametric generator (PG501/DFG) and a monochromator (MS2001). The laser generates a fundamental 1064 nm beam and a 532 nm visible beam. Then, a tunable IR beam is generated by the optical parametric generator. The visible and infrared beam overlap at the film's surface and generate the SFG beam. Lastly, the SFG signal is analyzed by the monochromator.

The SFG spectra were collected in ssp, ppp and spp polarizations, where the three letters indicate the polarization of the SFG beam, visible beam, and IR beam, respectively. To account for changes in laser power, the SFG signal was normalized by the product of the visible and IR energies[5,188]. Furthermore, the frequency was calibrated by using a spectra of poly(methyl methacrylate) (PMMA) that exhibits an intense resonance at 2955 cm^{-1}.

At least five film specimens per crystallization time were produced and analyzed. To compare the SFG intensity ratios of the phenyl ring vibrational modes, 24 to 52 ssp spectra, each collected from a different location on the sample, were used per crystallization time. A larger number of spectra were collected for the intermediate crystallization times (2.5 h, 5 h and 10 h), to account for the surface heterogeneity, as discussed in section 5.5.3.

The samples were analyzed with the incident beams passing through the optical window and the iPS film and overlapping at the iPS/air interface (Figure 5.1). Considering the sample geometry used in the present study, the two interfaces present (iPS/silica and iPS/air) could generate SFG signal because of the broken inversion symmetry. Also, the bulk region of semi-crystalline polymers may be SFG active[228,233]. The influence of the signal coming from the iPS/silica interface is considered negligible, because it is expected to be one order of magnitude smaller than that of the free surface[8]. An additional sample was prepared by coating the 16 h film surface with a thin layer of PMMA. To demonstrate that the origin of the SFG signal in the present study was from the film free surface (iPS/air) and to determine if a SFG signal was also coming from the bulk crystals, the 16 h film surface was coated with a thin layer of PMMA and the ssp spectrum was collected. The PMMA coating was made by spin coating (2000 RPM) a 0.5% w/w PMMA solution in nitromethane, which does not dissolve iPS, on top of the 16 h film. As the coated sample does not have the iPS/air interface, a substantial decrease in the SFG intensity, comparing with the 16 h sample without the top coating, demonstrates that the iPS/air interface is the predominant source of SFG signal from the iPS samples of the present study. Furthermore, we collected the spp spectra of the amorphous and 16 h films, because spp polarization is not surface active in SFG and may be considered a characteristic ‘’bulk” spectra[228].

5.4.3. SFG orientation analysis

The SFG spectra were collected from 2800 cm^{-1} to 3100 cm^{-1}, to include the resonances from the phenyl ring and backbone of iPS. The vast majority of previous IR spectroscopic studies of the crystallization of iPS[230,234–240] have focused the discussion of the spectra in the frequency region between 500 cm^{-1} to 1500 cm^{-1}. This is because this region includes the IR vibrational modes that are most sensitive to crystallization, such as the mode at 981 cm^{-1}, which is associated with the ordering of the phenyl rings and increases in intensity with crystallization, and the mode at 840 cm^{-1}, which decreases in intensity with crystallization and is linked to the amorphous phase of iPS[239]. These frequencies are usually out of the range of operation of commercially available SFG spectrometers, which poses not only a challenge for the interpretation of the iPS SFG spectra with crystallization, but also represents an opportunity to explore iPS crystallization by spectroscopy within a different region of the IR spectra.

The vibrational modes of the phenyl ring of iPS, ν_{20b}, ν_{7a}, ν_{7b} and ν_2 (Figure 5.2 A), were assigned the resonances present at ~3027 cm^{-1}, ~3038 cm^{-1}, ~3056 cm^{-1} and ~3072 cm^{-1}, respectively[6,7,13]. Also, the vibrational modes of the iPS backbone, CH_2ss, CH_3ss, CH and CH_2as were assigned to the resonances present at ~2850 cm^{-1}, ~2877 cm^{-1}, ~2906 cm^{-1} and ~2923 cm^{-1}, respectively, in agreement with previous studies[10,19,105], where ‘’ss” and ‘’as” represent the symmetric and antisymmetric stretch.

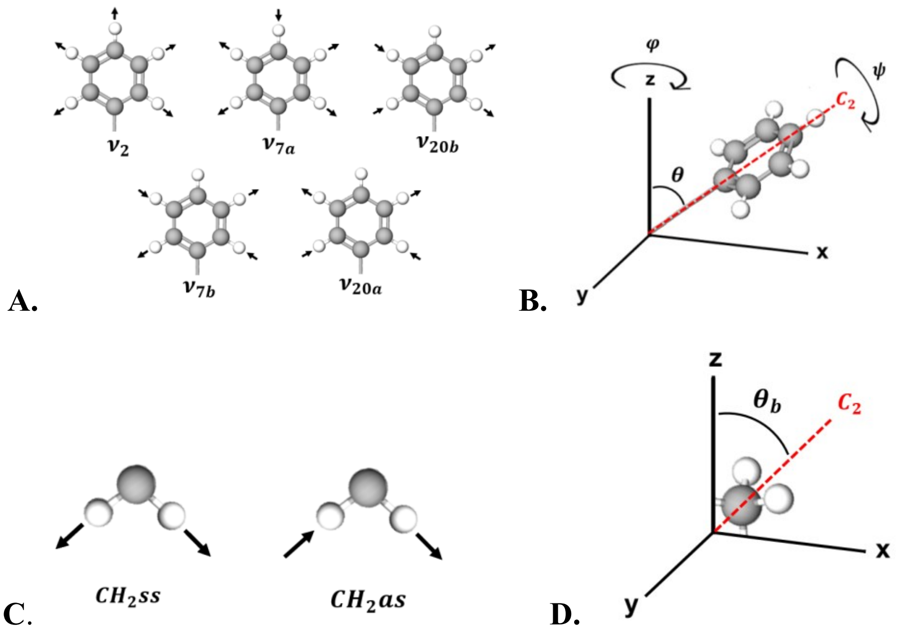

Figure 5.2. A. C-H stretch vibrational modes of iPS phenyl ring. B. Phenyl ring Euler angles, tilt angle of iPS phenyl ring (θ), twist (ψ) and the azimuthal (φ) angles. C. C-H stretch vibrational modes of CH_2. d. Tilt angle of iPS backbone CH_2 groups (θ_b).

The orientation of the pendant phenyl ring in iPS is described in terms of the Euler angles, namely the tilt (θ), the twist (ψ) and the azimuthal (φ) angles (Figure 5.2 B). In the orientation analysis, we consider the twist and azimuthal angles as isotropically distributed. This assumption is based on the fact that the samples were annealed above the melting temperature prior to crystallization, which removes any possible net orientation of the phenyl rings in the x-y plane (surface plane), leading to isotropic φ distribution. Furthermore, the spherulites formed during crystallization also lead to an isotropic φ distribution. The phenyl rings at the vicinity of the air interface can rotate around the C_2 axis (single C-C bond), leading to isotropic ψ distribution. A non-isotropic φ distribution usually involves high energy interactions (for example, between the phenyl rings and the substrate) that overcome the torsion barrier of the ring with respect to the chain[11].

The SFG spectra of the films were used for analyzing the tilt angle of the pendant phenyl ring (θ) and of the CH_2 groups (θ_b), defined as the angle between the C_2 symmetry axis of these groups and the surface normal (Figure 5.2 B and D). For the orientation analysis, the five specimens of the amorphous and 16 h films were used. For each specimen, at least 3 ssp and 3 ppp spectra were collected in different spots from the specimen on the same day. The triplicate ssp and ppp spectra collected for each specimen were then averaged for the following fitting performed with Igor Pro 8 software (WaveMetrics). The average spectra were fitted using a Lorentzian function[14,111,137] (Equation 5.1), that relates the SFG intensity (I_{SFG}) to the square of the effective second-order non-linear susceptibility tensor (χ_{eff}). In Equation 5.1, χ_{NR} and α are the non-resonant signal and its phase, respectively, A_q is the amplitude of the vibrational mode q, ω_{IR} and ω_q are the IR beam frequency and the frequency of the resonant vibrational mode q, respectively, and Γ_q is a damping constant. To maximize the accuracy of the fitting parameters, the fitting using Equation 5.1 was performed separately for the phenyl ring and backbone vibrational frequencies of the spectra. The fitting parameters were then averaged for all specimens.

$$I_{SFG} \propto \left|\chi_{eff}\right|^2 = \left|\chi_{NR} e^{i\alpha} + \sum_q \frac{A_q}{\omega_{IR} - \omega_q + i\Gamma_q}\right|^2 \qquad \text{Equation 5.1}$$

We used two different strategies to estimate the tilt angle of the iPS pendant phenyl ring. First, θ can be estimated by the ratio between ν_2 amplitudes in ssp and ppp polarizations (method 1, Equation C1), according to the work of Lu and co-workers[7]. Another way to estimate the phenyl ring tilt angle is based on the ratio between the amplitudes of the ν_{20b} and ν_2 vibrational modes in ssp polarization (method 2, Equation C2)[10,13,141]. Here, we have used the parameters values reported by Hong and co-workers[6].

5.5. Results and discussion

5.5.1. Crystal growth

The growth of iPS crystals was monitored by optical microscopy. The images are presented in Figure 5.3. No crystalline features were observed for the films after the melting and quenching processes, confirming the applicability of this methodology to produce a fully amorphous sample. At 2.5 h, the presence of iPS spherulites of diameter 71 ± 1 µm distributed throughout an amorphous matrix can be observed. The spherulitic diameter grows with the crystallization time and impingement can be observed starting at 10 h. At 16 h, the surface of the film is mostly crystalline with large spherulites (diameter of 455 ± 9 µm). The average linear spherulitic growth rate was 14.1 ± 0.1 µm h^{-1}, which is comparable to the value reported by Sawamura et al.[220] for 100 nm thick iPS films deposited on glass and crystallized at 180 °C (16 µm h^{-1}). The surface crystallinity, in terms of area fraction, was estimated from the optical microscopy images to be about 8 %, 18 %, 51 % and 89 %, for 2.5 h, 5 h, 10 h and 16 h, respectively.

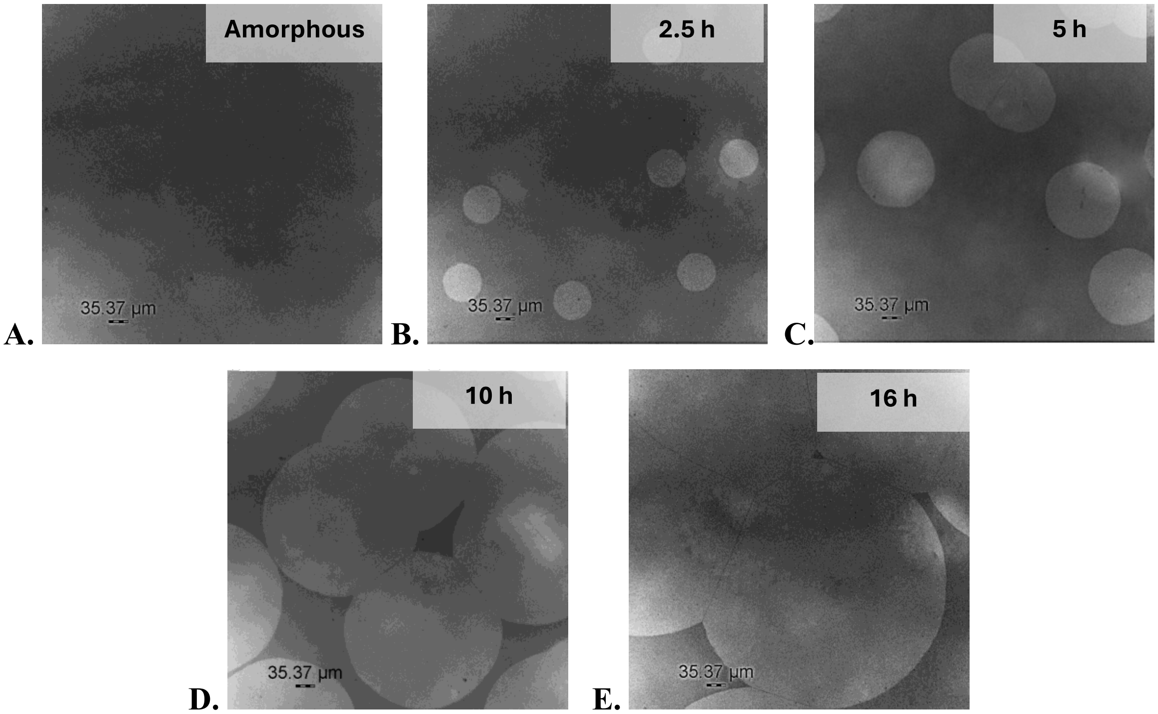

Figure 5.3. Optical microscopy images of the iPS films that are: A. amorphous and crystallized at 180 °C for B. 2.5 h, C. 5 h, D.10 h and E.16 h.

5.5.2. Confirming the source of the SFG signal

The SFG selection rules state that this process can only occur if the media symmetry does not have an inversion center. As a result, SFG is generally considered to be specific for the polymer/air or polymer/substrate interface of thin films, because for most amorphous polymeric films, the ensemble averaged bulk region has inversion symmetry. In these materials, the inversion symmetry is only broken at the interfaces, and therefore, only the interfaces are SFG active. However, for crystalline materials, there is the possibility of SFG activity from the bulk, when the crystals are non-centrosymmetric[228,233], or when there is a large difference in the refractive indices of the amorphous and crystalline phases[77,229]. To test the bulk SFG activity in the present work, we compared the SFG spectra of the amorphous and 16 h crystalline iPS films collected in spp polarization (Figure 5.4 A). This polarization combination was previously reported to generate distinguishable resonances for a polymer sample with a SFG active bulk[228]. The spp spectra of the amorphous and 16 h films are very similar, with no significant differences in the SFG intensities or new features, indicating a lack of SFG activity from the bulk of iPS semi-crystalline films.

The SFG signal arising from each interface of the sample can be expressed in terms of their contribution to χ_{eff}, as shown in Equation 5.2[63]. In Equation 5.2, $F^{silica/iPS}$ and $F^{iPS/air}$ are the Fresnel coefficients of the silica/iPS and iPS/air interfaces, respectively. Also, $\chi^{silica/iPS}$ and $\chi^{iPS/air}$ are the second-order non-linear susceptibility tensors for the silica/iPS and iPS/air interfaces.

$$\chi_{eff} = F^{silica/iPS}\chi^{silica/iPS} + F^{iPS/air}\chi^{iPS/air} + \chi_{NR} \qquad \text{Equation 5.2}$$

We used a thin film interference model[63,112] presented in Appendix C. Briefly, the magnitude of the Fresnel coefficients are 10 times stronger for the iPS/air interface than for the silica/iPS interface in ssp polarization. Furthermore, for ppp polarization, all components of the Fresnel coefficients are 1.5 to 6 times stronger for the iPS/air interface, compared to the silica/iPS interface. The SFG intensity has a quadratic dependence on χ_{eff} (Equation 5.1). Therefore, stronger Fresnel coefficients for the iPS/air interface represent a substantial magnification of the resonant SFG signal coming from this interface.

To further confirm that the film surface (iPS/air) was the main source of SFG signal, with negligible contribution from the iPS/silica interface and from the bulk crystals, the 16 h sample was coated with a thin layer of PMMA. The ssp spectrum collected in this configuration, as well as the spectrum of the 16 h film with no top coating, are shown in Figure 5.4 B. The feature observed at ~2955 cm^{-1} in the coated sample belongs to the PMMA. The pure PMMA SFG spectra contains no features between 2980 cm^{-1} - 3100 cm^{-1} as shown in Figure 5.4 C. We observe that, when the film's surface is coated with PMMA, the SFG signal in the phenyl ring region decreases to about 1/3 of its initial value. Furthermore, coating the film surface resulted on a shift of the ν_2 vibrational frequency from ~3070 cm^{-1} to ~3060 cm^{-1}. These observations are consistent with the work of Curtis, et al.[13], where the authors compared the SFG spectrum of the surface of atactic polystyrene films, with the one in which the surface was coated with PMMA. These results indicate that the main source of the SFG signal in the present study is the film surface, with negligible interference from the bulk or from the iPS/silica interface.

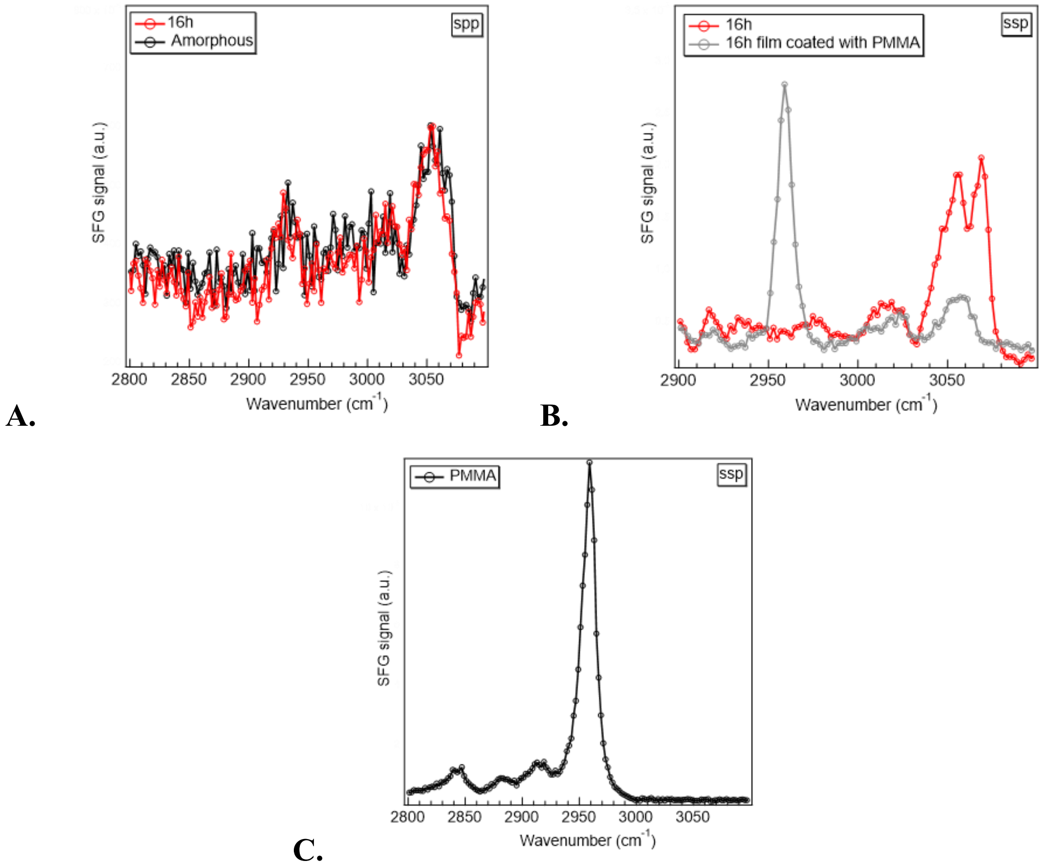

Figure 5.4. A. SFG spectra of the amorphous and 16 h semi-crystalline iPS films collected in spp polarization. B. SFG spectra of the 16 h iPS film with and without the top surface coated with a thin layer of PMMA (ssp polarization). C. PMMA SFG spectrum in ssp polarization, showing the absence of features from 3000 cm^{-1} to 3100 cm^{-1}.

5.5.3. Tracking the crystallization progress by SFG

Before performing the surface orientation analysis of the iPS films, it is important to know the changes in the SFG spectral features with the progress of the crystallization. The surface SFG spectra of iPS was previously reported by Oh-e and co-workers[241]. However, the spectra reported by the authors are of a rubbed iPS surface (annealed at 170 °C for 1 h), making it impossible to directly compare with the spectra collected in the present study. Also, the authors did not explore the effect of the crystallization on the iPS SFG spectra.

Previous authors have reported drastic changes in the SFG spectra with crystallization of different substances. For example, Zhang and co-authors monitored the freezing temperature of water at different interfaces by looking at the temperature at which there was a sudden increase of the SFG intensity at ~3100 cm^{-1}, which is associated with tetrahedrally coordinated hydrogen-bond stretch, only present in ice[242]. Also, Johnson, et al. observed the appearance an intense new spectral feature at ~3007 cm^{-1} when comparing the SFG spectra of amorphous and semi-crystalline PLA films[228]. Contrastingly, only subtle SFG spectral changes are observed during iPS crystallization, which is consistent with the IR and Raman behavior of iPS with crystallization[243]. When the SFG spectrum of the amorphous film is compared to that of the 2.5 h film (Figure 5.5 A), which already contains several spherulites (Figure 5.3 B), we observe only a small decrease in the ν_2 intensity, with the other spectral features remaining nearly unchanged. Even when comparing the SFG spectra of the amorphous films with the 16 h iPS films (Figure 5.5 B), which have the surface dominated by crystals, we observe no new features emerging in the spectra. Still, in the phenyl ring frequency region (3000 cm^{-1} to 3100 cm^{-1}), we observe changes in the relative intensities of the vibrational modes, as explained in the following paragraphs. Furthermore, in the backbone frequency region (2980 cm^{-1} to 3000 cm^{-1}), it is possible to observe that the resonances of the 16 h films are better resolved than the ones of the amorphous films. For example, the CH_2ss and the CH_3ss resonances are merged in the SFG spectra of the amorphous films, while they are completely separated in the SFG spectra of the 16 h films. The same happens with the CH and the CH_2as resonances. This observation indicates that the level of ordering[14] of the backbone groups at the surface is higher for the 16 h sample, compared to the amorphous samples, which is consistent with the backbone ordering that occurs during the helix formation of crystallization. Furthermore, the lower level of ordering seen for the amorphous iPS film surface is expected, as it maximizes the conformational entropy of the surface chains.

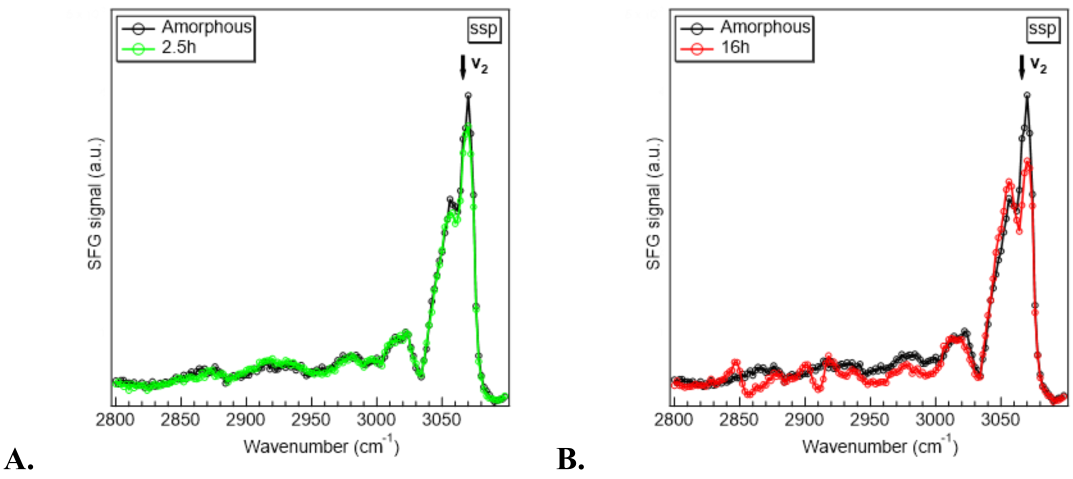

Figure 5.5. A. SFG spectra of iPS amorphous films and 2.5 h semi-crystalline films. B. SFG spectra of iPS amorphous films and 16 h semi-crystalline films. All spectra are in ssp polarization.

The use of SFG in the analysis of chain conformation in semi-crystalline systems raises a few challenges that are not present in amorphous systems. For example, the heterogeneity of the sample surface may lead to lack of repeatability in the SFG spectra. Figure 5.6 A shows various spectra collected for a single 5 h film specimen, at different spots. It is possible to see that, the spectra labeled as #1 is significantly different than the others, and that the relative amplitudes of the ν_{7b} and ν_2 modes resemble the ones observed for the 16 h sample (Figure 5.6 B). This probably happened because spot #1, which was chosen randomly, was richer in crystalline features than the other spots. Similar behavior was seen for the other intermediate crystallization times. It is important to mention that the orientation analysis of the films at intermediate crystallization times (2.5 h, 5 h and 10 h) is challenging and goes beyond the scope of the present work, because there exist two populations of chains with different conformations, and they may be probed simultaneously by the SFG beam. A deeper discussion of the SFG spectra differences due to heterogeneous film surfaces is presented in section C2 of Appendix C.

Despite the intrinsic challenges associated with the SFG analysis of heterogeneous surfaces, we observe that the intensity of the ν_2 mode decreases progressively as crystallization advances (Figure 5.6 B). Also, we demonstrate that the SFG spectra provides an indication of the surface crystallinity. By simply calculating the ratios of the SFG intensities of the phenyl ring vibrational modes, it is possible to clearly distinguish the samples with lower surface crystallinity (amorphous and 2.5 h) from the ones with higher surface crystallinity (5 h, 10 h and 16 h), as shown in Figure 5.6 C and D for the SFG intensities ratios of ν_{20b}/ν_2 and ν_{7b}/ν_2, respectively.

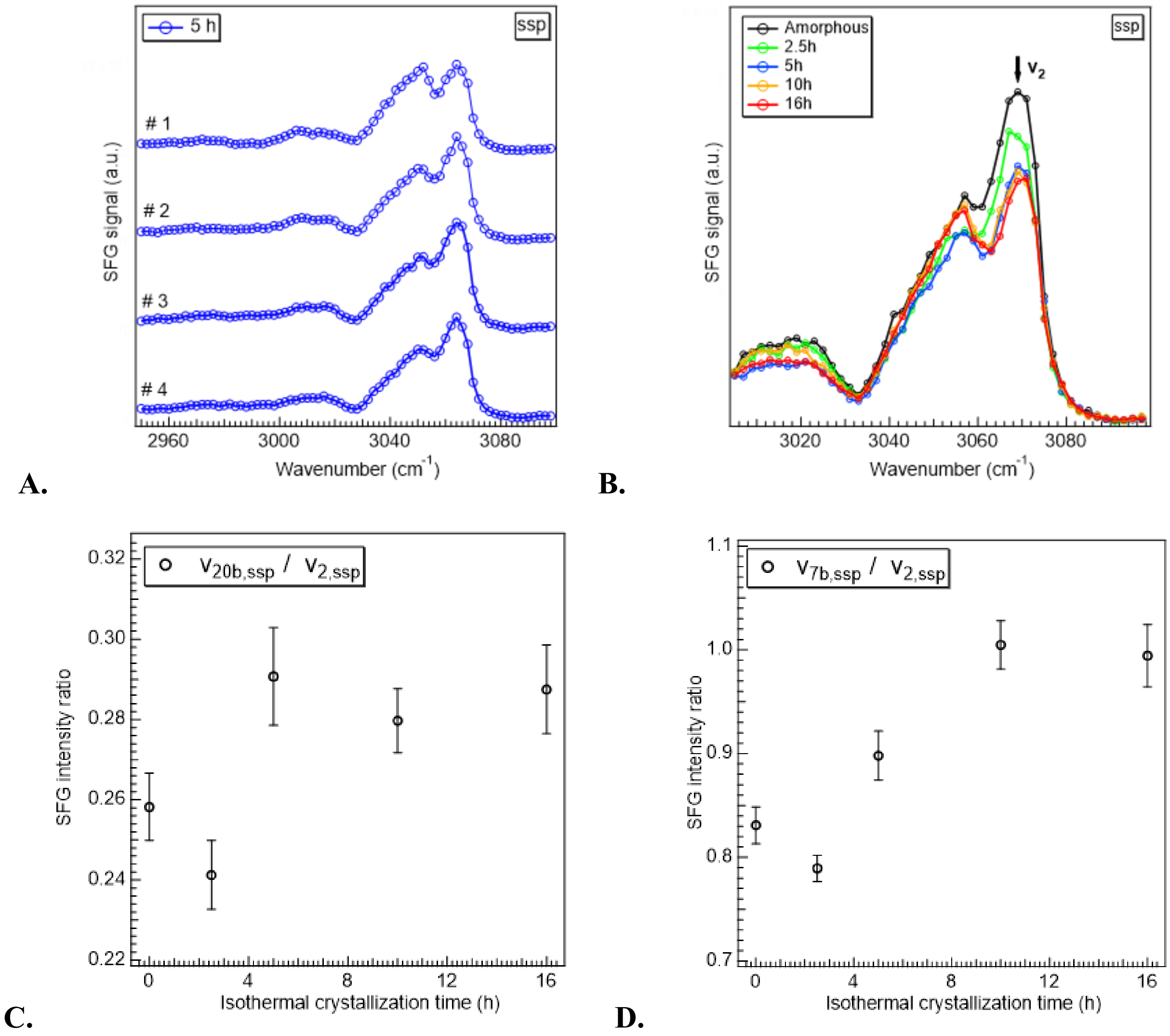

Figure 5.6. A. SFG spectra of a 5 h film, the curves are multiple spectra taken from different spots (curve numbers) of one specimen, in a single day. B. SFG spectra of iPS amorphous films and crystallized at 180 °C for 2.5 h, 5 h, 10 h and 16 h. C. Ratio of the SFG intensity ν_{20b}/ν_2 as a function of crystallization time (ssp polarization). D. Ratio of the SFG intensity ν_{7b}/ν_2 as a function of crystallization time (ssp polarization). Here, we note that, to account for the surface heterogeneity, the intensity ratios are based on the average of 24 to 52 spectra per crystallization time. Error bars represent the standard error.

5.5.4. Crystalline structure of iPS and expected SFG response

The crystalline structure of iPS was described by Natta and Bassi[244]. The 3_1 helix of iPS in thin films may be oriented parallel or perpendicular to the surface normal, resulting in a flat-on or edge-on lamella orientation, respectively (Figure 5.7). Our goal is to use the SFG conformation analysis to determine the lamellar orientation of the surface crystals of the iPS thin films crystallized at 180 °C. To do this, we will discuss the expected SFG response of each lamellar orientation, and then, we will compare with the SFG spectra collected for the crystalline iPS films.

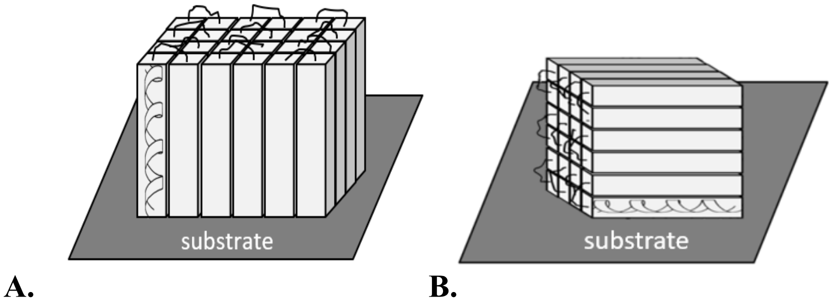

Figure 5.7. Scheme of iPS lamellar orientation A. flat-on. B. edge-on

In the flat-on lamellae, the surface of the sample is composed of the top face of the crystals, as well as of the amorphous loops formed by the chains going in and out of the crystal structure (Figure 5.7 A). The loops should have negligible contribution to the SFG response of the films because the loops can be considered to have an ensemble averaged inversion symmetry at the surface. Our hypothesis is based on the argument proposed by Li et al.[19], for an adsorbed layer of polystyrene (train-loop-tail adsorption model), in which the loops' influence on the SFG signal was neglected due to their ensemble averaged inversion symmetry at the interface arising from their amorphous nature. Therefore, the helices would be the only source of the SFG signal. In this conformation, all the phenyl ring groups in the structure assume the same tilt angle of $\theta \sim 73°$ (Figure 5.8 A and B) between the C_2 axis and the surface normal. Furthermore, all the CH_2 groups assume the same tilt angle of $\theta_b \sim 110°$ (Figure 5.8 B). Therefore, for the SFG results to be considered consistent with a flat-on lamellar structure at the surface, one may expect to have a narrow θ distribution width and an average tilt angle of about 73° for the phenyl rings. Similarly, for the CH_2 groups, one would expect an average tilt angle, θ_b, of 110° and a narrow θ_b distribution.

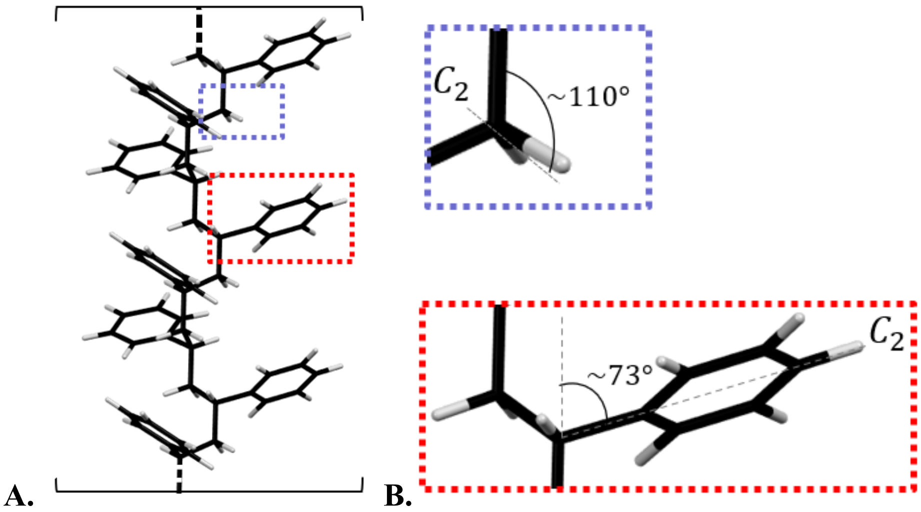

Figure 5.8. A. Scheme of crystalline structure of iPS, according to Natta et al.[244], for a flat-on crystalline orientation. B. Zoomed regions of the 3_1 helix of iPS, showing the angles between the C_2 symmetry axes of the CH_2 (θ_b) and phenyl ring groups (θ) with the surface normal.

In the edge-on lamellar orientation, the surface of the sample is the lateral face of the crystals (Figure 5.7 B), formed by the side of the iPS helices. The packing of the helices occurs in a way that the phenyl rings have various θ values (~0°, ~60°, ~120° and ~180°), as shown in Figure 5.9 A. A detailed description of the expected SFG response of the edge-on orientation is more challenging than that of the flat-on orientation, due to the multi phenyl ring and CH_2 orientations, both within a single molecule and across the ensemble of molecules forming the crystal. For a single molecule containing more than one of the same functional group with different orientations, the SFG signal of both groups may have constructive or destructive interference[245,246], depending on the angle between the groups and the surface normal. This effect is not accounted on the equations commonly used for θ and θ_b analysis that consider Gaussian angle distributions. However, considering the intermolecular packing arrangement of the iPS helices in the edge-on orientation, we may expect to have destructive SFG interference. When two or more of the same functional group is present at different orientations, the overall second order non-linear susceptibility tensor, which is responsible for the SFG response, has contributions of the non-resonant susceptibility as well as the sum of the individual resonant susceptibilities of the groups[245]. When the direction of a group is reversed, the resonant susceptibilities change sign[14]. For iPS edge-on packing, we see that each phenyl ring may be matched with another ring of the opposite orientation (Figure 5.9 B). Given these orientations, we expect the two resonant susceptibilities for the paired rings to have equivalent value, but with reversed sign, leading to destructive SFG interference. Therefore, for the edge-on crystalline orientation at the surface, we expect to see spectral signs of a broad tilt angle distribution and of destructive interference, both leading to low SFG intensity and resolution in the backbone and phenyl ring regions.

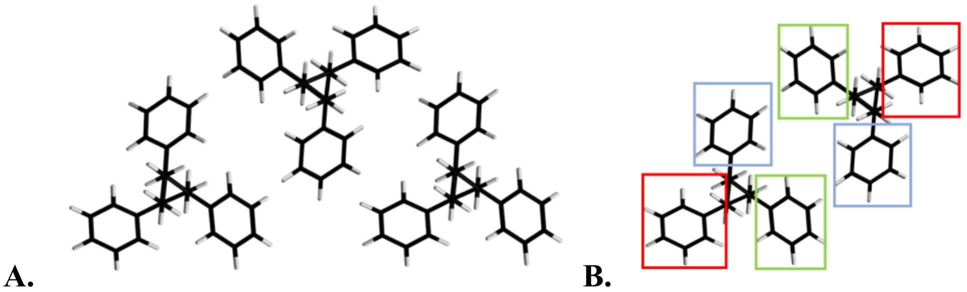

Figure 5.9. A. Scheme of crystalline structure of iPS, according to Natta et al.[244], for an edge-on crystalline orientation. B. Oppositely oriented iPS phenyl groups are shown with the same frame color.

5.5.5. Analyzing iPS lamellar orientation with SFG

For determining the iPS lamellar orientation using the SFG spectra, we will use the 16 h films due to their higher surface crystallinity and increased surface homogeneity. Furthermore, we will compare the 16 h SFG spectra and orientation analysis, with the same results of the amorphous films. The amorphous iPS surface serves as a comparison to determine the conformational changes that occur with crystallization and gives the initial intensity and peak width of the resonances before crystallization. The SFG spectra of the iPS/air interface of the films in ssp and ppp polarizations are presented in Figure 5.10 A and B. The spectra fitted with Equation 5.1 are shown in Figure 5.10 C and D for the phenyl ring resonances and in Figure 5.10 E for the backbone resonances (only ssp). The amplitudes of the phenyl ring vibrational modes, obtained through the Lorentzian fit (Equation 5.1), are presented in Table C1 of Appendix C. The phenyl ring tilt angle analyses (θ), according to methods 1 and 2 are shown in Figure 5.11, where the experimental ratios of amplitudes were plotted as the shaded regions and the overlap between the shaded regions and the solid curves represents the possible values of θ for each tilt angle distribution width (σ). The results of the tilt angle analysis are also shown in Table 5.1.

The SFG spectra of the amorphous iPS films (Figure 5.10 A) resemble the ones reported for atactic polystyrene (also amorphous) at the air interface[5,7]. While the ranges of possible values of θ obtained using methods 1 and 2 for the amorphous samples do not overlap (Table 5.1), the similarity between the results of the two methods still permits some elucidation of the orientation at the iPS/air interface. First, we may exclude the broader tilt angle distribution (σ = 30°), because with this value of σ, methods 1 and 2 differ by at least 25°. Then, when comparing the range of θ shown in Table 5.1, we can conclude that the range of possible θ for the amorphous films is 31°-58° or 122°-149°, with σ between 1° and 15°. Both the θ and distribution width range obtained for the amorphous iPS films are consistent with previous studies of the conformation of atactic polystyrene at the air interface [5,7]. The differences in the results obtained using methods 1 and 2 may arise from the different mathematical assumptions used to derive the equation of amplitude ratio as a function of θ (Equation C1 and Equation C2), which include theoretical calculations of the molecular hyperpolarizabilities. Due to the low resolution and thus high fitting parameter uncertainty of the backbone resonances of the amorphous films, it is not viable to perform the θ_b analysis. Therefore, previous authors have focused exclusively on the analysis of the phenyl ring conformation when analyzing the atactic polystyrene/air interface, which are comparable to the SFG spectra of the amorphous iPS films[5,7,8,17].

When comparing the amorphous and 16 h SFG spectra, we observe that the SFG intensity and peak widths of the vibrational modes of the phenyl ring are similar in both samples (Figure 5.10 C and D). In contrast, the resonances measured for the semi-crystalline 16 h films have narrower peak widths in the backbone frequency region when compared to the amorphous film (Figure 5.10 E). These observations are contrary to the expected SFG response for the edge-on lamellar orientation, in which a substantial destructive SFG interference is predicted. The phenyl ring θ results for the 16 h films in Figure 5.11 show that only narrow θ distribution widths are consistent with the experimental data, and there is agreement of the θ range and distribution width for methods 1 and 2 (Table 5.1). However, method 1 is better constrained when compared to method 2. While method 2 gives a wide range of possible θ, method 1 gives two narrow ranges. For example, for σ = 15°, method 2 gives a θ range of 67°-113°, while method 1 narrows the θ possibilities to 66°-73° or 107°-114°. These results are consistent with the predicted structure of a flat-on crystalline lamella (Figure 5.8), in which we expect a narrow θ distribution, and the θ

determined from the flat-on crystal geometry of θ = 73° is included in the experimentally determined tilt angle range.

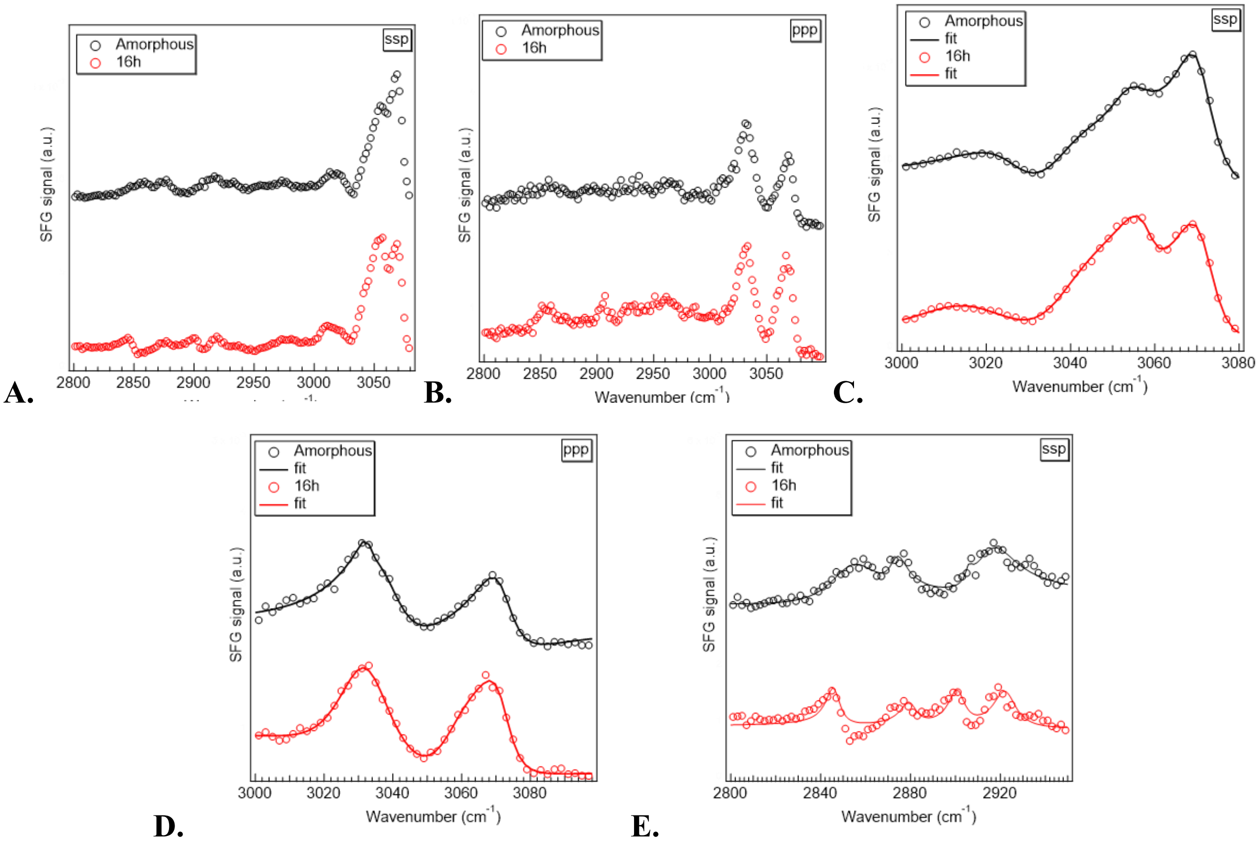

Figure 5.10. SFG spectra of iPS thin films: amorphous (black) and crystallized at 180 °C for 16h (red). A. ssp polarization, B. ppp polarization, C. Phenyl ring vibrational frequency region of ssp spectra fitted with Equation 5.1, D. Phenyl ring vibrational frequency region of ppp spectra fitted with Equation 5.1 and E. Backbone vibrational frequency region of ssp spectra fitted with Equation 5.1.

The backbone spectral features of the 16 h iPS films were well resolved, allowing the proper fitting of resonances for θ_b analysis. The ratio of the vibrational amplitudes of CH_2ss ($A_{CH_2\,\mathrm{ss}}$) and CH_2as ($A_{CH_2\,\mathrm{as}}$) is used to determine θ_b, according to the method proposed by Xiao, et al.[247]. The experimental value of $A_{CH_2\,\mathrm{ss}}/A_{CH_2\,\mathrm{as}}$ for the 16 h films was 0.4 ± 0.1, which indicates a high θ_b, in the range of 60° - 120°. This result is consistent with the expected value of $\theta_b\sim$ 110° in the helical structure of iPS in a flat-on orientation (Figure 5.8 B).

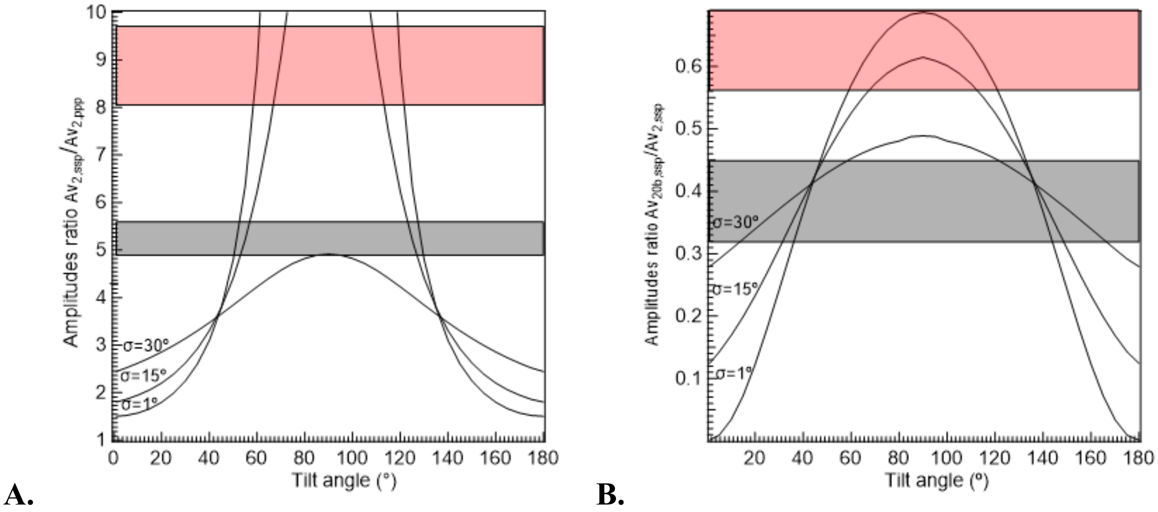

Figure 5.11. Tilt angle analysis of the pendant phenyl ring of iPS. Solid black curves represent the plots of A. Equation C1 (Method 1) and B. Equation C2 (Method 2), for different values of the tilt angle distribution width (σ = 1°, 15°, 30°). The shaded regions represent the experimental ratios of amplitudes and their standard error. Grey regions represent the amorphous sample, and the red regions represent the 16 h semi-crystalline films. The overlap of the shaded regions with the solid back curves represents possible values for θ and σ.

Table 5.1. Possible values of tilt angle assumed by the pendant phenyl ring of iPS at the iPS/air interface.

$\boldsymbol{\sigma}$	Amorphous		16h	
	Method 1 $\theta(°)$	Method 2 $\theta(°)$	Method 1 $\theta(°)$	Method 2 $\theta(°)$
$\boldsymbol{\sigma = 1°}$	50-53 or 127-130	36-47 or 133-144	58-61 or 119-122	59-121
$\boldsymbol{\sigma = 15°}$	54-58 or 122-126	31-49 or 131-149	66-73 or 107-114	67-113
$\boldsymbol{\sigma = 30°}$	84-95	14-59 or 121-166	-	-

5.5.6. Validating the iPS lamellar orientation

To validate the SFG results interpretation, AFM height images with high magnification were used (Figure 5.12 A and B). These images clearly show the presence of overgrowth terraces, which is a characteristic of the flat-on orientation[94,220,222,248]. No fibril-like structures can be seen, which demonstrates the lack of edge-on orientation.

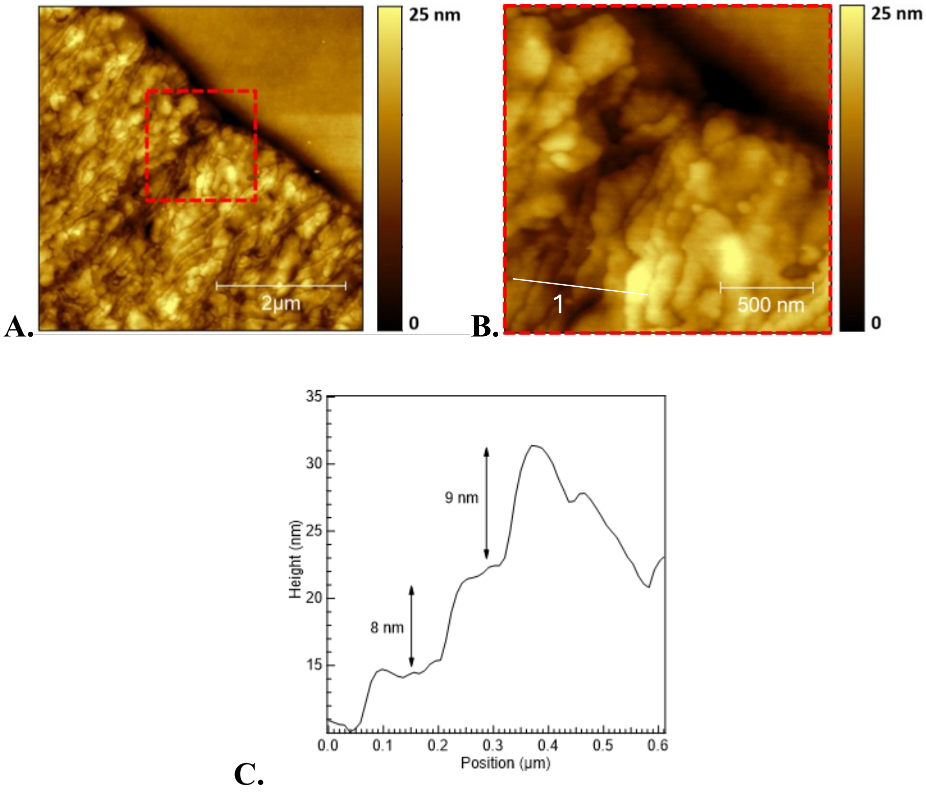

Figure 5.12. A. AFM height images of the iPS films crystallized at 180°C 2.5 h (5 µm x 5 µm), B. Zoomed region shown in a. in a red square, B. Height profile obtained over the arbitrary line 1, shown in B.

Direct measurement of the lamellar thickness by AFM is challenging and requires previous treatment of the surface such as chemical etching[249]. However, the height difference profile can be considered a good estimate of the lamellar thickness[219]. Figure 5.12 C shows the height profile over an arbitrary line (line 1 in Figure 5.12 B) at the surface of the crystal. The height profile is characteristic of the flat-on orientation, confirming the presence of the overgrowth terraces. The roughness analysis of the surface area of the crystals resulted in a root mean square height (Sq) of 3.6 ± 0.2 nm. The Sq value represents the profile height deviation from the mean line, therefore, it is possible to infer that the average terrace step height is 7.2 ± 0.4 nm (2 x Sq). This value is consistent with the height difference of about 7 nm reported by Taguchi, et al.[219] for iPS thin films crystallized at 180°C.

The crystalline lamellae orientation is dependent on the crystallization temperature, due to the different surface energies of the growing crystal. Generally, higher crystallization temperatures lead to a preferred flat-on orientation and lower crystallization temperatures lead to preferred edge-on orientation[224]. For iPS thin films, Sawamura, et al.[220] reported flat-on crystals for isothermal crystallization at 180 °C. The authors observed the edge-on conformation only at a significantly lower crystallization temperature (150 °C). The flat-on orientation observed for the iPS thin films crystallized at 180 °C in the present study is also in agreement with what is reported in other studies for iPS thin and ultra-thin films crystallized at the same temperature[231,250]. The agreement between the AFM images and the SFG results demonstrates for the first time the possibility of using of SFG to determine and to confirm the orientation of polymeric lamella in thin films at the air interface and possibly also at buried interfaces.

5.6. Conclusions

In the present work, we analyzed the orientation of crystalline lamella at the surface of iPS thin films using SFG. Amorphous iPS films presented a surface conformation comparable to the one reported for atactic polystyrene (amorphous isomer of iPS) with similar molecular weight. In summary, the phenyl rings assumed a narrow tilt angle distribution width (σ), between 1° and 15°, with the average tilt angle, θ, of 44° ± 14° or 135° ± 14°, and the polymer backbone presented a low degree of organization, most probably, to maximize the conformational entropy.

It was observed that crystallization led to the appearance of more distinguishable vibrational modes for the backbone, compared to the amorphous samples, indicating a more organized backbone structure in the crystalline film. The SFG tilt angle analyses of both phenyl ring (θ) and methylene groups (θ_b) for the 16 h films (with a surface dominated by crystalline structures) are consistent with the reported 3_1 helical structure of iPS with the chains packed in a flat-on lamellae. Here, the analysis found that iPS phenyl rings assumed a narrow σ, between 1° and 15°, with the average θ of 69° ± 4° or 111° ± 4, with the former value consistent with that expected for the flat-on structure. In the backbone region, the CH_2 θ_b, was determined to be in the range of 60° - 120°.

These findings were confirmed by AFM analysis, which also revealed a flat-on lamellar orientation at the film's surface.

This research expands the use of SFG for the characterization of polymer conformations at interfaces in semi-crystalline thin films. To the best of our knowledge, this is the first time that the lamellar orientation at the surface of a polymeric thin films has been determined by SFG orientation analysis. This study opens the way to the investigation of more complex polymeric structures and crystalline arrangements that cannot be studied by other established methods such as AFM, for example thin films buried between two solid substrates. New techniques such as SFG are needed to elucidate the critical properties in thin films, such as adhesion and wettability, which are affected by the conformation of the interfacial chains.

Chapter 6 . Conclusions

In this work, we have conducted a comprehensive investigation into the interfacial conformation of polystyrene chains across diverse interfaces using SFG spectroscopy. Our study offers significant contributions to the field of polymer science by providing detailed insights into the molecular-level arrangements at interfaces and their impact on macroscopic film behavior. We systematically explored the role of polymer molecular weight in determining the interfacial conformation near free surfaces and buried interfaces, such as silver and mica substrates, highlighting how the interplay between entropic and enthalpic forces of adsorption drives these conformations.

Additionally, our research extends beyond fundamental conformational analysis by linking interfacial arrangements to the macroscopic behavior of polymer films, particularly their dewetting properties. This connection showcases the practical implications of molecular-level conformation in controlling film stability and performance. Furthermore, we introduced an innovative application of SFG spectroscopy for examining lamellar orientations at the interfaces of semi-crystalline thin films, broadening the scope of this technique in polymer science.

Together, these findings provide a detailed understanding of the factors influencing interfacial molecular arrangements and their influence on the macroscopic film behavior. This work not only advances theoretical knowledge but also offers valuable experimental methodologies and strategies for using SFG spectroscopy as a powerful tool for interfacial studies in polymer science.

6.1. Detailed conclusions, contributions and future work by chapter

In **Chapter 3**, we conducted a detailed investigation into the interfacial conformation of PS chains near a silver substrate, with a specific focus on the influence of polymer molecular weight, using SFG spectroscopy. The chosen experimental approach enabled direct probing of these buried interfacial conformations, due to the intense plasmon field generated at the PS/silver interface. This field significantly enhances the SFG signal from the silver interface with minimum contributions from the PS/silica interface. Our results revealed that the molecular weight of PS plays a critical role in determining both the backbone and phenyl ring conformations at the interface.

Our findings demonstrated that short PS chains tend to adopt an isotropic conformation near the silver substrate, with phenyl rings tilting toward the surface to benefit from d-π interactions with the substrate. On the other hand, long PS chains assume an extended conformation that facilitates multisite adsorption, maximizing the enthalpic gain per chain. This extended conformation also induces significant torsion in the polymer backbone, which is possible by tilting the phenyl rings toward the surface normal. To our knowledge, this study represents the first application of SFG spectroscopy to elucidate the molecular weight-dependent conformational behavior of PS at a polymer/metal interface.

The insights gained from this work extend far beyond the PS/silver system, offering a foundational understanding of the balance between entropic confinement and enthalpic adsorption that governs polymer behavior near metallic substrates. These findings have implications for a wide range of applications, including coatings, adhesives, and electronic materials, where polymer-metal interfaces play a critical role. Furthermore, our research highlights the necessity of accounting for chemical interactions in the equations used for SFG orientational analysis. Specifically, we demonstrated that the commonly applied hyperpolarizability values for other interfaces are not suitable for systems involving d-π interactions, such as the silver/PS interface. This critical methodological refinement addresses a topic that is underexplored in the literature and provides a valuable insights for interpreting SFG spectra in systems involving metallic substrates.

This chapter provides an important contribution to our understanding of polymer chain behavior near metallic substrates, highlighting the impact of molecular weight on interfacial conformation through direct SFG measurements. It establishes a strong foundation for future investigations into additional factors influencing interfacial conformations at metallic interfaces. Potential directions for future research include: i) examining the effect of chain architecture, such as differences between polymers with phenyl rings in the backbone versus pendant phenyl rings; ii) analyzing chain conformations near various metals exhibiting distinct interaction types with polymers; and iii) exploring the role of surface chemistry by comparing the interfacial conformations of polymers near substrates with various chemical compositions and structures.

In **Chapter 4**, we explored the conformation of PS chains at the polymer/air and polymer/mica interfaces, investigating the influence of polymer molecular weight on their arrangement. By using SFG spectroscopy, we analyzed PS chains with molecular weights ranging from 27,000 g/mol to 344,000 g/mol. Our findings reveal that the annealing environment, whether at a free or buried interface, significantly templates the interfacial conformation of polymer chains, with these templated conformations subsequently impacting their behavior when transferred to other substrates. Specifically, we combined experimental results with theoretical calculations of enthalpic and entropic forces to establish a descriptive relationship between the initial interfacial chain conformation and the dewetting behavior of thin films.

To overcome the inherent challenges of selectively probing the PS/air and PS/mica interfaces, we introduced an innovative application of the established thin-film flotation method, adapting it as a strategy for SFG studies to selectively probe different interfaces of a single film. This approach, coupled with Fresnel factor calculations, enabled the selective enhancement of signals from targeted interfaces, representing an innovative methodological contribution to SFG spectroscopy.

Our results showed a clear distinction in interfacial conformations based on molecular weight: low molecular weight chains exhibited coiled conformations regardless of the interface, whereas high molecular weight chains displayed coiled conformations at the air interface and extended conformations at the mica interface. These variations in interfacial conformation directly influenced dewetting behavior. Films composed of low molecular weight PS exhibited slow dewetting rates regardless of their interfacial history. In contrast, high molecular weight PS films showed significantly different behaviors: air-templated chains with coiled conformations exhibited rapid dewetting due to the high entropic cost of adsorption, whereas mica-templated chains with extended conformations demonstrated slower dewetting rates, benefiting from higher enthalpic gain of multisite interaction, enhancing the film stability.

One of the key discoveries of this work is the critical role that initial chain arrangement plays in dictating the macroscopic behavior of thin films, particularly their dewetting dynamics. Furthermore, we highlighted the powerful templating effect of the annealing conditions on the interfacial conformations, which could potentially be leveraged in other polymer systems. This study not only advances our understanding of the interplay between molecular structure, annealing conditions, and thin film performance but also bridges fundamental polymer science and practical applications, offering innovative approaches to controlling thin film behavior.

In addition to these scientific contributions, we address long-standing questions in the literature regarding the disparity in dewetting behavior observed between two interfaces of a single film, providing robust hypotheses grounded in interfacial conformation differences. This work also introduces the thin-film flotation method as a powerful tool for probing distinct interfaces within a single film using SFG spectroscopy, broadening the technique's applicability to systems with substrates traditionally unsuitable for SFG measurements.

Future research inspired by this study could explore several avenues, such as: i) examining how templated interfacial conformations affect other film properties like adhesion and barrier performance; ii) investigating the behavior of PS chains with extremely low or high molecular weights to test the generalizability of our observed trends; and iii) developing reverse manufacturing strategies that utilize substrate-templated effects to achieve desired initial chain conformations, whether extended or coiled. These opportunities underscore the foundational impact of our findings on polymer science and thin film technology.

In **Chapter 5**, we explored the application of SFG spectroscopy to determine the lamellar orientation of surface iPS crystals, representing a significant advance in the interfacial analysis of semi-crystalline polymers. By performing SFG measurements and orientation analyses on iPS films with varying isothermal crystallization times, we successfully identified the presence of flat-on lamellar orientations at the film surfaces. This identification was achieved by combining experimental SFG data with theoretical predictions of SFG responses for the two possible lamellar orientations (flat-on and edge-on orientations), and it was subsequently confirmed through AFM analysis.

Despite the common presence of semi-crystalline polymers in practical applications, the use of SFG spectroscopy to analyze such systems remains largely underexplored. Our research addressed this gap, highlighting both the potential and the challenges of applying SFG spectroscopy to semi-crystalline films. Specifically, we demonstrated that the intrinsic heterogeneity of these films, where crystalline and amorphous regions coexist, necessitates careful treatment of SFG data. We emphasized the importance of acquiring a large number of spectra to account for sample heterogeneity and of properly classifying these spectra to avoid misinterpretation. These considerations are crucial, as the spectra may represent crystalline regions, amorphous regions, or a mixture of both, and averaging such data for orientation analysis can lead to erroneous conclusions.

Our study represents significant contributions to the field of interfacial analysis of semi-crystalline polymer films. First, we established that the ratios of SFG intensities for specific vibrational modes can serve as a reliable, non-contact, and non-destructive indicator of surface crystallinity. This provides a valuable tool for characterizing surface properties in situ. Second, we presented a comprehensive theoretical discussion for interpreting SFG responses of semi-crystalline polymer thin films, elucidating the key differences between lamellar orientations and demonstrating how theoretical insights can greatly contribute to the analysis of experimental data. To the best of our knowledge, this is the first study to utilize SFG spectroscopy for determining surface lamellar orientation in semi-crystalline polymeric thin films.

These advancements open new possibilities for the application of SFG spectroscopy in polymer research. Our work not only expands the analytical capabilities for studying surface crystallinity and lamellar orientation but also provides a foundation for further exploration. Potential future directions include: i) probing lamellar orientations at buried interfaces; ii) investigating other polymers with diverse crystalline structures; and iii) conducting in situ studies of semi-crystalline polymers during isothermal crystallization to monitor molecular rearrangements during nucleation and crystal growth.

APPENDIX A. Supplementary information for Chapter 3

A1. Calculation of the uncertainty

The uncertainty ($\delta\bar{x}$) for each parameter x was determined by error propagation of the fitting uncertainties (δx) given by the software, according to $\delta\bar{x} = 1/6 * \sqrt{(\delta x_1)^2 + (\delta x_2)^2 + \cdots + (\delta x_6)^2}$, where the subscript numbers represent each fitting. Furthermore, the uncertainties on the ratios of different amplitudes $\delta(A/B)$ were determined by propagating the uncertainties for the amplitudes calculated by the previous method, according to $\delta(A/B) = \frac{A}{B} * \sqrt{\left(\frac{\delta A}{\bar{A}}\right)^2 + \left(\frac{\delta B}{\bar{B}}\right)^2}$, where A and B represent two different vibrational amplitudes[251].

A2. Local plasmon field

The decay in the plasmon field intensity across the PS film was calculated following the approach published by Read et al.[140] for a continuous metal surface. The result is shown in Figure A1. The exponential decay of the plasmon field can be expressed as exp $(-2z/l_d)$, where z is the distance from the silver surface and l_d is the plasmon field propagation depth, defined as:

$$l_d = \frac{\lambda_0}{2\pi}\sqrt{\left|\frac{\varepsilon_m + \eta^2}{\eta^4}\right|} \qquad \text{Equation A1}$$

Here, λ_0 is the wavelength of the excitation radiation, with a value of 532 nm for the visible radiation; ε_m is the real part of the relative permittivity of silver, with a value of 16.2[252] and η is the refractive index of polystyrene, with a value of 1.61[7]. The intensity of the plasmon field decays exponentially and reaches about 20% of its initial value at the silica/PS interface, making the signal of this interface negligible with respect to the total SFG signal.

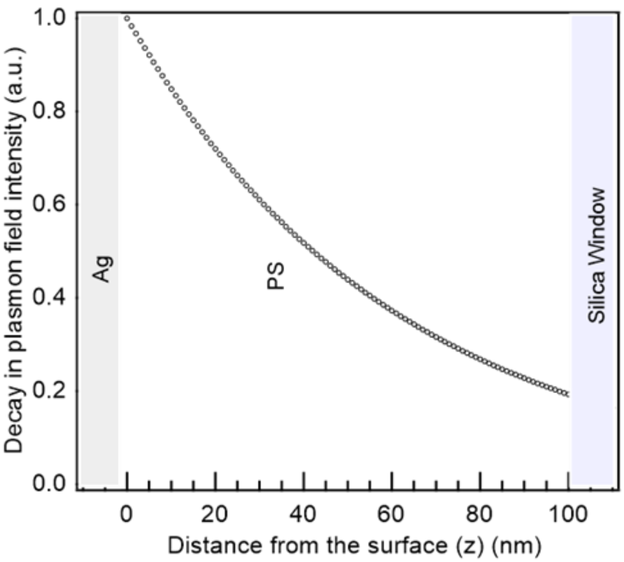

Figure A1. Decay in the plasmon field radiation as a function of the distance from the silver surface.

A3. Tilt angle analysis using ssp amplitudes for ν_{20b} and ν_2 modes

SFG can be seen as two consecutive processes, infrared absorption, followed by Raman scattering. Therefore, the plasmon enhancement effects observed for surface enhanced Raman spectroscopy (SERS) can be expected to influence the SFG spectra. In fact, Chulhai et al.[253] proposed that surface-enhanced SFG can be, at some level, interpreted as a ''SERS-like'' process. In this sense, the SFG signal is not only related to the isolated molecular hyperpolarizabilities (β_{SFG}^{M}), but to the total hyperpolarizability of the molecule/metal system β_{SFG}^{tot}. In a similar way to what is widely reported for the total polarizability in SERS experiments, one can expect β_{SFG}^{tot} to have contributions from two enhancement mechanisms, the electromagnetic mechanism (EMM) and the chemical mechanism (CM)[253].

In the vicinity of a metal surface, the electron distribution within the molecule is perturbed, which changes the values of the hyperpolarizability elements. Baldelli et al.[254] reported that the hyperpolarizability ratio β_{yyz}/β_{zzz} for carbon monoxide adsorbed on platinum was up to 6 times higher than that of the free molecule. The authors attributed the changes in the hyperpolarizabilities to the electron transfer from the d-orbitals of platinum to the π^* orbitals of the CO molecules, which changed the overall shape of the electron distribution.

Equation 3.6 cannot be used in a quantitative analysis of the tilt angle distribution unless the values of the hyperpolarizabilities for the phenyl group adsorbed on silver are known. The calculation of the hyperpolarizabilities of PS adsorbed on silver goes beyond the scope of this paper, so only a qualitative discussion of the tilt angle analysis using Equation 3.6 is presented here. The goal of this section is to demonstrate that this alternative method for determining tilt angle leads to a result that is qualitatively consistent with the approach presented in the thesis text and that is based on Equation 3.5.

The general qualitative relationship between the $A_{\nu 20b}/A_{\nu 2}$ ratio in ssp polarization (R) and tilt angle is shown in Figure A2. Furthermore, the R value obtained experimentally using the amplitudes of the ν_{20b} and ν_2 modes in ssp polarization are presented in Figure A3. The decrease in the R value with increasing Mw indicates that tilt angle also decreases with increasing Mw. This qualitative trend is consistent with the tilt angle analysis presented in the main text, where the tilt angles were determined using different SFG polarization combinations (Equation 3.5).

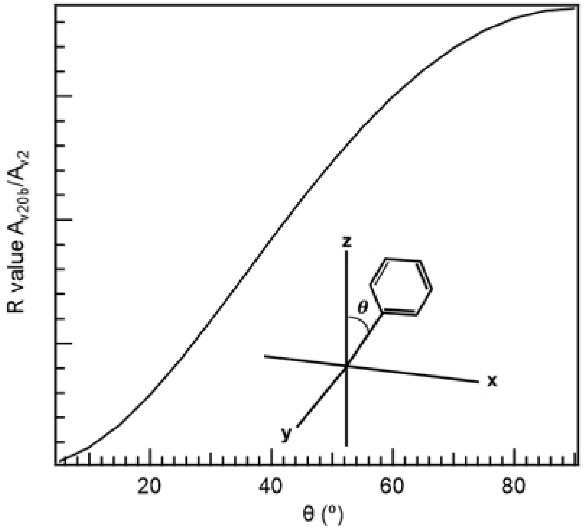

Figure A2. Qualitative relationship between the R value ($A_{\nu 20b}/A_{\nu 2}$) and the tilt angle, θ.

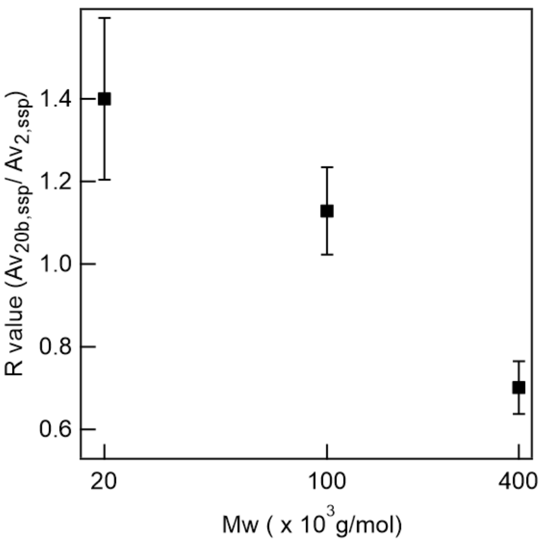

Figure A3. R value obtained from the ssp spectra as a function of PS Mw. The uncertainties were determined as described in section A1 for the ratio of the amplitudes.

APPENDIX B. Supplementary information for Chapter 4

B1. SFG spectra fitting

The SFG spectra were fitted using a Lorentzian equation (Equation B1)[7,10], to obtain the amplitudes of the vibrational modes of the pendant phenyl ring and backbone groups. Here, I_{SFG} is the SFG intensity, χ_{eff} is the effective second-order non-linear susceptibility tensor, χ_{NR} and a are the non-resonant signal and its phase, respectively, A_q is the amplitude of the vibrational mode q, ω_{IR} and ω_q are the infrared (IR) beam frequency and the frequency of the resonant vibrational mode q, respectively, and Γ_q is a damping constant. The frequency assignments to the PS vibrational modes were made according to our previous publications[187,188].

$$I_{SFG} \propto \left|\chi_{eff}\right|^2 = \left|\chi_{NR}e^{i\alpha} + \sum_q \frac{A_q}{\omega_{IR}-\omega_q+i\Gamma_q}\right|^2 \qquad \text{Equation B1}$$

B2. SFG spectra of PS films

Typical SFG spectral curves fitted using Equation B1 in the phenyl ring and backbone vibrational regions are presented in Figure B1.

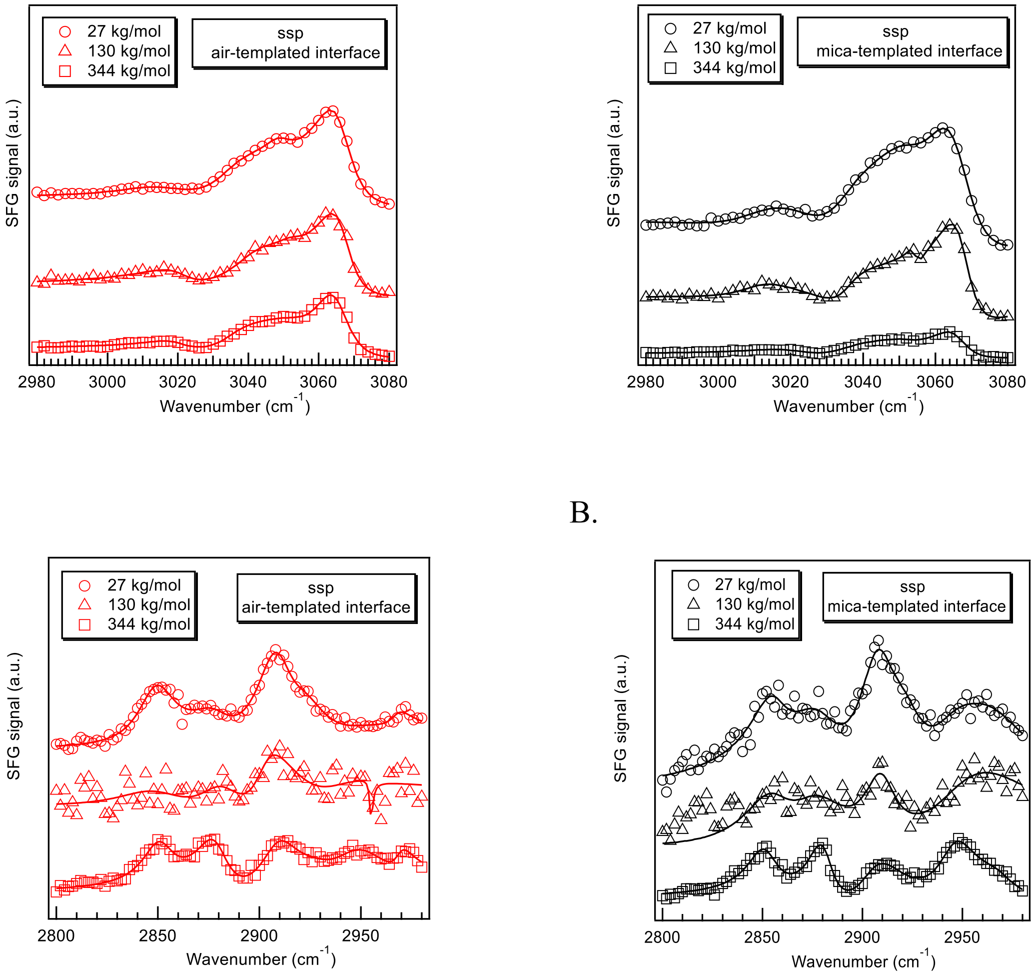

A. B.

C. D.

Figure B1. Typical SFG spectra of PS thin films. Markers represent SFG signal and lines represent the fittings using Equation B1. A. Air-templated interface - phenyl ring vibrational region. B. Mica-templated interface - phenyl ring vibrational region. C. A. Air-templated interface - backbone vibrational region and D. Mica-templated interface - backbone vibrational region.

B3. Phenyl ring orientational analysis

Two well-established approaches were employed to determine the possible range of tilt angles for the pendant phenyl ring of the PS samples. The first approach [7] uses the ratio of the ν_2 amplitudes in ssp and ppp polarizations to determine the range of possible tilt angle values. This relationship is shown in Equation B2, where $A_{\nu 2}$ represent the amplitude of the ν_2 mode and the brackets represent an ensemble average.

$$\frac{A_{\nu 2,ssp}}{A_{\nu 2,ppp}} \cong \frac{0.65\langle\cos\theta\rangle - 0.20\langle cos^3\theta\rangle}{-0.01\langle\cos\theta\rangle + 0.31\langle cos^3\theta\rangle} \qquad \text{Equation B2}$$

The second approach[6,10,13,141] relates the ratio of the ν_{20b} and ν_2 amplitudes in ssp polarization to the possible range of θ (Equation B3). Here, $A_{\nu 20b}$ represent the amplitude of the ν_{20b} vibrational mode, and $\beta_{caa,\nu 20b}/\beta_{aac,\nu 2}$ is the ratio of the hyperpolarizability components for ν_{20b} and ν_2 modes.

$$\left|\frac{A_{\nu 20b,ssp}}{A_{\nu 2,ssp}}\right| = \left|\left(\frac{\beta_{caa,\nu 20b}}{\beta_{aac,\nu 2}}\right)\left(\frac{2(\langle\cos 3\theta\rangle - \langle\cos\theta\rangle)}{(7+2r)\langle\cos\theta\rangle + (1-2r)\langle\cos 3\theta\rangle}\right)\right| \qquad \text{Equation B3}$$

B4. Range of phenyl ring tilt angle for PS samples

The range of possible values of θ obtained using Equation B2 and B3, as well as the overlap region between the two approaches, are shown in Table B1.

Table B1. The tilt angle of the pendant phenyl ring of PS samples, using Equation B2 and Equation B3.

Sample	Tilt angle range*		
	Equation B2	Equation B3	Overlapping region
27 kg/mol air-templated interface	33 ° - 47 °	28 ° - 38 °	33 ° - 38 °
27 kg/mol mica-templated interface	0 ° - 36 °	33 ° - 49 °	33 ° - 36 °
130 kg/mol air-templated interface	0 ° - 45 °	33 ° - 42 °	33 ° - 42 °
130 kg/mol mica-templated interface	32 ° - 44 °	31 ° - 37 °	32 ° - 37 °
344 kg/mol air-templated interface	26 ° - 35 °	20° - 36 °	26 ° - 35 °
344 kg/mol mica-templated interface	42 ° - 47 °	44 ° - 90 °	44 ° - 47 °

* Considering a narrow tilt angle distribution of 1°

APPENDIX C. Supplementary information for Chapter 5

C1. SFG equations for phenyl ring orientation analysis

Two methods were used to calculate the possible tilt angle range for the pendant phenyl ring at the iPS/air interface.

Method 1

This method, shown in Equation C1, relates the ratio of the ν_2 amplitudes in ssp and ppp polarizations to the θ range. Lu and co-workers[7] have previously reported the derivation of Equation C1, which is used here as reported by the authors. In Equation C1, $A_{\nu 2,ssp}$ and $A_{\nu 2,ppp}$ represent the amplitudes of the ν_2 mode in ssp and ppp polarization, respectively, and the brackets represent an ensemble average.

$$\frac{A_{\nu 2,ssp}}{A_{\nu 2,ppp}} \cong \frac{0.65\langle\cos\theta\rangle - 0.20\langle cos^3\theta\rangle}{-0.01\langle\cos\theta\rangle + 0.31\langle cos^3\theta\rangle} \qquad \text{Equation C1}$$

Method 2

This is the most commonly used approach to estimate the θ range at the air/PS interface[10,13,141]. As shown in Equation C2, the ratio of the ν_{20b} and ν_2 amplitudes in ssp polarization are used to obtain the θ range. In Equation C2, $A_{\nu 20b,ssp}$ represent the amplitude of the ν_{20b} vibrational mode in the ssp polarization. Also, $\beta_{caa,\nu 20b}$ and $\beta_{aac,\nu 2}$ are hyperpolarizability components for ν_{20b} and ν_2 modes, respectively, and r is the ratio between β_{ccc}/β_{aac} for the ν_2 mode. Here, we have used $\beta_{caa,\nu 20b}/\beta_{aac,\nu 2} = 1.12$ and $r = 1.13$, as reported by Hong and co-workers[6].

$$\left|\frac{A_{\nu 20b,ssp}}{A_{\nu 2,ssp}}\right| = \left|\left(\frac{\beta_{caa,\nu 20b}}{\beta_{aac,\nu 2}}\right)\left(\frac{2(\langle\cos 3\theta\rangle - \langle\cos\theta\rangle)}{(7+2r)\langle\cos\theta\rangle + (1-2r)\langle\cos 3\theta\rangle}\right)\right| \qquad \text{Equation C2}$$

C2. Fresnel coefficients of the silica/iPS and iPS/air interfaces

The SFG intensity (I_{SFG}) is proportional to the square of the effective second-order non-linear susceptibility tensor (χ_{eff}) (Equation C3).

$$I_{SFG} \propto \left|\chi_{eff}\right|^2 \qquad \text{Equation C3}$$

Each interface present in the sample contributes to χ_{eff}, as well as the non-resonant background, χ_{NR}[63]. The participation of each interface in the overall SFG signal is based on the Fresnel coefficients (F), responsible for the local field corrections at the interface, as well as the magnitude of the second-order non-linear susceptibility tensor at the interface, χ. For the geometry used in the present study, we have:

$$\chi_{eff} = F^{silica/iPS}\chi^{silica/iPS} + F^{iPS/air}\chi^{iPS/air} + \chi_{NR} \qquad \text{Equation C4}$$

The components of F and χ in χ_{eff} for the ssp and ppp polarization combinations are:

$$\chi_{eff,ssp} = F_{yyz}^{silica/iPS}\chi_{yyz}^{silica/iPS} + F_{yyz}^{iPS/air}\chi_{yyz}^{silica/iPS} + \chi_{NR,ssp} \qquad \text{Equation C5}$$

$$\chi_{eff,ppp} = F_{xxz}^{silica/iPS}\chi_{xxz}^{silica/iPS} + F_{xxz}^{iPS/air}\chi_{xxz}^{silica/iPS} + F_{xzx}^{silica/iPS}\chi_{xzx}^{silica/iPS} + F_{xzx}^{iPS/air}\chi_{xzx}^{silica/iPS} + F_{zxx}^{silica/iPS}\chi_{zxx}^{silica/iPS} + F_{zxx}^{iPS/air}\chi_{zxx}^{silica/iPS} + F_{zzz}^{silica/iPS}\chi_{zzz}^{silica/iPS} + F_{zzz}^{iPS/air}\chi_{zzz}^{silica/iPS} + \chi_{NR,ppp} \qquad \text{Equation C6}$$

We used the thin film model reported by Lu, X.[63,112] to calculate the Fresnel coefficients at the 2 interfaces present in the current study. The visible and infrared beams incidence angles are 60° and 55°, respectively, with respect to the surface normal. The refraction indexes of each media used in the model were reported by Lu, X.[7]. Figure C1 shows the $\left|F_{yyz}\right|$ coefficients (ssp polarization) as a function of the iPS film thickness for the silica/iPS and iPS/air interfaces. It can be seen that the iPS film thickness used in the present study (100nm) is in the region where

$\left|F_{yyz}^{silica/iPS}\right|$ is minimum. More specifically, the magnitude of $\left|F_{yyz}^{iPS/air}\right|$ is 10 times stronger than $\left|F_{yyz}^{silica/iPS}\right|$.

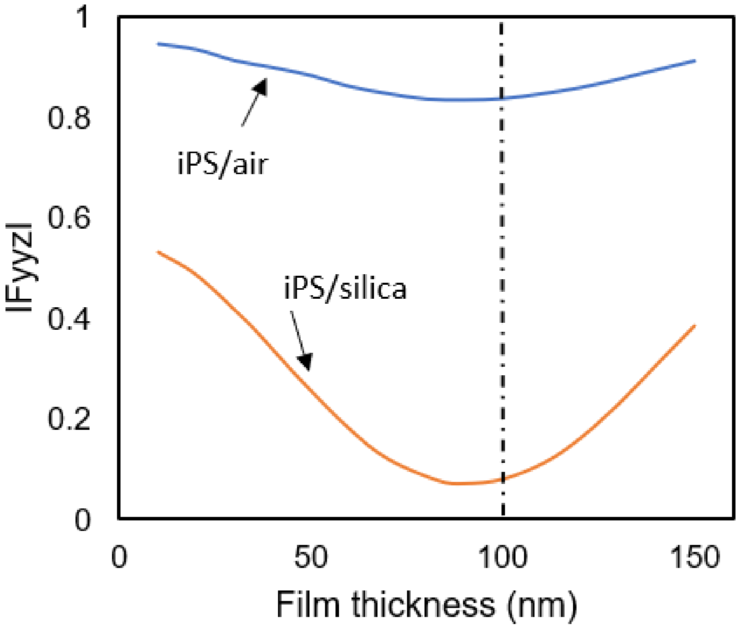

Figure C1. F_{yyz} magnitude for silica/iPS and iPS/air interfaces as a function of film thickness

The modulus of the Fresnel coefficients for a 100 nm iPS thin film for ppp polarization are shown in Table C1. From Table C1, it can be seen that each component of the Fresnel coefficients, $\left|F_{xxz}^{iPS/air}\right|$, $\left|F_{xzx}^{iPS/air}\right|$, $\left|F_{xxz}^{iPS/air}\right|$ and $\left|F_{zzz}^{iPS/air}\right|$ is between 1.5x to 6x stronger than its equivalent for the iPS/air interface, $\left|F_{xxz}^{silica/iPS}\right|$, $\left|F_{xzx}^{silica/iPS}\right|$, $\left|F_{xxz}^{silica/iPS}\right|$ and $\left|F_{zzz}^{silica/iPS}\right|$. Therefore, all components contributing to the SFG signal in ppp polarization are magnified for the iPS/air interface, compared to the silica/iPS interface.

Table C1. Fresnel coefficients for iPS/air and silica/iPS

$\lvert F_{xxz}^{iPS/air}\rvert$	$\lvert F_{xzx}^{iPS/air}\rvert$	$\lvert F_{zxx}^{iPS/air}\rvert$	$\lvert F_{zzz}^{iPS/air}\rvert$
0.33	0.40	0.41	0.48
$\lvert F_{xxz}^{silica/iPS}\rvert$	$\lvert F_{xzx}^{silica/iPS}\rvert$	$\lvert F_{zxx}^{silica/iPS}\rvert$	$\lvert F_{zzz}^{silica/iPS}\rvert$
0.21	0.22	0.23	0.08

It is important to highlight that the SFG signal has a quadratic dependence on χ_{eff}, as shown in Equation C3. Therefore, a higher Fresnel coefficient for one interface compared with the other, means that the resonant vibrational SFG signal from that interface will be quadratically magnified.

C3. SFG of heterogeneous surfaces

The area probed by the SFG spectrometer was estimated to be about 300 μm^2 based on the area burned on a piece of paper by the visible beam. The effective area probed is less than this value because it constitutes the area in which there is an overlap between the visible and infrared beams. When the SFG spectra is collected, the probing spot is randomly chosen, with no control or view of the features present in the probed area. In Figure C2, we show the optical microscopy of the 5 h film. The area of the squares indicates the area probed by SFG. One may observe that, there is a probability that the SFG probed area falls in a region with no crystals (white squares), and the resulting spectra would be similar to the one of the amorphous film. The other extreme case would be red squares, in which the SFG probed area falls in a region richer in crystals, compared to the rest of the film, and the resulting spectra would resemble the ones for the 16 h films. Lastly, most spectra would be collected from regions that are better representations of the average surface crystallinity of the film (yellow squares), and the resulting spectra would be intermediate between the white and red regions.

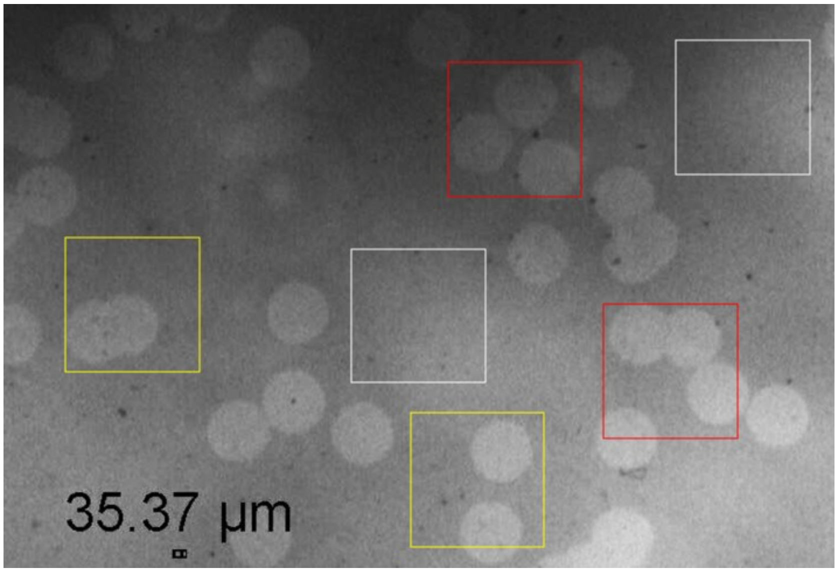

Figure C2. Optical microscopy of 5 h films. The area of the squares is 300 µm^2, equivalent to the area probed by the visible and IR beams. White squares are in a region with no crystals. Red squares are in a region with high surface crystallinity. Yellow squares contain a balance of amorphous and crystalline phases.

C4. Fitting amplitudes of phenyl ring resonances

Table C2. Amplitudes of the vibrational modes of the pendant phenyl ring of iPS. The amplitudes were obtained through fitting the SFG spectra with a Lorentzian equation (Equation C1).

Resonant mode	**ssp amplitude ± standard error**	**ppp amplitude ± standard error**
ν_{20b}	0.25 ± 0.04	0.011 ± 0.007
ν_{7a}	0.4 ± 0.1	0.16 ± 0.02
ν_{7b}	0.09 ± 0.02	0.26 ± 0.02
ν_{2}	0.67 ± 0.03	0.13 ± 0.01

References

(1) Nguyen, H. K.; Inutsuka, M.; Kawaguchi, D.; Tanaka, K. Depth-Resolved Local Conformation and Thermal Relaxation of Polystyrene near Substrate Interface. *J. Chem. Phys.* **2017**, *146* (20), 203313. https://doi.org/10.1063/1.4976523.

(2) Brown, H. R.; Russell, T. P. Entanglements at Polymer Surfaces and Interfaces. *Macromolecules* **1996**, *29* (2), 798–800. https://doi.org/10.1021/ma951123k.

(3) Opdahl, A.; Phillips, R. A.; Somorjai, G. A. Surface Segregation of Methyl Side Branches Monitored by Sum Frequency Generation (SFG) Vibrational Spectroscopy for a Series of Random Poly(Ethylene- Co -Propylene) Copolymers. *J. Phys. Chem. B* **2002**, *106* (20), 5212–5220. https://doi.org/10.1021/jp013741a.

(4) Li, B.; Lu, X.; Ma, Y.; Han, X.; Chen, Z. Method to Probe Glass Transition Temperatures of Polymer Thin Films. *ACS Macro Lett.* **2015**, *4* (5), 548–551. https://doi.org/10.1021/acsmacrolett.5b00185.

(5) Bzeih, W.; Gheribi, A.; Wood-Adams, P. M.; Hayes, P. L. Dependence of the Surface Structure of Polystyrene on Chain Molecular Weight Investigated by Sum Frequency Generation Spectroscopy. *J. Phys. Chem. C* **2018**, *122* (7), 3838–3845. https://doi.org/10.1021/acs.jpcc.7b08574.

(6) Hong, Y.; Bao, S.; Xiang, X.; Wang, X. Concentration-Dominated Orientation of Phenyl Groups at the Polystyrene/Graphene Interface. *ACS Macro Lett.* **2020**, *9* (6), 889–894. https://doi.org/10.1021/acsmacrolett.0c00279.

(7) Lu, X.; Myers, J. N.; Chen, Z. Molecular Ordering of Phenyl Groups at the Buried Polystyrene/Metal Interface. *Langmuir* **2014**, *30* (31), 9418–9422. https://doi.org/10.1021/la502037h.

(8) Gautam, K. S.; Schwab, A. D.; Dhinojwala, A.; Zhang, D.; Dougal, S. M.; Yeganeh, M. S. Molecular Structure of Polystyrene at Air/Polymer and Solid/Polymer Interfaces. *Phys. Rev. Lett.* **2000**, *85* (18), 3854–3857. https://doi.org/10.1103/PhysRevLett.85.3854.

(9) Myers, J. N.; Zhang, C.; Chen, C.; Chen, Z. Influence of Casting Solvent on Phenyl Ordering at the Surface of Spin Cast Polymer Thin Films. *J. Colloid Interface Sci.* **2014**, *423*, 60–66. https://doi.org/10.1016/j.jcis.2014.02.027.

(10) Tsuruta, H.; Fujii, Y.; Kai, N.; Kataoka, H.; Ishizone, T.; Doi, M.; Morita, H.; Tanaka, K. Local Conformation and Relaxation of Polystyrene at Substrate Interface. *Macromolecules* **2012**, *45* (11), 4643–4649. https://doi.org/10.1021/ma3007202.

(11) Wilson, P. T.; Richter, L. J.; Wallace, W. E.; Briggman, K. A.; Stephenson, J. C. Correlation of Molecular Orientation with Adhesion at Polystyrene/Solid Interfaces. *Chem. Phys. Lett.* **2002**, *363* (1–2), 161–168. https://doi.org/10.1016/S0009-2614(02)01171-5.

(12) Tian, C. S.; Shen, Y. R. Recent Progress on Sum-Frequency Spectroscopy. *Surf. Sci. Rep.* **2014**, *69* (2–3), 105–131. https://doi.org/10.1016/j.surfrep.2014.05.001.

(13) Curtis, A. D.; Calchera, A. R.; Asplund, M. C.; Patterson, J. E. Observation of Sub-Surface Phenyl Rings in Polystyrene with Vibrationally Resonant Sum-Frequency Generation. *Vib. Spectrosc.* **2013**, *68*, 71–81. https://doi.org/10.1016/j.vibspec.2013.05.011.

(14) Lambert, A. G.; Davies, P. B.; Neivandt, D. J. Implementing the Theory of Sum Frequency Generation Vibrational Spectroscopy: A Tutorial Review. *Appl. Spectrosc. Rev.* **2005**, *40* (2), 103–145. https://doi.org/10.1081/ASR-200038326.

(15) Dreesen, L.; Humbert, C.; Hollander, P.; Mani, A. A.; Ataka, K.; Thiry, P. A.; Peremans, A. Study of the Water/Poly(Ethylene Glycol) Interface by IR-Visible Sum-Frequency Generation Spectroscopy. *Chem. Phys. Lett.* **2001**, *333* (5), 327–331. https://doi.org/10.1016/S0009-2614(00)01383-X.

(16) Chen, C.; Even, M. A.; Wang, J.; Chen, Z. Sum Frequency Generation Vibrational Spectroscopy Studies on Molecular Conformation of Liquid Polymers Poly(Ethylene Glycol) and Poly(Propylene Glycol) at Different Interfaces. *Macromolecules* **2002**, *35* (24), 9130–9135. https://doi.org/10.1021/ma020614j.

(17) Briggman, K. A.; Stephenson, J. C.; Wallace, W. E.; Richter, L. J. Absolute Molecular Orientational Distribution of the Polystyrene Surface. *J. Phys. Chem. B* **2001**, *105* (14), 2785–2791. https://doi.org/10.1021/jp0037495.

(18) Li, B.; Chen, L.; Zhang, S.; Tao, Q.; Ma, Y.-H.; Hu, P.; Lu, X.; Chou, K. C.; Chen, Z. Absolute Molecular Structure of the Polystyrene at the Buried Polystyrene/Silica Interface and Its Relationship to Dewetting during Annealing. *Appl. Surf. Sci.* **2023**, *611*, 155715. https://doi.org/10.1016/j.apsusc.2022.155715.

(19) Li, X.; Lu, X. Evolution of Irreversibly Adsorbed Layer Promotes Dewetting of Polystyrene Film on Sapphire. *Macromolecules* **2018**, *51* (17), 6653–6660. https://doi.org/10.1021/acs.macromol.8b01141.

(20) Ramli Sulong, N. H.; Mustapa, S. A. S.; Abdul Rashid, M. K. Application of Expanded Polystyrene (EPS) in Buildings and Constructions: A Review. *J. Appl. Polym. Sci.* **2019**, *136* (20). https://doi.org/10.1002/app.47529.

(21) McKee, G. E.; Kistenmacher, A.; Goerrissen, H.; Breulmann, M. Synthesis, Properties and Applications of Acrylonitrile–Styrene–Acrylate Polymers. In *Modern Styrenic Polymers: Polystyrenes and Styrenic Copolymers*; Scheirs, J., Priddy, D. B., Eds.; Wiley, 2003; pp 341–362. https://doi.org/10.1002/0470867213.ch16.

(22) Mckeen, L. W. Introduction to Plastics, Polymers, and Their Properties. In *The Effect of Temperature and Other Factors on Plastics and Elastomers*; Elsevier, 2023; pp 1–45. https://doi.org/10.1016/B978-0-323-99555-9.00002-6.

(23) Pawlak, A.; Krajenta, J. Entanglements of Macromolecules and Their Influence on Rheological and Mechanical Properties of Polymers. *Molecules* **2024**, *29* (14), 3410. https://doi.org/10.3390/molecules29143410.

(24) Brochard-Wyart, F.; de Gennes, P.-G.; Hervert, H.; Redon, C. Wetting and Slippage of Polymer Melts on Semi-Ideal Surfaces. *Langmuir* **1994**, *10* (5), 1566–1572. https://doi.org/10.1021/la00017a040.

(25) Doi, M. Explanation for the 3.4-power Law for Viscosity of Polymeric Liquids on the Basis of the Tube Model. *Journal of Polymer Science: Polymer Physics Edition* **1983**, *21* (5), 667–684. https://doi.org/10.1002/pol.1983.180210501.

(26) McLeish, T. C. B. Tube Theory of Entangled Polymer Dynamics. *Adv Phys* **2002**, *51* (6), 1379–1527. https://doi.org/10.1080/00018730210153216.

(27) Pei, D.; Wang, Z.; Peng, Z.; Zhang, J.; Deng, Y.; Han, Y.; Ye, L.; Geng, Y. Impact of Molecular Weight on the Mechanical and Electrical Properties of a High-Mobility Diketopyrrolopyrrole-Based Conjugated Polymer. *Macromolecules* **2020**, *53* (11), 4490–4500. https://doi.org/10.1021/acs.macromol.0c00209.

(28) Promnil, S.; Numpaisal, P.; Ruksakulpiwat, Y. Effect of Molecular Weight on Mechanical Properties of Electrospun Poly (Lactic Acid) Fibers for Meniscus Tissue Engineering Scaffold. *Mater. Today: Proc.* **2021**, *47*, 3496–3499. https://doi.org/10.1016/j.matpr.2021.03.504.

(29) Sangroniz, L.; Fernández, M.; Santamaria, A. Polymers and Rheology: A Tale of Give and Take. *Polymer (Guildf)* **2023**, *271*, 125811. https://doi.org/10.1016/j.polymer.2023.125811.

(30) Gentekos, D. T.; Sifri, R. J.; Fors, B. P. Controlling Polymer Properties through the Shape of the Molecular-Weight Distribution. *Nat. Rev. Mater.* **2019**, *4* (12), 761–774. https://doi.org/10.1038/s41578-019-0138-8.

(31) Nunes, R. W.; Martin, J. R.; Johnson, J. F. Influence of Molecular Weight and Molecular Weight Distribution on Mechanical Properties of Polymers. *Polym. Eng. Sci.* **1982**, *22* (4), 205–228. https://doi.org/10.1002/pen.760220402.

(32) Fernández-Tena, A.; Pérez-Camargo, R. A.; Coulembier, O.; Sangroniz, L.; Aranburu, N.; Guerrica-Echevarria, G.; Liu, G.; Wang, D.; Cavallo, D.; Müller, A. J. Effect of Molecular Weight on the Crystallization and Melt Memory of Poly(ε-Caprolactone) (PCL). *Macromolecules* **2023**, *56* (12), 4602–4620. https://doi.org/10.1021/acs.macromol.3c00234.

(33) Chen, X.; Hou, G.; Chen, Y.; Yang, K.; Dong, Y.; Zhou, H. Effect of Molecular Weight on Crystallization, Melting Behavior and Morphology of Poly(Trimethylene Terephalate). *Polym. Test.* **2007**, *26* (2), 144–153. https://doi.org/10.1016/j.polymertesting.2006.08.011.

(34) Broseta, D.; Fredrickson, G. H.; Helfand, E.; Leibler, L. Molecular Weight and Polydispersity Effects at Polymer-Polymer Interfaces. *Macromolecules* **1990**, *23* (1), 132–139. https://doi.org/10.1021/ma00203a023.

(35) Sauer, B. B.; Dee, G. T. Surface Tensions of Molten Polymers as a Function of Molecular Weight and Temperature. *MRS Proceedings* **1991**, *248*, 441. https://doi.org/10.1557/PROC-248-441.

(36) Legrand, D. G.; Gaines, G. L. The Molecular Weight Dependence of Polymer Surface Tension. *J. Colloid Interface Sci.* **1969**, *31* (2), 162–167. https://doi.org/10.1016/0021-9797(69)90322-1.

(37) Rougier, V.; Cellier, J.; Duchemin, B.; Gomina, M.; Bréard, J. Influence of the Molecular Weight and Physical Properties of a Thermoplastic Polymer on Its Dynamic Wetting Behavior. *Chem. Eng. Sci.* **2023**, *269*, 118442. https://doi.org/10.1016/j.ces.2022.118442.

(38) Dee, G. T.; Sauer, B. B. The Cohesive Energy Density of Polymers and Its Relationship to Surface Tension, Bulk Thermodynamic Properties, and Chain Structure. *J. Appl. Polym. Sci.* **2017**, *134* (5). https://doi.org/10.1002/app.44431.

(39) Mahmoudi, P.; Matsen, M. W. Entropic Segregation of Short Polymers to the Surface of a Polydisperse Melt. *Eur. Phys. J. E.* **2017**, *40* (10), 85. https://doi.org/10.1140/epje/i2017-11575-7.

(40) van der Gucht, J.; Besseling, N. A. M.; Fleer, G. J. Surface Segregation in Polydisperse Polymer Melts. *Macromolecules* **2002**, *35* (17), 6732–6738. https://doi.org/10.1021/ma010964q.

(41) Gin, P.; Jiang, N.; Liang, C.; Taniguchi, T.; Akgun, B.; Satija, S. K.; Endoh, M. K.; Koga, T. Revealed Architectures of Adsorbed Polymer Chains at Solid-Polymer Melt Interfaces. *Phys. Rev. Lett.* **2012**, *109* (26), 265501. https://doi.org/10.1103/PhysRevLett.109.265501.

(42) Scheutjens, J. M. H. M.; Fleer, G. J. Statistical Theory of the Adsorption of Interacting Chain Molecules. 2. Train, Loop, and Tail Size Distribution. *J. Phys. Chem.* **1980**, *84* (2), 178–190. https://doi.org/10.1021/j100439a011.

(43) Cheng, S.; Holt, A. P.; Wang, H.; Fan, F.; Bocharova, V.; Martin, H.; Etampawala, T.; White, B. T.; Saito, T.; Kang, N.-G.; Dadmun, M. D.; Mays, J. W.; Sokolov, A. P. Unexpected Molecular Weight Effect in Polymer Nanocomposites. *Phys. Rev. Lett.* **2016**, *116* (3), 038302. https://doi.org/10.1103/PhysRevLett.116.038302.

(44) Gurney, R.; Henry, A.; Schach, R.; Lindner, A.; Creton, C. Molecular Weight Dependence of Interdiffusion and Adhesion of Polymers at Short Contact Times. *Langmuir* **2017**, *33* (7), 1670–1678. https://doi.org/10.1021/acs.langmuir.6b03972.

(45) Schach, R.; Tran, Y.; Menelle, A.; Creton, C. Role of Chain Interpenetration in the Adhesion between Immiscible Polymer Melts. *Macromolecules* **2007**, *40* (17), 6325–6332. https://doi.org/10.1021/ma0707990.

(46) Yu, J.; Cheng, B.; Ejima, H. Effect of Molecular Weight and Polymer Composition on Gallol-Functionalized Underwater Adhesive. *J. Mater. Chem. B* **2020**, *8* (31), 6798–6801. https://doi.org/10.1039/D0TB00706D.

(47) Sabzevari, S. M.; McGraw, J. D.; Wood-Adams, P. Short Chains Enhance Slip of Highly Entangled Polystyrenes during Thin Film Dewetting. *RSC Adv.* **2016**, *6* (94), 91163–91170. https://doi.org/10.1039/C6RA15606A.

(48) Hatzikiriakos, S. G. Slip Mechanisms in Complex Fluid Flows. *Soft Matter* **2015**, *11* (40), 7851–7856. https://doi.org/10.1039/C5SM01711D.

(49) Mhetar, V.; Archer, L. A. Slip in Entangled Polymer Melts. 1. General Features. *Macromolecules* **1998**, *31* (24), 8607–8616. https://doi.org/10.1021/ma980163w.

(50) Sabzevari, S. M.; McGraw, J. D.; Jacobs, K.; Wood–Adams, P. Sacrificial Mica Substrates Influence the Slip Boundary Condition of Dewetting Polymer Films. *Polymer (Guildf)* **2015**, *78*, 202–207. https://doi.org/10.1016/j.polymer.2015.08.038.

(51) Bouchaud, E.; Daoud, M. Polymer Adsorption: Concentration Effects. *J. Phys. France* **1987**, *48* (11), 1991–2000. https://doi.org/10.1051/jphys:0198700480110199100.

(52) Zhang, Z.; Peng, F.; Kornev, K. The Thickness and Structure of Dip-Coated Polymer Films in the Liquid and Solid States. *Micromachines (Basel)* **2022**, *13* (7), 982. https://doi.org/10.3390/mi13070982.

(53) Rehse, N.; Wang, C.; Hund, M.; Geoghegan, M.; Magerle, R.; Krausch, G. Stability of Thin Polymer Films on a Corrugated Substrate. *Eur. Phys. J. E* **2001**, *4* (1), 69–76. https://doi.org/10.1007/s101890170144.

(54) Wang, L.; Xu, L.; Liu, B.; Shi, T.; Jiang, S.; An, L. The Influence of Polymer Architectures on the Dewetting Behavior of Thin Polymer Films: From Linear Chains to Ring Chains. *Soft Matter* **2017**, *13* (17), 3091–3098. https://doi.org/10.1039/C7SM00379J.

(55) Chang, J.; Toga, K. B.; Paulsen, J. D.; Menon, N.; Russell, T. P. Thickness Dependence of the Young's Modulus of Polymer Thin Films. *Macromolecules* **2018**, *51* (17), 6764–6770. https://doi.org/10.1021/acs.macromol.8b00602.

(56) de Silva, J. P.; Geoghegan, M.; Higgins, A. M.; Krausch, G.; David, M.-O.; Reiter, G. Switching Layer Stability in a Polymer Bilayer by Thickness Variation. *Phys. Rev. Lett.* **2007**, *98* (26), 267802. https://doi.org/10.1103/PhysRevLett.98.267802.

(57) Yin, J.; Forrest, J. A. Film Thickness Dependent Stability and Glass Transition Temperature of Polymer Films Produced by Physical Vapor Deposition. *Phys. Rev. Lett.* **2023**, *130* (16), 168101. https://doi.org/10.1103/PhysRevLett.130.168101.

(58) Fujii, Y.; Morita, H.; Takahara, A.; Tanaka, K. Mobility Gradient of Polystyrene in Films Supported on Solid Substrates. In *Advances in Polymer Science*; Springer New York LLC, 2012; Vol. 252, pp 1–27. https://doi.org/10.1007/12_2012_175.

(59) Wang, Y.; Chan, C.-M.; Ng, K.-M.; Li, L. What Controls the Lamellar Orientation at the Surface of Polymer Films during Crystallization? *Macromolecules* **2008**, *41* (7), 2548–2553. https://doi.org/10.1021/ma7021309.

(60) Nassier, L. F.; Shinen, M. H. Study of the Optical Properties of Poly (Methyl Methacrylate) (PMMA) by Using Spin Coating Method. *Mater. Today: Proc.* **2022**, *60*, 1660–1664. https://doi.org/10.1016/j.matpr.2021.12.213.

(61) Ghasemi, B.; Ševčík, J.; Nádaždy, V.; Végsö, K.; Šiffalovič, P.; Urbánek, P.; Kuřitka, I. Thickness Dependence of Electronic Structure and Optical Properties of F8BT Thin Films. *Polymers (Basel)* **2022**, *14* (3), 641. https://doi.org/10.3390/polym14030641.

(62) Moon, C. W.; Park, J.; Park, M.; Kim, Y.; Narasimha, K.; Hyun, J. K.; Park, S.-J. Responsive Thin-Film Interference Colors from Polaronic Conjugated Block Copolymers. *ACS Appl. Mater. Interfaces* **2021**, *13* (1), 1555–1561. https://doi.org/10.1021/acsami.0c19252.

(63) Lu, X.; Clarke, M. L.; Li, D.; Wang, X.; Xue, G.; Chen, Z. A Sum Frequency Generation Vibrational Study of the Interference Effect in Poly(n -Butyl Methacrylate) Thin Films Sandwiched between Silica and Water. *J. Phys. Chem. C* **2011**, *115* (28), 13759–13767. https://doi.org/10.1021/jp202416z.

(64) Li, X.; Lu, X. Interfacial Irreversibly and Loosely Adsorbed Layers Abide by Different Evolution Dynamics. *ACS Macro Lett.* **2019**, *8* (11), 1426–1431. https://doi.org/10.1021/acsmacrolett.9b00472.

(65) Criado-Gonzalez, M.; Mijangos, C.; Hernández, R. Polyelectrolyte Multilayer Films Based on Natural Polymers: From Fundamentals to Bio-Applications. *Polymers (Basel)* **2021**, *13* (14), 2254. https://doi.org/10.3390/polym13142254.

(66) Siemann, U. Solvent Cast Technology – a Versatile Tool for Thin Film Production. In *Scattering Methods and the Properties of Polymer Materials*; Springer Berlin Heidelberg: Berlin, Heidelberg, 2005; pp 1–14. https://doi.org/10.1007/b107336.

(67) Chung, J. Y.; Chastek, T. Q.; Fasolka, M. J.; Ro, H. W.; Stafford, C. M. Quantifying Residual Stress in Nanoscale Thin Polymer Films *via* Surface Wrinkling. *ACS Nano* **2009**, *3* (4), 844–852. https://doi.org/10.1021/nn800853y.

(68) Macías-Naranjo, M.; Sánchez-Domínguez, M.; Rubio-Valle, J. F.; Rodríguez, C. A.; Martín-Alfonso, J. E.; García-López, E.; Vazquez-Lepe, E. A Study of PLA Thin Film on SS 316L Coronary Stents Using a Dip Coating Technique. *Polymers (Basel)* **2024**, *16* (2), 284. https://doi.org/10.3390/polym16020284.

(69) Butt, M. A. Thin-Film Coating Methods: A Successful Marriage of High-Quality and Cost-Effectiveness—A Brief Exploration. *Coatings* **2022**, *12* (8), 1115. https://doi.org/10.3390/coatings12081115.

(70) Park, J.; Shin, K.; Lee, C. Roll-to-Roll Coating Technology and Its Applications: A Review. *Int. J. Precis. Eng. Manuf.* **2016**, *17* (4), 537–550. https://doi.org/10.1007/s12541-016-0067-z.

(71) Aziz, F.; Ismail, A. F. Spray Coating Methods for Polymer Solar Cells Fabrication: A Review. *Mater. Sci. Semicond. Process.* **2015**, *39*, 416–425. https://doi.org/10.1016/j.mssp.2015.05.019.

(72) Reale, A.; La Notte, L.; Salamandra, L.; Polino, G.; Susanna, G.; Brown, T. M.; Brunetti, F.; Di Carlo, A. Spray Coating for Polymer Solar Cells: An Up-to-Date Overview. *Energy Technol.* **2015**, *3* (4), 385–406. https://doi.org/10.1002/ente.201402180.

(73) Yimsiri, P.; Mackley, M. R. Spin and Dip Coating of Light-Emitting Polymer Solutions: Matching Experiment with Modelling. *Chem. Eng. Sci.* **2006**, *61* (11), 3496–3505. https://doi.org/10.1016/j.ces.2005.12.018.

(74) Reiter, G.; Hamieh, M.; Damman, P.; Sclavons, S.; Gabriele, S.; Vilmin, T.; Raphaël, E. Residual Stresses in Thin Polymer Films Cause Rupture and Dominate Early Stages of Dewetting. *Nat. Mater.* **2005**, *4* (10), 754–758. https://doi.org/10.1038/nmat1484.

(75) Chen, Z.; Ward, R.; Tian, Y.; Baldelli, S.; Opdahl, A.; Shen, Y. R.; Somorjai, G. A. Detection of Hydrophobic End Groups on Polymer Surfaces by Sum-Frequency Generation Vibrational Spectroscopy. *J. Am. Chem. Soc.* **2000**, *122* (43), 10615–10620. https://doi.org/10.1021/ja000808j.

(76) Zhang, D.; Dougal, S. M.; Yeganeh, M. S. Effects of UV Irradiation and Plasma Treatment on a Polystyrene Surface Studied by IR−Visible Sum Frequency Generation Spectroscopy. *Langmuir* **2000**, *16* (10), 4528–4532. https://doi.org/10.1021/la991353i.

(77) Abe, T.; Shimada, H.; Hoshino, T.; Kawaguchi, D.; Tanaka, K. Sum Frequency Generation Imaging for Semi-Crystalline Polymers. *Polym. J.* **2022**, *54* (5), 679–685. https://doi.org/10.1038/s41428-021-00613-9.

(78) Asatekin, A.; Barr, M. C.; Baxamusa, S. H.; Lau, K. K. S.; Tenhaeff, W.; Xu, J.; Gleason, K. K. Designing Polymer Surfaces via Vapor Deposition. *Mater. Today* **2010**, *13* (5), 26–33. https://doi.org/10.1016/S1369-7021(10)70081-X.

(79) Usui, H. Preparation of Polymer Thin Films by Physical Vapor Deposition. In *Functional Polymer Films*; Wiley, 2011; pp 287–318. https://doi.org/10.1002/9783527638482.ch9.

(80) Lee, T.; Kim, J. H.; Oh, E. S.; Kim, T. Direct Tensile Testing of Free-Standing Ultrathin Polymer Films on Liquid Surface at High Temperature. *Small Methods* **2024**, 2401291. https://doi.org/10.1002/smtd.202401291.

(81) Zhang, S.; Galuska, L. A.; Gu, X. Water-assisted Mechanical Testing of Polymeric Thin-films. *J. Polym. Sci.* **2022**, *60* (7), 1108–1129. https://doi.org/10.1002/pol.20210281.

(82) Li, H.; Yan, S. Surface-Induced Polymer Crystallization and the Resultant Structures and Morphologies. *Macromolecules* **2011**, *44* (3), 417–428. https://doi.org/10.1021/ma1023457.

(83) Yuryev, Y.; Wood-Adams, P. Effect of Surface Nucleation on Isothermal Crystallization Kinetics: Theory, Simulation and Experiment. *Polymer (Guildf)* **2011**, *52* (3), 708–717. https://doi.org/10.1016/j.polymer.2010.12.043.

(84) Wu, H.-C.; Nikzad, S.; Zhu, C.; Yan, H.; Li, Y.; Niu, W.; Matthews, J. R.; Xu, J.; Matsuhisa, N.; Arunachala, P. K.; Rastak, R.; Linder, C.; Zheng, Y.-Q.; Toney, M. F.; He, M.; Bao, Z. Highly Stretchable Polymer Semiconductor Thin Films with Multi-Modal Energy Dissipation and High Relative Stretchability. *Nat. Commun.* **2023**, *14* (1), 8382. https://doi.org/10.1038/s41467-023-44099-w.

(85) Song, X.; Tao, K.; Wang, S.; Zhao, X.; Xu, J. Survey of Nanomaterials Synthesis, Fabrication, and Growth. In *21st Century Nanoscience – A Handbook*; CRC Press, 2019; pp 13-1-13–23. https://doi.org/10.1201/9780367341558-13.

(86) Fan, Z.; Men, H. Heterogeneous Nucleation and Grain Initiation on a Single Substrate. *Metals (Basel)* **2022**, *12* (9), 1454. https://doi.org/10.3390/met12091454.

(87) Bachchhav, S. D.; Roy, S.; Mukhopadhyay, M. Parametric Analysis of Homogeneous and Heterogeneous Nucleation in Subcritical CO2-Mediated Antisolvent Crystallization. *Chem. Eng. Res. Des.* **2016**, *106*, 283–297. https://doi.org/10.1016/j.cherd.2015.12.016.

(88) Meng, J.; Wang, S. Advanced Antiscaling Interfacial Materials toward Highly Efficient Heat Energy Transfer. *Adv. Funct. Mater.* **2020**, *30* (8), 1904796. https://doi.org/10.1002/adfm.201904796.

(89) Lin, C. W.; Ding, S. Y.; Hwang, Y. W. Interfacial Crystallization of Isotactic Polypropylene Molded against the Copper Surface with Various Surface Roughnesses Prepared by an Electrochemical Process. *J. Mater. Sci.* **2001**, *36* (20), 4943–4948. https://doi.org/10.1023/A:1011848623699.

(90) Cho, K.; Kim, D.; Yoon, S. Effect of Substrate Surface Energy on Transcrystalline Growth and Its Effect on Interfacial Adhesion of Semicrystalline Polymers. *Macromolecules* **2003**, *36* (20), 7652–7660. https://doi.org/10.1021/ma034597p.

(91) Chatterjee, A. M.; Price, F. P.; Newman, S. Heterogeneous Nucleation of Crystallization of High Polymers from the Melt. I. Substrate-induced Morphologies. *J. Polym. Sci. B: Polym. Phys.* **1975**, *13* (12), 2369–2383. https://doi.org/10.1002/pol.1975.180131211.

(92) Xin, R.; Zhang, J.; Sun, X.; Li, H.; Qiu, Z.; Yan, S. Epitaxial Effects on Polymer Crystallization. In *Polymer Crystallization II. Advances in Polymer Science*; Springer, 2015; pp 55–94. https://doi.org/10.1007/12_2015_329.

(93) Chan, C.-M.; Li, L. Direct Observation of the Growth of Lamellae and Spherulites by AFM. In *Advances in Polymer Science*; 2005; Vol. 188, pp 1–41. https://doi.org/10.1007/b136971.

(94) Jradi, K.; Bistac, S.; Schmitt, M.; Schmatulla, A.; Reiter, G. Enhancing Nucleation and Controlling Crystal Orientation by Rubbing/Scratching the Surface of a Thin Polymer Film. *Eur. Phys. J. E.* **2009**, *29* (4), 383–389. https://doi.org/10.1140/epje/i2009-10480-0.

(95) Lau, Y.-T. R.; Weng, L.-T.; Ng, K.-M.; Chan, C.-M. Lamellar Orientation on the Surface of a Polymer Determined by ToF-SIMS and AFM. *Appl. Surf. Sci.* **2008**, *255* (4), 1001–1005. https://doi.org/10.1016/j.apsusc.2008.05.114.

(96) Kurta, R. P.; Grodd, L.; Mikayelyan, E.; Gorobtsov, O. Y.; Zaluzhnyy, I. A.; Fratoddi, I.; Venditti, I.; Russo, M. V.; Sprung, M.; Vartanyants, I. A.; Grigorian, S. Local Structure of Semicrystalline P3HT Films Probed by Nanofocused Coherent X-Rays. *Phys. Chem. Chem. Phys.* **2015**, *17* (11), 7404–7410. https://doi.org/10.1039/C5CP00426H.

(97) Tracz, A.; Kucinska, I.; Jeszka, J. K. Unusual Crystallization of Polyethylene at Melt/Atomically Flat Interface: Lamellar Thickening Growth under Normal Pressure. *Polymer (Guildf)* **2006**, *47* (20), 7251–7258. https://doi.org/10.1016/j.polymer.2006.04.070.

(98) Stein, G. E.; Laws, T. S.; Verduzco, R. Tailoring the Attraction of Polymers toward Surfaces. *Macromolecules* **2019**, *52* (13), 4787–4802. https://doi.org/10.1021/acs.macromol.9b00492.

(99) Napolitano, S.; Cangialosi, D. Interfacial Free Volume and Vitrification: Reduction in T g in Proximity of an Adsorbing Interface Explained by the Free Volume Holes Diffusion Model . *Macromolecules* **2013**, *46* (19), 8051–8053. https://doi.org/10.1021/ma401368p.

(100) Thomas, K. R.; Chenneviere, A.; Reiter, G.; Steiner, U. Nonequilibrium Behavior of Thin Polymer Films. *Phys. Rev. E* **2011**, *83* (2), 1–8. https://doi.org/10.1103/PhysRevE.83.021804.

(101) Reiter, G.; de Gennes, P. G. Spin-Cast, Thin, Glassy Polymer Films: Highly Metastable Forms of Matter. *Eur. Phys. J. E.* **2001**, *6* (1), 25–28. https://doi.org/10.1007/s101890170024.

(102) Nguyen, H. K.; Inutsuka, M.; Kawaguchi, D.; Tanaka, K. Direct Observation of Conformational Relaxation of Polymer Chains at Surfaces. *ACS Macro Lett.* **2018**, *7* (10), 1198–1202. https://doi.org/10.1021/acsmacrolett.8b00411.

(103) Silberberg, A. Distribution of Conformations and Chain Ends near the Surface of a Melt of Linear Flexible Macromolecules. *J. Colloid Interface Sci.* **1982**, *90* (1), 86–91. https://doi.org/10.1016/0021-9797(82)90400-3.

(104) Matsen, M. W.; Mahmoudi, P. Segregation of Chain Ends to the Surface of a Polymer Melt. *Eur. Phys. J. E.* **2014**, *37* (8), 78. https://doi.org/10.1140/epje/i2014-14078-1.

(105) Li, X.; Han, X.; Wang, X.; Chen, Z.; Lu, X. Observing Different Dynamic Behaviors of Weakly and Strongly Adsorbed Polystyrene Chains at Interfaces. *Soft Matter* **2018**, *14* (15), 2762–2766. https://doi.org/10.1039/C7SM02503C.

(106) Guiselin, O. Irreversible Adsorption of a Concentrated Polymer Solution. *EPL* **1992**, *17* (3), 225–230. https://doi.org/10.1209/0295-5075/17/3/007.

(107) Sen, M.; Jiang, N.; Cheung, J.; Endoh, M. K.; Koga, T.; Kawaguchi, D.; Tanaka, K. Flattening Process of Polymer Chains Irreversibly Adsorbed on a Solid. *ACS Macro Lett.* **2016**, *5* (4), 504–508. https://doi.org/10.1021/acsmacrolett.6b00169.

(108) Barkley, D. A.; Jiang, N.; Sen, M.; Endoh, M. K.; Rudick, J. G.; Koga, T.; Zhang, Y.; Gang, O.; Yuan, G.; Satija, S. K.; Kawaguchi, D.; Tanaka, K.; Karim, A. Chain Conformation near the Buried Interface in Nanoparticle-Stabilized Polymer Thin Films. *Macromolecules* **2017**, *50* (19), 7657–7665. https://doi.org/10.1021/acs.macromol.7b01187.

(109) Evmenenko, G.; van der Boom, M. E.; Yu, C.-J.; Kmetko, J.; Dutta, P. Specular X-Ray Reflectivity Analysis of Adhesion Interface-Dependent Density Profiles in Nanometer-Scale Siloxane-Based Liquid Films. *Polymer (Guildf)* **2003**, *44* (4), 1051–1056. https://doi.org/10.1016/S0032-3861(02)00900-X.

(110) Sferrazza, M.; Jones, R. A. L.; Penfold, J.; Bucknall, D. B.; Webster, J. R. P. Neutron Reflectivity Studies of the Structure of Polymer/Polymer and Polymer/Substrate Interfaces at the Nanometer Level. *J. Mater. Chem.* **2000**, *10* (1), 127–132. https://doi.org/10.1039/a904301b.

(111) Zhang, C. Sum Frequency Generation Vibrational Spectroscopy for Characterization of Buried Polymer Interfaces. *Appl. Spectrosc.* **2017**, *71* (8), 1717–1749. https://doi.org/10.1177/0003702817708321.

(112) Lu, X.; Li, D.; Kristalyn, C. B.; Han, J.; Shephard, N.; Rhodes, S.; Xue, G.; Chen, Z. Directly Probing Molecular Ordering at the Buried Polymer/Metal Interface. *Macromolecules* **2009**, *42* (22), 9052–9057. https://doi.org/10.1021/ma901757w.

(113) Myers, J. N.; Chen, Z. Polymer Molecular Behaviors at Buried Polymer/Metal and Polymer/Polymer Interfaces and Their Relations to Adhesion in Packaging. *J. Adhes.* **2017**, *93* (13), 1081–1103. https://doi.org/10.1080/00218464.2016.1204603.

(114) Zhou, Y.; Rossi, B.; Zhou, Q.; Hihara, L.; Dhinojwala, A.; Foster, M. D. Thin Plasma-Polymerized Coatings as a Primer with Polyurethane Topcoat for Improved Corrosion Resistance. *Langmuir* **2020**, *36* (4), 837–843. https://doi.org/10.1021/acs.langmuir.9b02589.

(115) Joseph, E.; Rajput, S. S.; Patil, S.; Nisal, A. Mechanism of Adhesion of Natural Polymer Coatings to Chemically Modified Siloxane Polymer. *Langmuir* **2021**, *37* (9), 2974–2984. https://doi.org/10.1021/acs.langmuir.1c00047.

(116) Dao, T.-H.; Vu, T.-Q.-M.; Nguyen, N.-T.; Pham, T.-T.; Nguyen, T.-L.; Yusa, S.; Pham, T.-D. Adsorption Characteristics of Synthesized Polyelectrolytes onto Alumina Nanoparticles and Their Application in Antibiotic Removal. *Langmuir* **2020**, *36* (43), 13001–13011. https://doi.org/10.1021/acs.langmuir.0c02352.

(117) Tiraferri, A.; Borkovec, M. Probing Effects of Polymer Adsorption in Colloidal Particle Suspensions by Light Scattering as Relevant for the Aquatic Environment: An Overview. *Sci. Total Environ.* **2015**, *535*, 131–140. https://doi.org/10.1016/j.scitotenv.2014.11.063.

(118) Hong, Y.; Chen, W.; Fang, H.; Zuo, B.; Yuan, Y.; Zhang, L.; Wang, X. Regulation of the Interfacial Effects of Thin Polystyrene Films by Changing the Aromatic Group Structure on Substrate Surfaces. *J. Phys. Chem. C* **2019**, *123* (32), 19715–19724. https://doi.org/10.1021/acs.jpcc.9b05391.

(119) Yang, C. S.-C.; Wilson, P. T.; Richter, L. J. Structure of Polystyrene at the Interface with Various Liquids. *Macromolecules* **2004**, *37* (20), 7742–7746. https://doi.org/10.1021/ma049692s.

(120) Lin, T.; Guo, W.; Guo, R.; Chen, Z. Probing Biological Molecule Orientation and Polymer Surface Structure at the Polymer/Solution Interface In Situ. *Langmuir* **2020**, *36* (26), 7681–7690. https://doi.org/10.1021/acs.langmuir.0c01319.

(121) Delle Site, L.; Abrams, C. F.; Alavi, A.; Kremer, K. Polymers near Metal Surfaces: Selective Adsorption and Global Conformations. *Phys. Rev. Lett.* **2002**, *89* (15), 156103. https://doi.org/10.1103/PhysRevLett.89.156103.

(122) Yu, Z.; Yahsi, U.; McGervey, J. D.; Jamieson, A. M.; Simha, R. Molecular Weight-dependence of Free Volume in Polystyrene Studied by Positron Annihilation Measurements. *J. Polym. Sci. B* **1994**, *32* (16), 2637–2644. https://doi.org/10.1002/polb.1994.090321609.

(123) de Gennes, P. G.; Witten, T. A. Scaling Concepts in Polymer Physics. *Phys. Today* **1980**, *33* (6), 51–54. https://doi.org/10.1063/1.2914118.

(124) Liu, D.; Zhou, F.; Li, H.; Xin, Y.; Yi, Z. Study on the Interfacial Interactions and Adhesion Behaviors of Various Polymer-metal Interfaces in Nano Molding. *Polym. Eng. Sci.* **2021**, *61* (1), 95–106. https://doi.org/10.1002/pen.25558.

(125) Liu, D.; Zhou, F.; Zhou, H. The Polymer-Metal Interactive Behavior in Polyphenylene Sulfide/Aluminium Hetero Interface in Nano Injection Molding. *Compos. Interfaces* **2020**, *27* (3), 277–288. https://doi.org/10.1080/09276440.2019.1626138.

(126) Kleinendorst, S. M.; Fleerakkers, R.; Cattarinuzzi, E.; Vena, P.; Gastaldi, D.; van Maris, M. P. F. H. L.; Hoefnagels, J. P. M. Micron-Scale Experimental-Numerical Characterization of Metal-

Polymer Interface Delamination in Stretchable Electronics Interconnects. *Int. J. Solids Struct.* **2020**, *204–205*, 52–64. https://doi.org/10.1016/j.ijsolstr.2020.08.011.

(127) Putz, B.; Milassin, G.; Butenko, Y.; Völker, B.; Gammer, C.; Semprimoschnig, C.; Cordill, M. J. Combined TEM and XPS Studies of Metal - Polymer Interfaces for Space Applications. *Surf. Coat. Technol.* **2017**, *332*, 368–375. https://doi.org/10.1016/j.surfcoat.2017.07.079.

(128) Zhang, D. G.; Yuan, X.-C.; Teng, J. Surface Plasmon-Coupled Emission on Metallic Film Coated with Dye-Doped Polymer Nanogratings. *Appl. Phys. Lett.* **2010**, *97* (23), 231117. https://doi.org/10.1063/1.3525576.

(129) Banik, U.; Agrawal, A.; Meddeb, H.; Sergeev, O.; Reininghaus, N.; Götz-Köhler, M.; Gehrke, K.; Stührenberg, J.; Vehse, M.; Sznajder, M.; Agert, C. Efficient Thin Polymer Coating as a Selective Thermal Emitter for Passive Daytime Radiative Cooling. *ACS Appl. Mater. Interfaces* **2021**, *13* (20), 24130–24137. https://doi.org/10.1021/acsami.1c04056.

(130) Chen, D.; Zhang, Y.; Bessho, T.; Kudo, T.; Sang, J.; Hirahara, H.; Mori, K.; Kang, Z. Formation of Reflective and Conductive Silver Film on ABS Surface via Covalent Grafting and Solution Spray. *Appl. Surf. Sci.* **2015**, *349*, 503–509. https://doi.org/10.1016/j.apsusc.2015.05.039.

(131) Taguchi, A.; Kitami, T.; Yamamoto, H.; Akamaru, S.; Hara, M.; Abe, T. Surface Coating with Various Metals on Spherical Polymer Particles by Using Barrel Sputtering Technique. *J. Alloys Compd.* **2007**, *441* (1–2), 162–167. https://doi.org/10.1016/j.jallcom.2006.07.131.

(132) Zhang, S.; Tang, Y.; Vlahovic, B. A Review on Preparation and Applications of Silver-Containing Nanofibers. *Nanoscale Res. Lett.* **2016**, *11* (1), 80. https://doi.org/10.1186/s11671-016-1286-z.

(133) Tylkowski, B.; Trojanowska, A.; Nowak, M.; Marciniak, L.; Jastrzab, R. Applications of Silver Nanoparticles Stabilized and/or Immobilized by Polymer Matrixes. *Phys. Sci. Rev.* **2017**, *2* (7), 20170024. https://doi.org/10.1515/psr-2017-0024.

(134) Dallas, P.; Sharma, V. K.; Zboril, R. Silver Polymeric Nanocomposites as Advanced Antimicrobial Agents: Classification, Synthetic Paths, Applications, and Perspectives. *Adv. Colloid Interface Sci.* **2011**, *166* (1–2), 119–135. https://doi.org/10.1016/j.cis.2011.05.008.

(135) Torres, L. L.; Chauveau, M.; Hayes, P. L. Macromolecular Structure of Dodecyltrimethylammonium Chloride at the Silica/Water Interface Studied by Sum Frequency Generation Spectroscopy. *J. Phys. Chem. C* **2015**, *119* (42), 23917–23927. https://doi.org/10.1021/acs.jpcc.5b06058.

(136) Harp, G. P.; Rangwalla, H.; Li, G.; Yeganeh, M. S.; Dhinojwala, A. Coupling of Interfacial Motion at Polystyrene−Alkane Interfaces. *Macromolecules* **2006**, *39* (22), 7464–7466. https://doi.org/10.1021/ma0612226.

(137) Zhuang, X.; Miranda, P. B.; Kim, D.; Shen, Y. R. Mapping Molecular Orientation and Conformation at Interfaces by Surface Nonlinear Optics. *Phys. Rev. B* **1999**, *59* (19), 12632–12640. https://doi.org/10.1103/PhysRevB.59.12632.

(138) Fan, J.; Trenary, M. Symmetry and the Surface Infrared Selection Rule for the Determination of the Structure of Molecules on Metal Surfaces. *Langmuir* **1994**, *10* (10), 3649–3657. https://doi.org/10.1021/la00022a044.

(139) Greenler, R. G. Infrared Study of Adsorbed Molecules on Metal Surfaces by Reflection Techniques. *J. Chem. Phys.* **1966**, *44* (1), 310–315. https://doi.org/10.1063/1.1726462.

(140) Read, T.; Olkhov, R. V.; Shaw, A. M. Measurement of the Localised Plasmon Penetration Depth for Gold Nanoparticles Using a Non-Invasive Bio-Stacking Method. *Phys. Chem. Chem. Phys.* **2013**, *15* (16), 6122. https://doi.org/10.1039/c3cp50758k.

(141) Hirose, C.; Akamatsu, N.; Domen, K. Formulas for the Analysis of the Surface SFG Spectrum and Transformation Coefficients of Cartesian SFG Tensor Components. *Appl. Spectrosc.* **1992**, *46* (6), 1051–1072. https://doi.org/10.1366/0003702924124385.

(142) Horinouchi, A.; Yamada, N. L.; Tanaka, K. Aggregation States of Polystyrene at Nonsolvent Interfaces. *Langmuir* **2014**, *30* (22), 6565–6570. https://doi.org/10.1021/la500829p.

(143) Jalkanen, J.-P.; Zerbetto, F. Interaction Model for the Adsorption of Organic Molecules on the Silver Surface. *J. Phys. Chem. B* **2006**, *110* (11), 5595–5601. https://doi.org/10.1021/jp055225g.

(144) Moskovits, M.; DiLella, D. P. Surface-Enhanced Raman Spectroscopy of Benzene and Benzene- d 6 Adsorbed on Silver. *J. Chem. Phys.* **1980**, *73* (12), 6068–6075. https://doi.org/10.1063/1.440142.

(145) Teng, C.-Y.; Sheng, Y.-J.; Tsao, H.-K. Boundary-Induced Segregation in Nanoscale Thin Films of Athermal Polymer Blends. *Soft Matter* **2016**, *12* (20), 4603–4610. https://doi.org/10.1039/C6SM00559D.

(146) Cimino, R. T.; Rasmussen, C. J.; Brun, Y.; Neimark, A. V. Mechanisms of Chain Adsorption on Porous Substrates and Critical Conditions of Polymer Chromatography. *J. Colloid Interface Sci.* **2016**, *481*, 181–193. https://doi.org/10.1016/j.jcis.2016.07.019.

(147) O'Shaughnessy, B.; Vavylonis, D. Irreversibility and Polymer Adsorption. *Phys. Rev. Lett.* **2003**, *90* (5), 056103. https://doi.org/10.1103/PhysRevLett.90.056103.

(148) Welch, D.; Lettinga, M. P.; Ripoll, M.; Dogic, Z.; Vliegenthart, G. A. Trains, Tails and Loops of Partially Adsorbed Semi-Flexible Filaments. *Soft Matter* **2015**, *11* (38), 7507–7514. https://doi.org/10.1039/C5SM01457C.

(149) Tumsarp, P.; Pangpaiboon, N.; Sujaroon, K.; Deejai, S.; Treetong, A.; Sae-Ueng, U.; Sinthiptharakoon, K. Inorganic Nanoparticle-Blended Polymer Nanofilm and Its Wettability Improvement: Film Grading and Dewetting Cause Analysis. *Appl. Surf. Sci.* **2020**, *521*, 146399. https://doi.org/10.1016/j.apsusc.2020.146399.

(150) Thickett, S. C.; Neto, C.; Harris, A. T. Biomimetic Surface Coatings for Atmospheric Water Capture Prepared by Dewetting of Polymer Films. *Adv. Mater.* **2011**, *23* (32), 3718–3722. https://doi.org/10.1002/adma.201100290.

(151) Telford, A. M.; Thickett, S. C.; Neto, C. Functional Patterned Coatings by Thin Polymer Film Dewetting. *J. Colloid Interface Sci.* **2017**, *507*, 453–469. https://doi.org/10.1016/j.jcis.2017.07.004.

(152) Gentili, D.; Foschi, G.; Valle, F.; Cavallini, M.; Biscarini, F. Applications of Dewetting in Micro and Nanotechnology. *Chem. Soc. Rev.* **2012**, *41* (12), 4430. https://doi.org/10.1039/c2cs35040h.

(153) Chakrabarty, P.; Ghorai, A.; Ray, S. K.; Mukherjee, R. Polymer Thin-Film Dewetting-Mediated Growth of Wettability-Controlled Titania Nanorod Arrays for Highly Responsive, Water-Stable Self-Powered UV Photodetectors. *ACS Appl. Electron. Mater.* **2020**, *2* (9), 2895–2905. https://doi.org/10.1021/acsaelm.0c00543.

(154) Verma, A.; Sharma, A. Enhanced Self-Organized Dewetting of Ultrathin Polymer Films Under Water-Organic Solutions: Fabrication of Sub-micrometer Spherical Lens Arrays. *Adv. Mater.* **2010**, *22* (46), 5306–5309. https://doi.org/10.1002/adma.201002768.

(155) Xue, L.; Han, Y. Inhibition of Dewetting of Thin Polymer Films. *Prog. Mater. Sci.* **2012**, *57* (6), 947–979. https://doi.org/10.1016/j.pmatsci.2012.01.003.

(156) Barnes, K. A.; Karim, A.; Douglas, J. F.; Nakatani, A. I.; Gruell, H.; Amis, E. J. Suppression of Dewetting in Nanoparticle-Filled Polymer Films. *Macromolecules* **2000**, *33* (11), 4177–4185. https://doi.org/10.1021/ma990614s.

(157) Jo, K. Il; Kim, T. H.; Choi, K. I.; Lee, H.; Choi, J. H.; Bang, J.; Kim, T. H.; Yuan, G.; Satija, S. K.; Koo, J. Dewetting of Thin Polymer Films on Wrinkled Graphene Oxide Monolayers. *Langmuir* **2019**, *35* (16), 5549–5556. https://doi.org/10.1021/acs.langmuir.9b00141.

(158) Cao, P.; Bai, P.; Omrani, A. A.; Xiao, Y.; Meaker, K. L.; Tsai, H.; Yan, A.; Jung, H. S.; Khajeh, R.; Rodgers, G. F.; Kim, Y.; Aikawa, A. S.; Kolaczkowski, M. A.; Liu, Y.; Zettl, A.; Xu, K.; Crommie, M. F.; Xu, T. Preventing Thin Film Dewetting via Graphene Capping. *Adv. Mater.* **2017**, *29* (36), 1701536. https://doi.org/10.1002/adma.201701536.

(159) Singer, J. P.; Kooi, S. E.; Thomas, E. L. Focused Laser-Induced Marangoni Dewetting for Patterning Polymer Thin Films. *J. Polym. Sci. B* **2016**, *54* (2), 225–236. https://doi.org/10.1002/polb.23906.

(160) Golany, Z.; Weisbord, I.; Abo-Jabal, M.; Manor, O.; Segal-Peretz, T. Polymer Dewetting in Solvent-Non-Solvent Environment- New Insights on Dynamics and Lithography-Free Patterning. *J. Colloid Interface Sci.* **2021**, *596*, 267–277. https://doi.org/10.1016/j.jcis.2021.02.092.

(161) Verma, A.; Sekhar, S.; Sachan, P.; Reddy, P. D. S.; Sharma, A. Control of Morphologies and Length Scales in Intensified Dewetting of Electron Beam Modified Polymer Thin Films under a Liquid Solvent Mixture. *Macromolecules* **2015**, *48* (10), 3318–3326. https://doi.org/10.1021/acs.macromol.5b00029.

(162) Roy, S.; Mukherjee, R. Ordered to Isotropic Morphology Transition in Pattern-Directed Dewetting of Polymer Thin Films on Substrates with Different Feature Heights. *ACS Appl. Mater. Interfaces* **2012**, *4* (10), 5375–5385. https://doi.org/10.1021/am301311d.

(163) Chiu, M.; Wood, J. A.; Widmer-Cooper, A.; Neto, C. Aligned Droplet Patterns by Dewetting of Polymer Bilayers. *Macromolecules* **2018**, *51* (15), 5485–5493. https://doi.org/10.1021/acs.macromol.8b00620.

(164) Leng, C. Z.; Losego, M. D. Vapor Phase Infiltration (VPI) for Transforming Polymers into Organic–Inorganic Hybrid Materials: A Critical Review of Current Progress and Future Challenges. *Mater Horiz.* **2017**, *4* (5), 747–771. https://doi.org/10.1039/C7MH00196G.

(165) Peng, Q.; Tseng, Y.-C.; Darling, S. B.; Elam, J. W. A Route to Nanoscopic Materials via Sequential Infiltration Synthesis on Block Copolymer Templates. *ACS Nano* **2011**, *5* (6), 4600–4606. https://doi.org/10.1021/nn2003234.

(166) Reiter, G.; Al Akhrass, S.; Hamieh, M.; Damman, P.; Gabriele, S.; Vilmin, T.; Raphaël, E. Dewetting as an Investigative Tool for Studying Properties of Thin Polymer Films. *Eur. Phys. J.: Spec. Top.* **2009**, *166* (1), 165–172. https://doi.org/10.1140/epjst/e2009-00900-5.

(167) Wang, L. N.; Zhang, H. H.; Xu, L.; Liu, B. Y.; Shi, T. F.; Jiang, S. C.; An, L. J. Dewetting Kinetics of Thin Polymer Films with Different Architectures: Effect of Polymer Adsorption. *Chin. J. Polym.* **2018**, *36* (8), 984–990. https://doi.org/10.1007/s10118-018-2111-1.

(168) Fetzer, R.; Münch, A.; Wagner, B.; Rauscher, M.; Jacobs, K. Quantifying Hydrodynamic Slip: A Comprehensive Analysis of Dewetting Profiles. *Langmuir* **2007**, *23* (21), 10559–10566. https://doi.org/10.1021/la7010698.

(169) Brochard-Wyart, F.; de Gennes, P.-G.; Hervert, H.; Redon, C. Wetting and Slippage of Polymer Melts on Semi-Ideal Surfaces. *Langmuir* **1994**, *10* (5), 1566–1572. https://doi.org/10.1021/la00017a040.

(170) Glynos, E.; Chremos, A.; Frieberg, B.; Sakellariou, G.; Green, P. F. Wetting of Macromolecules: From Linear Chain to Soft Colloid-Like Behavior. *Macromolecules* **2014**, *47* (3), 1137–1143. https://doi.org/10.1021/ma4024119.

(171) Xu, L.; Sharma, A.; Joo, S. W. Substrate Heterogeneity Induced Instability and Slip in Polymer Thin Films: Dewetting on Silanized Surfaces with Variable Grafting Density. *Macromolecules* **2010**, *43* (18), 7759–7762. https://doi.org/10.1021/ma1010028.

(172) McClements, J.; Shaver, M. P.; Sefiane, K.; Koutsos, V. Morphology of Poly(Styrene-Co-Butadiene) Random Copolymer Thin Films and Nanostructures on a Graphite Surface. *Langmuir* **2018**, *34* (26), 7784–7796. https://doi.org/10.1021/acs.langmuir.8b01020.

(173) McClements, J.; Buffone, C.; Shaver, M. P.; Sefiane, K.; Koutsos, V. Poly(Styrene-Co-Butadiene) Random Copolymer Thin Films and Nanostructures on a Mica Surface: Morphology and Contact Angles of Nanodroplets. *Soft Matter* **2017**, *13* (36), 6152–6166. https://doi.org/10.1039/C7SM00994A.

(174) Glynos, E.; Frieberg, B.; Green, P. F. Wetting of a Multiarm Star-Shaped Molecule. *Phys. Rev. Lett.* **2011**, *107* (11), 118303. https://doi.org/10.1103/PhysRevLett.107.118303.

(175) Bäumchen, O.; Jacobs, K. Slip Effects in Polymer Thin Films. *J. Phys. Condens. Matter* **2010**, *22* (3), 033102. https://doi.org/10.1088/0953-8984/22/3/033102.

(176) Peschka, D.; Haefner, S.; Marquant, L.; Jacobs, K.; Münch, A.; Wagner, B. Signatures of Slip in Dewetting Polymer Films. *Proc. Natl. Acad. Sci. U.S.A.* **2019**, *116* (19), 9275–9284. https://doi.org/10.1073/pnas.1820487116.

(177) Petek, E. S.; Katsumata, R. Open Questions That Can Bridge Intermolecular Interactions and Macroscopic Wetting/Dewetting Behaviors of Thin Films. *Macromol. Chem. Phys.* **2023**, *224* (3), 2200375. https://doi.org/10.1002/macp.202200375.

(178) Reiter, G. Dewetting of Thin Polymer Films. *Phys. Rev. Lett.* **1992**, *68* (1), 75–78. https://doi.org/10.1103/PhysRevLett.68.75.

(179) Liu, D.; Wang, T. Instability of Hydrophobic and Viscoelastic Polymer Thin Films in Water at Room Temperature. *J. Phys. Condens. Matter* **2013**, *25* (41), 415101. https://doi.org/10.1088/0953-8984/25/41/415101.

(180) Xu, L.; Yu, X.; Shi, T.; An, L. Investigation of the Dewetting Inhibition Mechanism of Thin Polymer Films. *Soft Matter* **2009**, *5* (10), 2109. https://doi.org/10.1039/b818824f.

(181) Buckingham, A. D.; Del Bene, J. E.; McDowell, S. A. C. The Hydrogen Bond. *Chem. Phys. Lett.* **2008**, *463* (1–3), 1–10. https://doi.org/10.1016/j.cplett.2008.06.060.

(182) Tadros, T. Paints and Coatings. In *Encyclopedia of Colloid and Interface Science*; Tadros, T., Ed.; Springer Berlin Heidelberg, 2013; pp 821–868. https://doi.org/10.1007/978-3-642-20665-8_29.

(183) Kramarenko, E. Yu.; Winkler, R. G.; Khalatur, P. G.; Khokhlov, A. R.; Reineker, P. Molecular Dynamics Simulation Study of Adsorption of Polymer Chains with Variable Degree of Rigidity. I. Static Properties. *J. Chem. Phys.* **1996**, *104* (12), 4806–4813. https://doi.org/10.1063/1.471175.

(184) Wang, S.-Q. On Chain Statistics and Entanglement of Flexible Linear Polymer Melts. *Macromolecules* **2007**, *40* (24), 8684–8694. https://doi.org/10.1021/ma0712549.

(185) Smyda, M. R.; Harvey, S. C. The Entropic Cost of Polymer Confinement. *J. Phys. Chem. B* **2012**, *116* (35), 10928–10934. https://doi.org/10.1021/jp302807r.

(186) Ausserré, D. Polymer Melt Confined between Two Plates. *J. Phys. France* **1989**, *50* (19), 3021–3042. https://doi.org/10.1051/jphys:0198900500190302100.

(187) de Lima, B. M.; Hayes, P. L.; Wood-Adams, P. M. Lamellar Orientation at the Surface of Isotactic Polystyrene Thin Films Analyzed by Sum Frequency Generation Spectroscopy. *Anal Chim Acta* **2023**, *1248*, 340904. https://doi.org/10.1016/j.aca.2023.340904.

(188) de Lima, B. M.; Hayes, P. L.; Wood-Adams, P. M. Influence of Polymer Molecular Weight on Chain Conformation at the Polystyrene/Silver Interface. *Langmuir* **2021**, *37* (33), 10036–10045. https://doi.org/10.1021/acs.langmuir.1c01211.

(189) Jones, R. L.; Kumar, S. K.; Ho, D. L.; Briber, R. M.; Russell, T. P. Chain Conformation in Ultrathin Polymer Films. *Nature* **1999**, *400* (6740), 146–149. https://doi.org/10.1038/22080.

(190) Zhu, H.; Jha, K. C.; Bhatta, R. S.; Tsige, M.; Dhinojwala, A. Molecular Structure of Poly(Methyl Methacrylate) Surface. I. Combination of Interface-Sensitive Infrared-Visible Sum Frequency Generation, Molecular Dynamics Simulations, and Ab Initio Calculations. *Langmuir* **2014**, *30* (39), 11609–11618. https://doi.org/10.1021/la502333u.

(191) Franceschi, G.; Brandstetter, S.; Balajka, J.; Sokolović, I.; Pavelec, J.; Setvín, M.; Schmid, M.; Diebold, U. Interaction of Surface Cations of Cleaved Mica with Water in Vapor and Liquid Forms. *Faraday Discuss.* **2023**, *249*, 84–97. https://doi.org/10.1039/d3fd00093a.

(192) Dougherty, D. A. Cation-π Interactions in Chemistry and Biology: A New View of Benzene, Phe, Tyr, and Trp. *Science (1979)* **1996**, *271* (5246), 163–168. https://doi.org/10.1126/science.271.5246.163.

(193) Nakamura, S.; Tsuji, Y.; Yoshizawa, K. Role of Hydrogen-Bonding and OH−π Interactions in the Adhesion of Epoxy Resin on Hydrophilic Surfaces. *ACS Omega* **2020**, *5* (40), 26211–26219. https://doi.org/10.1021/acsomega.0c03798.

(194) Ma, Y.; Lu, G.; Shao, C.; Li, X. Molecular Dynamics Simulation of Hydrocarbon Molecule Adsorption on Kaolinite (0 0 1) Surface. *Fuel* **2019**, *237*, 989–1002. https://doi.org/10.1016/j.fuel.2018.10.063.

(195) Wignall, G. D.; Ballard, D. G. H.; Schelten, J. Measurements of Persistence Length and Temperature Dependence of the Radius of Gyration in Bulk Atactic Polystyrene. *Eur. Polym. J.* **1974**, *10* (9), 861–865. https://doi.org/10.1016/0014-3057(74)90142-6.

(196) Monnier, X.; Napolitano, S.; Cangialosi, D. Direct Observation of Desorption of a Melt of Long Polymer Chains. *Nat. Commun.* **2020**, *11* (1), 4354. https://doi.org/10.1038/s41467-020-18216-y.

(197) Opdahl, A.; Phillips, R. A.; Somorjai, G. A. Surface Segregation of Methyl Side Branches Monitored by Sum Frequency Generation (SFG) Vibrational Spectroscopy for a Series of Random Poly(Ethylene- Co -Propylene) Copolymers. *J Phys Chem B* **2002**, *106* (20), 5212–5220. https://doi.org/10.1021/jp013741a.

(198) Oh, S.; Cho, H.; Choi, G.; Ha, J.; Khan, Md. R. R.; Lee, H. S. Precise Control over Polymer Semiconducting Films by Tuning the Thermal Behavior of the Thin-Film State's Crystalline and Morphological Structures. *ACS Appl. Mater. Interfaces* **2019**, *11* (43), 40358–40365. https://doi.org/10.1021/acsami.9b15129.

(199) Hsu, L.-C.; Isono, T.; Lin, Y.-C.; Kobayashi, S.; Chiang, Y.-C.; Jiang, D.-H.; Hung, C.-C.; Ercan, E.; Yang, W.-C.; Hsieh, H.-C.; Tajima, K.; Satoh, T.; Chen, W.-C. Stretchable OFET Memories: Tuning the Morphology and the Charge-Trapping Ability of Conjugated Block Copolymers

through Soft Segment Branching. *ACS Appl. Mater. Interfaces* **2021**, *13* (2), 2932–2943. https://doi.org/10.1021/acsami.0c18820.

(200) Bhuvaneswari, R.; Gajendiran, J.; Karthikeyan, S.; Selvasekarapandian, S.; Gnanam, S. Synthesis of Alcotex/3-Aminopropanoic Acid Polymer Thin Film and Its Structural and Opto-Electrical Properties. *Mater. Lett.* **2021**, *282*, 128690. https://doi.org/10.1016/j.matlet.2020.128690.

(201) He, Z.; Zhang, Z.; Bi, S.; Asare-Yeboah, K.; Chen, J. Ultra-Low Misorientation Angle in Small-Molecule Semiconductor/Polyethylene Oxide Blends for Organic Thin Film Transistors. *J. Polym. Res.* **2020**, *27* (3), 75. https://doi.org/10.1007/s10965-020-02047-y.

(202) Ko, J.; Ng, C. K.; Arramel; Wee, A. T. S.; Tam, T. L. D.; Leong, W. L. Water Robustness of Organic Thin-Film Transistors Based on Pyrazino[2,3- g]Quinoxaline-Dione Conjugated Polymer. *J. Mater. Chem. C* **2020**, *8* (12), 4157–4163. https://doi.org/10.1039/D0TC00543F.

(203) Kwon, E. H.; Jang, Y. J.; Kim, G. W.; Kim, M.; Park, Y. D. Highly Crystalline and Uniform Conjugated Polymer Thin Films by a Water-Based Biphasic Dip-Coating Technique Minimizing the Use of Halogenated Solvents for Transistor Applications. *RSC Adv.* **2019**, *9* (11), 6356–6362. https://doi.org/10.1039/C8RA09231A.

(204) Heo, Y.-J.; Jeong, H.-G.; Kim, J.; Lim, B.; Kim, J.; Kim, Y.; Kang, B.; Yun, J.-M.; Cho, K.; Kim, D.-Y. Formation of Large Crystalline Domains in a Semiconducting Polymer with Semi-Fluorinated Alkyl Side Chains and Application to High-Performance Thin-Film Transistors. *ACS Appl. Mater. Interfaces* **2020**, *12* (44), 49886–49894. https://doi.org/10.1021/acsami.0c13176.

(205) Sharma, T.; Je, S.-S.; Gill, B.; Zhang, J. X. J. Patterning Piezoelectric Thin Film PVDF–TrFE Based Pressure Sensor for Catheter Application. *Sens. Actuators A Phys.* **2012**, *177*, 87–92. https://doi.org/10.1016/j.sna.2011.08.019.

(206) Sahu, P. K.; Chandra, L.; Pandey, R. K.; Mehta, N. S.; Dwivedi, R.; Mishra, V. N.; Prakash, R. Fast Development of Self-Assembled, Highly Oriented Polymer Thin Film and Observation of Dual Sensing Behavior of Thin Film Transistor for Ammonia Vapor. *Macromol. Chem. Phys.* **2019**, *220* (11), 1900010. https://doi.org/10.1002/macp.201900010.

(207) Zhang, T.; Qi, H.; Liao, Z.; Horev, Y. D.; Panes-Ruiz, L. A.; Petkov, P. St.; Zhang, Z.; Shivhare, R.; Zhang, P.; Liu, K.; Bezugly, V.; Liu, S.; Zheng, Z.; Mannsfeld, S.; Heine, T.; Cuniberti, G.; Haick, H.; Zschech, E.; Kaiser, U.; Dong, R.; Feng, X. Engineering Crystalline Quasi-Two-Dimensional Polyaniline Thin Film with Enhanced Electrical and Chemiresistive Sensing Performances. *Nat. Commun.* **2019**, *10* (1), 4225. https://doi.org/10.1038/s41467-019-11921-3.

(208) Wang, H.; Keum, J. K.; Hiltner, A.; Baer, E.; Freeman, B.; Rozanski, A.; Galeski, A. Confined Crystallization of Polyethylene Oxide in Nanolayer Assemblies. *Science (1979)* **2009**, *323* (5915), 757–760. https://doi.org/10.1126/science.1164601.

(209) Wong, K. C.; Goh, P. S.; Ismail, A. F. Enhancing Hydrogen Gas Separation Performance of Thin Film Composite Membrane through Facilely Blended Polyvinyl Alcohol and PEBAX. *Int. J. Hydrog. Energy* **2021**, *46* (37), 19737–19748. https://doi.org/10.1016/j.ijhydene.2020.09.079.

(210) Yu, C.; Xie, Q.; Bao, Y.; Shan, G.; Pan, P. Crystalline and Spherulitic Morphology of Polymers Crystallized in Confined Systems. *Crystals (Basel)* **2017**, *7* (5), 147. https://doi.org/10.3390/cryst7050147.

(211) Michell, R. M.; Blaszczyk-Lezak, I.; Mijangos, C.; Müller, A. J. Confinement Effects on Polymer Crystallization: From Droplets to Alumina Nanopores. *Polymer (Guildf)* **2013**, *54* (16), 4059–4077. https://doi.org/10.1016/j.polymer.2013.05.029.

(212) Carr, J. M.; Langhe, D. S.; Ponting, M. T.; Hiltner, A.; Baer, E. Confined Crystallization in Polymer Nanolayered Films: A Review. *J. Mater. Res.* **2012**, *27* (10), 1326–1350. https://doi.org/10.1557/jmr.2012.17.

(213) Wang, W.-C.; Chen, S.-Y.; Yang, Y.-W.; Hsu, C.-S.; Tajima, K. Face-on Reorientation of π-Conjugated Polymers in Thin Films by Surface-Segregated Monolayers. *J. Mater. Chem. A* **2020**, *8* (13), 6268–6275. https://doi.org/10.1039/D0TA00030B.

(214) Sirringhaus, H.; Brown, P. J.; Friend, R. H.; Nielsen, M. M.; Bechgaard, K.; Langeveld-Voss, B. M. W.; Spiering, A. J. H.; Janssen, R. A. J.; Meijer, E. W.; Herwig, P.; de Leeuw, D. M. Two-Dimensional Charge Transport in Self-Organized, High-Mobility Conjugated Polymers. *Nature* **1999**, *401* (6754), 685–688. https://doi.org/10.1038/44359.

(215) Biniek, L.; Leclerc, N.; Heiser, T.; Bechara, R.; Brinkmann, M. Large Scale Alignment and Charge Transport Anisotropy of PBTTT Films Oriented by High Temperature Rubbing. *Macromolecules* **2013**, *46* (10), 4014–4023. https://doi.org/10.1021/ma400516d.

(216) Honda, K.; Morita, M.; Otsuka, H.; Takahara, A. Molecular Aggregation Structure and Surface Properties of Poly(Fluoroalkyl Acrylate) Thin Films. *Macromolecules* **2005**, *38* (13), 5699–5705. https://doi.org/10.1021/ma050394k.

(217) Eriksson, M.; Notley, S. M.; Wågberg, L. Cellulose Thin Films: Degree of Cellulose Ordering and Its Influence on Adhesion. *Biomacromolecules* **2007**, *8* (3), 912–919. https://doi.org/10.1021/bm061164w.

(218) Gossart, A.; Gand, A.; Ollivier, V.; Boissière, M.; Santerre, J. P.; Letourneur, D.; Pauthe, E. Coating of Cobalt Chrome Substrates with Thin Films of Polar/Hydrophobic/Ionic Polyurethanes: Characterization and Interaction with Human Immunoglobulin G and Fibronectin. *Colloids Surf. B* **2019**, *179*, 114–120. https://doi.org/10.1016/j.colsurfb.2019.03.040.

(219) Taguchi, K.; Miyaji, H.; Izumi, K.; Hoshino, A.; Miyamoto, Y.; Kokawa, R. Growth Shape of Isotactic Polystyrene Crystals in Thin Films. *Polymer (Guildf)* **2001**, *42* (17), 7443–7447. https://doi.org/10.1016/S0032-3861(01)00215-4.

(220) Sawamura, S.; Miyaji, H.; Izumi, K.; J. Sutton, S.; Miyamoto, Y. Growth Rate of Isotactic Polystyrene Crystals in Thin Films. *J. Phys. Soc. Japan* **1998**, *67* (10), 3338–3341. https://doi.org/10.1143/JPSJ.67.3338.

(221) Wang, Y.; Ge, S.; Rafailovich, M.; Sokolov, J.; Zou, Y.; Ade, H.; Lüning, J.; Lustiger, A.; Maron, G. Crystallization in the Thin and Ultrathin Films of Poly(Ethylene−vinyl Acetate) and Linear Low-

Density Polyethylene. *Macromolecules* **2004**, *37* (9), 3319–3327. https://doi.org/10.1021/ma030456b.

(222) Sutton, S. J.; Izumi, K.; Miyaji, H.; Miyamoto, Y.; Miyashita, S. The Morphology of Isotactic Polystyrene Crystals Grown in Thin Films: The Effect of Substrate Material. *J. Mater. Sci.* **1997**, *32* (21), 5621–5627. https://doi.org/10.1023/A:1018688827486.

(223) Schönherr, H.; Frank, C. W. Ultrathin Films of Poly(Ethylene Oxides) on Oxidized Silicon. 1. Spectroscopic Characterization of Film Structure and Crystallization Kinetics. *Macromolecules* **2003**, *36* (4), 1188–1198. https://doi.org/10.1021/ma020685i.

(224) Liu, Y.-X.; Chen, E.-Q. Polymer Crystallization of Ultrathin Films on Solid Substrates. *Coord. Chem. Rev.* **2010**, *254* (9–10), 1011–1037. https://doi.org/10.1016/j.ccr.2010.02.017.

(225) Sun, X.; Chen, Z.; Wang, F.; Yan, S.; Takahashi, I. Influence of Poly(Vinylphenol) Sublayer on the Crystallization Behavior of Poly(3-Hydroxybutyrate) Thin Films. *Macromolecules* **2013**, *46* (4), 1573–1581. https://doi.org/10.1021/ma302349a.

(226) Mareau, V. H.; Prud'homme, R. E. Crystallization of Ultrathin Poly(ε-Caprolactone) Films in the Presence of Residual Solvent, an in Situ Atomic Force Microscopy Study. *Polymer (Guildf)* **2005**, *46* (18), 7255–7265. https://doi.org/10.1016/j.polymer.2005.06.036.

(227) Zhang, D.; Shen, Y. R.; Somorjai, G. A. Studies of Surface Structures and Compositions of Polyethylene and Polypropylene by IR+visible Sum Frequency Vibrational Spectroscopy. *Chem. Phys. Lett.* **1997**, *281* (4–6), 394–400. https://doi.org/10.1016/S0009-2614(97)01311-0.

(228) Johnson, C. M.; Sugiharto, A. B.; Roke, S. Surface and Bulk Structure of Poly-(Lactic Acid) Films Studied by Vibrational Sum Frequency Generation Spectroscopy. *Chem. Phys. Lett.* **2007**, *449* (1–3), 191–195. https://doi.org/10.1016/j.cplett.2007.10.061.

(229) Kawaguchi, D.; Yamamoto, K.; Abe, T.; Jiang, N.; Koga, T.; Yamamoto, S.; Tanaka, K. Local Orientation of Chains at Crystal/Amorphous Interfaces Buried in Isotactic Polypropylene Thin Films. *Phys. Chem. Chem. Phys.* **2021**, *23* (41), 23466–23472. https://doi.org/10.1039/D1CP03959H.

(230) Duan, Y.; Zhang, J.; Shen, D.; Yan, S. In Situ FTIR Studies on the Cold-Crystallization Process and Multiple Melting Behavior of Isotactic Polystyrene. *Macromolecules* **2003**, *36* (13), 4874–4879. https://doi.org/10.1021/ma034008f.

(231) Zhang, H.; Yu, M.; Zhang, B.; Reiter, R.; Vielhauer, M.; Mülhaupt, R.; Xu, J.; Reiter, G. Correlating Polymer Crystals via Self-Induced Nucleation. *Phys. Rev. Lett.* **2014**, *112* (23), 237801. https://doi.org/10.1103/PhysRevLett.112.237801.

(232) Taguchi, K.; Miyaji, H.; Izumi, K.; Hoshino, A.; Miyamoto, Y.; Kokawa, R. Crystal Growth of Isotactic Polystyrene in Ultrathin Films: Film Thickness Dependence. *J. Macromol. Sci. B* **2002**, *41* (4–6), 1033–1042. https://doi.org/10.1081/MB-120013081.

(233) Chen, X.; Lee, C. M.; Wang, H.-F.; Jensen, L.; Kim, S. H. Experimental and Theoretical Study of Azimuth Angle and Polarization Dependences of Sum-Frequency-Generation Vibrational

Spectral Features of Uniaxially Aligned Cellulose Crystals. *J. Phys. Chem. C* **2017**, *121* (34), 18876–18886. https://doi.org/10.1021/acs.jpcc.7b03037.

(234) Xue, G.; Wang, Y.; Liu, S.; Liao, Y.-T. FT-IR Study of Concentration Dependence for Crystallization of Isotactic Polystyrene Arising from Freeze-Drying Dilute Solutions. *Macromolecules* **1995**, *28* (12), 4344–4346. https://doi.org/10.1021/ma00116a043.

(235) Matsuba, G.; Kaji, K.; Nishida, K.; Kanaya, T.; Imai, M. Conformational Change and Orientation Fluctuations of Isotactic Polystyrene Prior to Crystallization. *Polym. J.* **1999**, *31* (9), 722–727. https://doi.org/10.1295/polymj.31.722.

(236) Kobayashi, M.; Nakaoki, T.; Ishihara, N. Molecular Conformation in Glasses and Gels of Syndiotactic and Isotactic Polystyrenes. *Macromolecules* **1990**, *23* (1), 78–83. https://doi.org/10.1021/ma00203a015.

(237) Šašić, S.; Zhang, J.; Ozaki, Y. Detailed Interpretation of the Results of Two-Dimensional Correlation Analysis of Infrared Spectra Obtained during Isothermal Crystallization of Isotactic Polystyrene and Poly(3-Hydroxybutyrate). *Vib. Spectrosc.* **2007**, *44* (1), 50–55. https://doi.org/10.1016/j.vibspec.2006.07.016.

(238) Zhang, J.; Duan, Y.; Shen, D.; Yan, S.; Noda, I.; Ozaki, Y. Structure Changes during the Induction Period of Cold Crystallization of Isotactic Polystyrene Investigated by Infrared and Two-Dimensional Infrared Correlation Spectroscopy. *Macromolecules* **2004**, *37* (9), 3292–3298. https://doi.org/10.1021/ma049910h.

(239) Zhang, J.; Duan, Y.; Sato, H.; Shen, D.; Yan, S.; Noda, I.; Ozaki, Y. Initial Crystallization Mechanism of Isotactic Polystyrene from Different States. *J. Phys. Chem. B* **2005**, *109* (12), 5586–5591. https://doi.org/10.1021/jp0449004.

(240) Xu, H.; Ince, B. S.; Cebe, P. Development of the Crystallinity and Rigid Amorphous Fraction in Cold-Crystallized Isotactic Polystyrene. *J. Polym. Sci. B* **2003**, *41* (23), 3026–3036. https://doi.org/10.1002/polb.10625.

(241) Oh-e, M.; Hong, S.-C.; Shen, Y. R. Orientations of Phenyl Sidegroups and Liquid Crystal Molecules on a Rubbed Polystyrene Surface. *Appl. Phys. Lett.* **2002**, *80* (5), 784–786. https://doi.org/10.1063/1.1435069.

(242) Zhang, Y.; Anim-Danso, E.; Bekele, S.; Dhinojwala, A. Effect of Surface Energy on Freezing Temperature of Water. *ACS Appl. Mater. Interfaces* **2016**, *8* (27), 17583–17590. https://doi.org/10.1021/acsami.6b02094.

(243) Painter, P. C.; Koenig, J. L. A Normal Vibrational Analysis of Isotactic Polystyrene. *J. Polym. Sci. B* **1977**, *15* (11), 1885–1903. https://doi.org/10.1002/pol.1977.180151102.

(244) Natta, G.; Corradini, P.; Bassi, I. W. Crystal Structure of Isotactic Polystyrene. *Nuovo Cimento* **1960**, *15*, 68–82.

(245) Kett, P.; Casford, M.; Davies, P. Effect of Multiple Group Orientations on Sum Frequency Generation Spectra. *Mol. Phys.* **2013**, *111* (2), 175–187. https://doi.org/10.1080/00268976.2012.711492.

(246) Kett, P. J. N.; Casford, M. T. L.; Davies, P. B. Sum Frequency Generation Spectrum of a Self-Assembled Monolayer Containing Two Different Methyl Group Orientations. *J. Phys. Chem. Lett.* **2012**, *3* (22), 3276–3280. https://doi.org/10.1021/jz301363k.

(247) Xiao, M.; Mohler, C.; Tucker, C.; Walther, B.; Lu, X.; Chen, Z. Structures and Adhesion Properties at Polyethylene/Silica and Polyethylene/Nylon Interfaces. *Langmuir* **2018**, *34* (21), 6194–6204. https://doi.org/10.1021/acs.langmuir.8b00930.

(248) Chuang, W.-T.; Hong, P.-D.; Chuah, H. H. Effects of Crystallization Behavior on Morphological Change in Poly(Trimethylene Terephthalate) Spherulites. *Polymer (Guildf)* **2004**, *45* (7), 2413–2425. https://doi.org/10.1016/j.polymer.2004.01.048.

(249) Sutton, S. J.; Izumi, K.; Miyaji, H.; Fukao, K.; Miyamoto, Y. The Lamellar Thickness of Melt Crystallized Isotactic Polystyrene as Determined by Atomic Force Microscopy. *Polymer (Guildf)* **1996**, *37* (24), 5529–5532. https://doi.org/10.1016/S0032-3861(96)00435-1.

(250) Taguchi, K.; Miyamoto, Y.; Toda, A. Molecular Weight Dependence of Crystal Growth in Isotactic Polystyrene Ultrathin Films. *ACS Macro Lett.* **2019**, *8* (10), 1227–1232. https://doi.org/10.1021/acsmacrolett.9b00516.

(251) Ku, H. H. Notes on the Use of Propagation of Error Formulas. *Journal of Research of the National Bureau of Standards, Section C: Engineering and Instrumentation* **1966**, *70C* (4), 263. https://doi.org/10.6028/jres.070C.025.

(252) de Bruijn, H. E.; Kooyman, R. P. H.; Greve, J. Determination of Dielectric Permittivity and Thickness of a Metal Layer from a Surface Plasmon Resonance Experiment. *Appl. Opt.* **1990**, *29* (13), 1974. https://doi.org/10.1364/AO.29.001974.

(253) Chulhai, D. V.; Hu, Z.; Moore, J. E.; Chen, X.; Jensen, L. Theory of Linear and Nonlinear Surface-Enhanced Vibrational Spectroscopies. *Annu. Rev. Phys. Chem.* **2016**, *67* (1), 541–564. https://doi.org/10.1146/annurev-physchem-040215-112347.

(254) Baldelli, S.; Markovic, N.; Ross, P.; Shen, Y.-R.; Somorjai, G. Sum Frequency Generation of CO on (111) and Polycrystalline Platinum Electrode Surfaces: Evidence for SFG Invisible Surface CO. *J. Phys. Chem. B* **1999**, *103* (42), 8920–8925. https://doi.org/10.1021/jp991649x.